INFORMATION EXTRACTION FROM POLARIMETRIC SAR IMAGES

Rajib Kumar Panigrahi

INFORMATION EXTRACTION FROM POLARIMETRIC SAR IMAGES

A

Thesis submitted

for the award of the degree of

DOCTOR OF PHILOSOPHY

By

Rajib Kumar Panigrahi

DEPARTMENT OF ELECTRONICS AND ELECTRICAL ENGINEERING
INDIAN INSTITUTE OF TECHNOLOGY GUWAHATI
GUWAHATI - 781039, INDIA
MAY 2011

Certificate

This is to certify that the thesis entitled "**INFORMATION EXTRACTION FROM POLARIMETRIC SAR IMAGES**", submitted by **Rajib Kumar Panigrahi** (08610201), a research scholar in the *Department of Electronics and Electrical Engineering, Indian Institute of Technology Guwahati*, for the award of the degree of **Doctor of Philosophy**, is a research work carried out by him under our supervision. The thesis has fulfilled all requirements as per the regulations of the institute and in our opinion has reached the standard needed for submission. The results embodied in this thesis have not been submitted to any other University or Institute for the award of any degree or diploma.

Dated:
Guwahati.

Dr. A. K. Mishra
Assistant Professor
Dept. of Electronics and Electrical Engg.
Indian Institute of Technology Guwahati
Guwahati - 781039, Assam, India.

Dr. S. Dandapat
Professor
Dept. of Electronics and Electrical Engg.
Indian Institute of Technology Guwahati
Guwahati - 781039, Assam, India.

This work is dedicated

to

My elder brother

Shri Pradeep Kumar Panigrahi

and

My Parents

Smt. Sabita Panigrahi

&

Shri Chiranjiba Panigrahi

Acknowledgements

First, I would like to express my deep and sincere gratitude to my supervisor Prof. Amit Kumar Mishra for his decisive guidance, kindness, and constant encouragement throughout this PhD study and research. His enthusiasm, friendly accessibility and never-say-give-up attitude has been a constant source of inspiration for me to put up my best in research. Under his guidance, I not only learnt how to do research but also learnt some approaches of life. I thank him for patiently correcting my thesis.

I would like to thank Prof. Samarendra Dandapat for taking the role of my supervisor at the end phase of my research and for the support during this period. I would like to acknowledge my deepest respect and gratitude to him for his advices and encouragement that kept me stay focussed at the crucial end phase of the thesis. His invaluable suggestions have helped the thesis to have a better structure.

I acknowledge my deepest gratitude to all the members of my doctoral committee for their valuable comments on my thesis work. I sincerely thank Prof. S. R. M. Prasanna, the chairman of my doctoral committee for his kindness and invaluable suggestions.

I am grateful to Prof. P. K. Bora, Prof. S. R. M. Prasanna and Prof. Amit K. Mishra, from whose classes I was benefitted enormously. I would like to thank all faculties and staff in our department for their help and support.

The thesis work has been funded partly by the Indian Space Research Organization (ISRO), India, via sanction number ISRO/RES/4/561/08-09 for which I humbly acknowledge my gratefulness to ISRO Respond program.

My stay at IIT guwahati for last 3 years would not have been memorable if I were not associated with Omprakash (an ideal friend), Sanjoy (cool guy), Jana (cricket mania), Sayantan (moving encyclopedia), Samar (the computer wizard), Himanshuji (Matlab and latex expert), R. C. Mishra sir, Dolgobinda sir, Nagesh, Ashish, Kuntal, Pati sir, Mukesh sir, Utkalji, Shyam sir, Bhabesh sir, Senthil sir, Kartikeyan sir, Govind, Haris, Panda bhai, and Sarada bhai. I also would like to thank some of my close friends: Devender, Bhanu, Prem, Durga, Saroj, Hari, Mitra, Satya, Hadu, Biswa, and Tapan.

I wish to thank my family for their love and support during my PhD. I would like to extend my special thanks my wife Sukesini, who has been with me in the whole journey. The acknowledgement would be half-complete, if i do not render my thanks and gratitude to my grandparents, my sisters Queen and Rina nani and brother-in-law Biswanath bhai. I wish to express my deepest gratitude to my parents for their love throughout my life and the sacrifices they have made for me. This thesis is written in the memory of my elder brother, who is always a source of inspiration for me. I dedicated this thesis to my parents and elder brother.

Finally, I would like to express my deepest and most sincere thanks to all who contributed in my thesis work.

I praise lord Jagannath for all the blessings I received from him.

R. K. Panigrahi

Abstract

This thesis deals with extraction of information from polarimetric (Pol) synthetic aperture Radar (SAR) images. The complete thesis work can be presented under three major areas. The first major area of work comprises of information extraction from polarimetric SAR (PolSAR) images. In this, we propose and develop three new unsupervised algorithms for landcover mapping and crop classification using PolSAR images. The second major area of work deals with extraction of information from the images of the recently introduced hybrid-PolSAR architecture. At first, to realize the potential of this new polarimetric configuration, a comparison of hybrid-Pol configuration with the full polarimetric SAR configuration based on the information content is carried out. Secondly, we propose three new approaches for the analysis of the hybrid-Pol data to extract information from its images. The third major area of work deals with PolSAR image enhancement techniques. More precisely, this deals with sidelobe noise suppression in PolSAR images using non linear apodization techniques. We also validate that better information can be extracted from the PolSAR images, if sidelobe noise is removed from its images.

Contents

List of Figures

List of Tables

List of Algorithms

List of Acronyms

2-D	Two Dimensional
ASR	Adaptive Sidelobe Reduction
BSA	Backscatter Alignment
CDA	Complex Dual Apodization
DCP	Dual Circular Pol
DoP	Degree of Polarization
DFT	Discrete Fourier Transform
DA	Dual Apodization
EM	Expectation Maximization
E2CDA	Extended 2-Dimensional CDA
FSA	Forward Scattering Alignment
FT	Fourier Transform
GTRI	Georgia Technology Research Institute
GMM	Gaussian Mixture Models
ISRO	Indian Space Research Organisation
IPR	Impulse Response
LHCP	Left-Hand Circular Polarization
LGNLA	Local Gradient Based NLA
MSTAR	Moving and Stationary Target Acquisition and Recognition
ML	Maximum Likelihood
MLE	Maximum Likelihood Estimation
NLA	Non Linear Apodization

Pol	Polarimetric
PolSAR	Polarimetric SAR
PCA	Principle Component Analysis
PRF	Pulse Repetition Frequency
RP	Relative Phase
RISAT	Radar Imaging Satellite
RHCP	Right-Hand Circular Polarization
SAR	Synthetic Aperture Radar
SLAR	Side Looking Airborne Radar
SNR	Signal to Noise Ratio
SVA	Spatially Variant Apodization

1

Introduction

Contents

The thesis is concerned with extraction of information from polarimetric (Pol) synthetic aperture Radar (SAR) images. The thrust of current research and development in radar community is in applying the polarimetric concept to radar remote sensing. The polarimetric radar field started a new era with the acquisition of polarimetry data from the airborne SAR flown by the jet propulsion laboratory in the spring of 1985. Presently, the polarimetric radar field has reached its golden period of time. Keeping the progress in vigil, a concurrent topic in radar polarimetry is chosen as thesis work. This topic is about developing polarimetric tools and techniques to extract information from polarimetric SAR (PolSAR) images. The basic objective of this thesis is to find issues in this topic and address them.

This chapter presents a comprehensive overview of the basic principles of radar polarimetry and its application in remote sensing. The rest of the chapter is organized as follows. In the next section, an introduction to microwave remote sensing and its usefulness over optical remote sensing is presented. Evolution of different polarimetric SAR configurations from optical radar through real aperture radar followed by synthetic aperture radar is presented. Also usage of polarimetric radar in remote sensing applications is summarized. In Section 1.2, basics of polarimetric radar scattering from pure point targets and distributed targets is presented. In Section 1.3, the objective of the thesis is presented. Section 1.4 presents the details of the thesis organization.

1.1 Polarimetric SAR remote sensing

1.1.1 Remote sensing

Remote sensing is the science of acquiring information about the earth's surface remotely. This is achieved by sensing and recording reflected or emitted energy and processing, analyzing, and interpreting that information [1].

Remote sensing can be broadly classified into two, viz. optical and microwave remote sensing. In optical remote sensing, sensor detects solar radiations in the visible spectrum that scattered from the earth surface and forms images that looks alike photographs taken by a camera located high up in space. Microwave remote sensing data is quite different from optical remote sensing data. It provides many unique features that not found in their counterpart. A detailed study of microwave remote sensing and its advantages over optical remote sensing is provided here in next.

1.1.2 Microwave remote sensing

Microwaves are part of radio spectrum in the frequency range of 3-30 GHz. At frequencies above about 20 GHz, microwave signals passing through the earth's atmosphere are highly attenuated due to absorption by water and oxygen molecules. Thus the frequency range of 3-20 GHz has been used primarily for passive and active remote sensing of the earth's land and ocean surface, as attenuation of the atmosphere is low for this band [2].

Microwave remote sensors are of two types.

- **Active sensors**, e.g. imaging radars and non-imaging radars: scatterometers, and altimeters.
- **Passive sensors**, e.g. radiometers.

Imaging radars: Imaging radars observe the earth surface from outer space using satellites (spaceborne) or from the air using aircrafts (airborne). A radar image is a 2-D array of pixels formed by columns and rows, where a pixel is associated with a small area of earth's surface. The size of the area depends on the radar system characteristics. Each pixel provides a complex number associated to the reflectivity of all scatterers contained in the radar resolution cell. The different types of imaging radars along with their functionalities will be discussed in Section 1.1.3.

Scatterometer: A scatterometer measures the scattering properties of targets. A scatterometer usually measures the range (distance R) to the scattering target in order to calculate the backscattering coefficient from the received power.

Altimeter: An altimeter is a nadir-looking short-pulse radars used to measure the height of the radar's platform above the ground surface. An altimeter is similar to a scatterometer except that its primary function is to measure the height.

Radiometer: All objects, not at absolute zero temperature, radiate weak electromagnetic energy as a result of thermally induced random motions of electrons and protons. A microwave radiometer consists of an antenna, a very sensitive receiver, and a recorder. It is used to measure the thermal noise waves emitted from the earth's surface or atmosphere [2].

1.1.2.1 Unique features of microwave remote sensing

Microwave remote sensing data is quite different from optical and thermal remote sensing data. It provides many unique features that are not found in their optical or thermal counterparts. Some of these unique features are recapitulated here.

- **Geologic mapping application:** The advantage with radar sensor is that the angle of illumination can be changed. This is not possible with optical sensors where the geometry is completely fixed by the position of the Sun and the time of data acquisition [3]. Optical sensors also require fixed Sun angle for providing constant illumination. Since imaging radars are active device, they do not depend upon the Sun angle [2].

- **All day-all weather capability:** Microwave sensors can be used for remote sensing of earth surface during any time of the day as it does not require the presence of Sun to map earth surface. They also have the all weather capability as microwave can penetrate through clouds. Hence, the dynamic changes on earth surface, where repetitive observation with short time interval is required, can be studied using microwave sensors only. Some such usages are summarized below.
    - The continuously cloud covered surface of Venus was first seen with microwave sensors.
    - Mapping of perennially cloud-covered regions such as the Brazilian jungle can be done using radar.

  - Microwave radar data has also been important for studying volcanoes that are either cloud covered or obscured by volcanic ash during an eruption [4].
  - Microwave radar can take flood images during the immediate post-flood period when the area is still cloud covered from continuing storms [4].
  - Microwave sensor with its ability to collect ice sheet data through cloud and throughout the extended polar night has been an indispensable tool for the glaciologist. Several studies have demonstrated the capabilities of microwave sensors for monitoring ice sheet motion, ice topography, glacial surges, and flow dynamics of the Greenland ice sheet [4].

- **Microwave can penetrate Soil and Ice:** One of the unique features of microwave radar is that microwave signal can penetrate through soil, canopy and ice to a certain extent. L band radar waves can penetrate as much as 2 meter of very dry sand to image subsurface features. Drainage networks below the Sahara Desert, millions of year old, were first mapped through the use of the radars [5]. Low microwave frequencies can penetrate forest canopy and so one can get information about the object under forest, like whether the forest is flooded or not [5]. Microwave sensors are also capable of penetrating through the dry snow and hence can detect buried objects under snow.

- **Sensitivity to moisture and salinity:** The presence of moisture influences effective skin depth (penetration into soil). As the moisture content of surface soil increases, the transmitted wave tends to scatter from the surface. As moisture content decreases, skin depth increases and the signal may be scattered from a greater thickness of soil [5]. Therefore the soil moisture can be determined using microwave sensors which is an important parameter for hydrologists. The dielectric constant of ice is highly sensitive to the degree of salinity. Hence microwave radars can be used for distinguishing first-year ice from multi-year ice in polar regions as they do not have the same degree of salinity [2].

- **Oceanographic applications:** Microwave sensors can accurately measure the magnitude and direction of oceanic winds. The ability to routinely measure oceanic winds at global scales is crucially important to climatological studies as well as for the timely prediction of ocean storms and to other problems faced by oceanographer [3]. Microwave sensors could measure sea-surface salinity in very fine gradation of 500 parts per million [2]. Microwave sensors can also measure the velocity of ships. Detection of natural and man made slicks on the sea is crucial to the protection of the environment and the enforcement of regulations. Radar images are useful for detecting and measuring the extent of oil seepage on the ocean surface [4].

- **Atmosphere:** The microwave sensors can measure the backscatter from rain, clouds, and atmospheric water for meteorological studies and weather prediction. Using low frequency radars, it is possible to measure atmospheric winds and detect clear-air turbulence for improved weather prediction and aircraft routing [2].

1.1.3 Evolution of SAR

The first imaging radar is known as side looking airborne radar (SLAR). It is called so, as in this type of radar systems, an antenna is fixed below the aircraft which looks at a side. In the beginning, the SLAR systems were primarily developed for identification of military targets. Later it was evolved into a tool for remote sensing of the earth surface. The SLAR systems produce stripmap images by periodically transmitting a pulse and receiving the generated echo. The SLAR systems ensure that the echoes from the current pulse are received before the next pulse is transmitted. A geometry of SLAR system is shown in Figure 1.1. The resolution of such systems depend on two parameter: pulse length (τ) and antenna beamwidth (β). The pulse length τ defines the spatial resolution in the range direction (X_r). The width of the antenna beam β defines the spatial resolution in the azimuth direction (X_a).

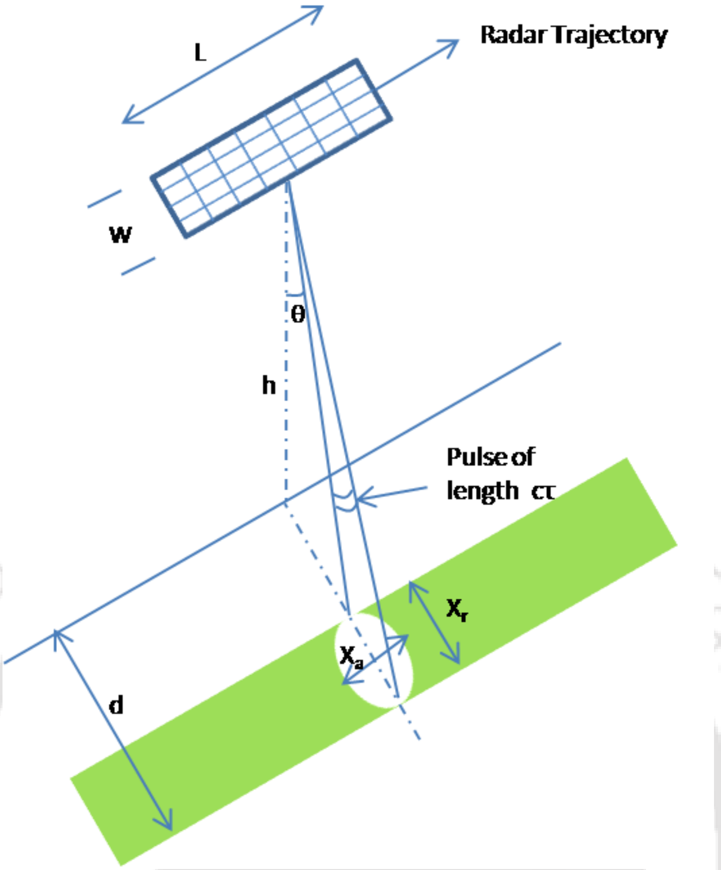

Figure 1.1: Geometry of a side looking aperture radar.

Range resolution: The range resolution is given by

$$X_r = \frac{c\tau}{2 \times \sin\theta}, \tag{1.1}$$

where c is the velocity of light and θ is the radar look angle. From the above relation, it is clear that range resolution is directly proportional to pulse length τ. Therefore, in order to achieve a finer range resolution, the pulse length should be as short as possible. However utilizing a pulse of short duration reduces the average transmitted power, which in turn reduces the received signal to noise ratio (SNR). The short pulse also enhances the operating bandwidth. However, It is often desirable that a pulsed radar system has both; fine range resolution and adequate average power transmission. This can be made possible by using pulse compression techniques. Pulse compression allows a pulsed radar system to achieve the average transmitted power of a long pulse, while obtaining the range resolution of a short pulse, simultaneously. Pulse compression is achieved by phase or frequency modulating the long pulse to be transmitted. The modulation process enhances the transmitted signal bandwidth. The received signal is processed through a matched filter that compresses the long pulse to achieve a fine range resolution corresponding to a short pulse.

Azimuthal resolution: The azimuthal resolution is given by

$$X_a = d\beta, \text{ where } \beta = \frac{\lambda}{L}, \tag{1.2}$$

where d is the swath width, λ is the wavelength of the transmitted pulse and L is the physical length of the antenna. For a given wavelength and swath width, the azimuthal resolution X_a depends on the length of the antenna. To have a fine azimuthal resolution, the length of the antenna should be long. Even if it is not impossible, it is difficult and impractical to construct and deploy such huge antennas.

1.1.3.1 Synthetic aperture radar

The poor azimuthal resolution of SLAR system can be overcome by using synthetic aperture radar (SAR). It is called as synthetic aperture radar as in this system a small-aperture antenna is used to synthesize the effect of a large aperture antenna through modified data recording and signal processing techniques. There are several different ways to explain the operation of a synthetic aperture radar. Here we have conceptualize the operation of a SAR system based on the doppler frequency shift of the echo.

The root of SAR concepts rooted in Carl A. Wiley work, where he observed that the resolution of a SLAR can be improved by utilizing the information contained in the Doppler frequency shift of the echo [6]. Using this observation, it is possible that the targets lying in the azimuth direction can be differentiated as different targets introduce different frequency shift. Even though they are illuminated by the same pulse, the angle of illumination is different for different targets in the azimuth direction. Therefore the relative velocity of each target with respect to aircraft moving at a constant speed is different. Hence different targets, in azimuth direction, illuminated by the same pulse introduce different frequency shifts. The targets to which the aircraft is approaching has a positive doppler frequency shift, whereas if the aircraft is receding it has negative doppler frequency shift. By processing the return echoes according to their Doppler frequency shifts, a fine azimuthal resolution can be obtained.

1.1.4 Polarimetric SAR

Conventional SARs which transmit and receive single polarization, results in scalar characterization of the backscattered wave which is a vector field. Therefore, any additional information about the scattering process contained in the polarization properties of the scattered signal is lost. Polarization information contained in the waves backscattered from a scattering media is influenced by the scatterer's geometrical structure, orientation and its geophysical properties such as humidity, roughness and conductivity. To retain this polarization information, the backscattered field must be measured by a vector measurement process. This requires that the radar be capable of decomposing the received wave into two orthogonally polarized components, which independently feed two identical and coherent reception channels. The polarization and the amplitude of the backscattered wave depends not only on target characteristics, but also on the polarization of the transmitted wave. To acquire complete polarimetric information of the target, reception polarization-diversity must be accompanied by transmission polarization-diversity [7,8]. Polarimetric radar which alternately transmits two orthogonal polarized waves, and receives the resulting backscatter simultaneously using two orthogonally polarized antennas, is capable of capturing all the polarization information in the backscattered wave.

There has been a growing interest in radar polarimetry due to the high quality data produced by various airborne missions (NASA/AIRSAR, DLR/ESAR, DLR/EMISAR, ONERA/RAMSES, CCRS/CONVAIR), and spaceborne missions (NASA/SIR−C, CSA/RADARSAT−2, DLR/TERRASAR−X, JAXA/ALOS−PALSAR).

1.1.5 Hybrid polarimetric SAR

Complete polarimetric information helps in better target decomposition and hence better scene or target classification. Despite of these advantages, fully polarimetric radar system (quad-Pol) suffers from an increase in the pulse repetition frequency (PRF) by a factor of two and increase in the data rate by a factor of four in comparison to conventional single polarization radars (single-Pol) [9].

As the PRF is increased by a factor of two, the swath coverage is halved to maintain the performance with respect to range ambiguities and average transmitted power is doubled. The reduced swatch coverage of the fully polarimetric radar system has an adverse impact on revisit time, which is always a important factor for the Earth-observing community.

A tradeoff between these two systems is dual-polarimetric (dual-Pol) systems that transmits a single polarization wave and coherently receives two orthogonal polarized waves. Dual-Pol offers more target information than a single-Pol system, and simultaneously overcomes some of the drawbacks of quad-Pol system. In comparison to quad-Pol system, dual-Pol systems have the advantage of halved average transmitted power and doubled swath coverage. Because of these benefits, there has been growing interest in dual-Pol systems now a days. Therefore, it is necessary to understand the amount of information content of these dual-Pol systems in comparison with quad-Pol systems. There are different dual-Pol systems based on the different transmitted polarization and coherent dual linear receive polarization.

- Dual linear Pol: single (H) linear transmit, dual (H and V) linear receive.
- $\Pi/4$ Pol: Slant (45^o) linear transmit, dual linear receive.
- Hybrid-Pol: Circular transmit (R or L), dual linear receive.
- Dual circular Pol (DCP): Circular transmit, dual (R and L) circular receive.

Different dual-Pol systems collect different aspects of polarimetric information. The last three configurations are collectively known as “compact polarimetry” or “partial polarimetry". Any linearly polarized transmit system such as dual linear Pol and Π/4 mode will not be able to excite a target response as with linear structures that are oriented orthogonal to the incident electric field. For this reason, the use of circularly polarized transmit systems are preferred for a generic Radar system.

Circular polarization waves are the least effected from ionospheric distortion as compared to any other polarization. Therefore, a circular polarization on-transmit guarantees that the scattering target will always be illuminated by wave of a constant polarization [10]. Moreover, the ratio of desired signal to rain clutter can be improved as circular polarization is insensitive to spherical target [11]. Among the circular transmit, hybrid-Pol is preferred than DCP. Because, in case of DCP, its performance is limited by the weaker cross polarized links,which is effected by additive noise and by crosstalk from the stronger "like polarized" signal [12]. Therefore, hybrid-Pol mode happens to be objectively superior than other dual-Pol alternatives.

In comparison to other dual-Pol SAR modes, the hybrid-Pol architecture can lead to a system with less RF hardware, less mass, and fewer losses, all of which are essential for applications such as lunar or planetary exploration [12]. The Mini-SAR on Chandraayan-1 is the first practical radar that is based on this hybrid-Pol architecture. Also, the radar imaging satellite (RISAT), the first SAR satellite from Indian Space Research Organisation (ISRO), currently under development, supports this hybrid-Pol configuration [13]. Hence, it can be stated that India is one of the pioneering nations in implementing this type of radar systems.

1.1.6 Use of polarimetric radar for remote sensing applications

The areas of application of polarimetric SAR remote sensing are outlined below.

- Agricultural
- Landuse and landcover
- Soil Moisture

- Forestry
- Oceanographic
- Radar Geology
- Snow and Ice and Glacier
- Wetlands

These are the broad areas in which polarimetric SAR remote sensing finds its applications. For example, the various applications in agriculture are crop-type identification, crop condition monitoring and yield estimation, soil conservation farming and rangelands monitoring. This thesis is concerned with the use of polarimetric data in two remote sensing applications, viz. landcover mapping and crop type identification. Researches in the use of polarimetric radar for these two applications are closely related. Phase preservation in polarimetric radar increases the information content that gives polarimetry an edge over conventional radar system. For example, the phase information along with polarization magnitude can be used for characterization of scattering from the crop and landcover [4, 14].

1.2 A Mathematical background for polarimetric radar

1.2.1 Polarization descriptors

The polarization of a monochromatic electromagnetic plane wave describes the shape and locus of the electric vector end point in a plane orthogonal to the direction of wave propagation. The instantaneous field of a plane wave, traveling in the Z direction, can be written as

$$\underline{E} = \underline{u}_x |E_x| \cos(\omega t - kz + \phi_x) + \underline{u}_y |E_y| \cos(\omega t - kz + \phi_y). \tag{1.3}$$

Let $\phi = \phi_x - \phi_y$ is the time phase difference between the two components x and y. The different possible polarizations are

- **Linear**: For the wave to have linear polarization, ϕ must be equal to multiples of π.

- **Circular**: Circular polarization can be achieved only when the magnitudes of the two components are the same and ϕ is odd multiple of $\pi/2$.
- **Elliptical**: Elliptical polarization can be attained only when ϕ is odd multiple of $\pi/2$ and their amplitudes are not equal or ϕ is not equal to multiple of $\pi/2$.

There are different representation of wave polarization for monochromatic waves which are given below [15].

- Polarization ellipse
- Jones vector
- Polarization ratio
- Stokes parameter
- Poincare sphere

The monochromatic waves are fully polarized waves. In remote sensing applications, generally we encountered with partially polarized waves. Partially polarized waves arise when a completely polarized wave is scattered by a random or distributed target. A distributed target may be taken as a collection of separated non-stationary sub-scatterers. A distributed target is said to depolarize the incident wave, which is completely polarized, to a partially polarized wave. Therefore sometimes, the distributed targets are called as depolarizing target. The parameters that characterize a partially polarized wave must be time averaged and are meaningful only under wide sense stationarity and ergodicity. A partially polarized wave may be characterized by the following descriptors.

1.2.1.1 Jones coherency matrix

The 2×2 complex Hermitian positive semi-definite Jones coherence matrix $\mathbf{J}$ is defined as [15]

$$\mathbf{J} = \begin{bmatrix} \langle E_x(t)E_x^*(t)\rangle & \langle E_x(t)E_y^*(t)\rangle \\ \langle E_y(t)E_X^*(t)\rangle & \langle E_y(t)E_y^*(t)\rangle \end{bmatrix} = \begin{bmatrix} J_{xx} & J_{xy} \\ J_{xy}^* & J_{yy} \end{bmatrix} \tag{1.4}$$

J is a 2×2 complex Hermitian positive semidefinite matrix. The determinant of **J** may be written as

$$\|\mathbf{J}\| = J_{xx}J_{yy} - |J_{xy}|^2 \tag{1.5}$$

By Schwartz inequality, it can be shown that $\|\mathbf{J}\| \geq 0$, for partially polarized wave; $\|\mathbf{J}\| = 0$, for complete polarized wave; and for unpolarized wave, $J_{xy} = 0$ and $J_{xx} = J_{yy}$.

1.2.1.2 Stokes vector

The Jones matrix elements can be obtained through the use of a coherent radar systems that can measure the amplitude and phase of an incoming wave. However in the past, coherent radar systems were not available. Only systems those are able to measure the observable power terms of an incoming wave were available. Hence, it was quite necessary at that time to characterize the polarization of a wave only by power measurements terms which are real quantities [16]. The characterization of partially polarized wave in terms of real quantities is done by Stokes vector $\underline{G}$.

$$\underline{G} = \begin{bmatrix} G_0 \\ G_1 \\ G_2 \\ G_3 \end{bmatrix} = \begin{bmatrix} \langle |E_x|^2 + |E_y|^2 \rangle \\ \langle |E_x|^2 - |E_y|^2 \rangle \\ 2\mathrm{Re}\langle E_x^* E_y)\rangle \\ 2\mathrm{Im}\langle E_x^* E_y)\rangle \end{bmatrix} \tag{1.6}$$

For completely polarized case, $G_0^2 = G_1^2 + G_2^2 + G_3^2$. The coherency matrix elements in terms of the stokes parameters are given by

$$\begin{aligned} J_{xx} &= \tfrac{1}{2}\left(G_0 + G_1\right) \\ J_{yy} &= \tfrac{1}{2}\left(G_0 - G_1\right) \\ J_{xy} &= \tfrac{1}{2}\left(G_2 - jG_3\right) \\ J_{yx} &= \tfrac{1}{2}\left(G_2 + jG_3\right) \end{aligned} \tag{1.7}$$

Now the determinant of **J** ($\|\mathbf{J}\|$) in terms of Stokes parameter can be obtained as

$$\|\mathbf{J}\| = \frac{1}{4}(G_0^2 - G_1^2 - G_2^2 - G_3^2). \tag{1.8}$$

As for partially polarized wave $\|\mathbf{J}\| \geq 0$, it follows that $G_0^2 \geq G_1^2 + G_2^2 + G_3^2$. For unpolarized wave as $J_{xy} = 0$ and $J_{xx} = J_{yy}$, it follows that $G_1 = G_2 = G_3 = 0$.

The ratio of the power densities of the polarized part and the total wave is called the degree of polarization (DoP) of the wave. The DoP of the wave is an important parameter which can be used for target scattering characterization [17]. The stokes vector of any wave may be split into Stokes vector of an unpolarized wave and Stokes vector of a completely polarized wave in an unique way as follows.

$$\underline{G} = \begin{bmatrix} G_0 \\ G_1 \\ G_2 \\ G_3 \end{bmatrix} = \begin{bmatrix} \sqrt{G_1^2 + G_2^2 + G_3^2} \\ G_1 \\ G_2 \\ G_3 \end{bmatrix} + \begin{bmatrix} G_0 - \sqrt{G_1^2 + G_2^2 + G_3^2} \\ 0 \\ 0 \\ 0 \end{bmatrix} \tag{1.9}$$

1.2.2 Mathematical characterization of target scattering

Generally, the wave scattered from the target has different properties from the incident one. The changes are due to the electromagnetic interaction between the target and the incident wave. In radar polarimetry, we are concerned with the change in wave polarization. The change in polarization can be attributed to the characteristics of the target scattering. In the following, we present different mathematical ways by which the target scattering can be studied.

1.2.2.1 Scattering matrix

The electric fields $\underline{E}^s$ and $\underline{E}^i$ of the scattered wave and the incident waves are related by 2×2 complex scattering matrix $\mathbf{S}$ defined as [15]:

$$\underline{E}^s = \mathbf{S}\underline{E}^i. \tag{1.10}$$

The $\mathbf{S}$ matrix, which is expressed in the backscatter alignment (BSA) coordinates, is referred to as the Sinclair matrix and is given in the horizontal-vertical polarization basis

(H, V) as

$$\mathbf{S} = \begin{bmatrix} S_{HH} & S_{HV} \\ S_{VH} & S_{VV} \end{bmatrix}, \tag{1.11}$$

where the first and second subscript denotes the received and transmitted polarization, respectively. In general, the elements of the scattering matrix are complex and uncorrelated with each other. The scattering matrix can be parameterized as follows.

$$\mathbf{S} = \begin{bmatrix} |S_{HH}|e^{j\phi_{HH}} & |S_{HV}|e^{j\phi_{HV}} \\ |S_{VH}|e^{j\phi_{VH}} & |S_{VV}|e^{j\phi_{VV}} \end{bmatrix} = e^{j\phi_{HH}} \cdot \begin{bmatrix} |S_{HH}| & |S_{HV}|e^{j(\phi_{HV}-\phi_{HH})} \\ |S_{VH}|e^{j(\phi_{VH}-\phi_{HH})} & |S_{VV}|e^{j(\phi_{VV}-\phi_{HH})} \end{bmatrix} \tag{1.12}$$

The matrix in the right-hand side of the equation is called as relative scattering matrix $\mathbf{S}_R$ which is parameterized by seven parameters; four amplitude and the three relative phase.

In monostatic backscattering case, the reciprocity-principle constrains the Sinclair scattering matrix to be symmetrical, that is, $S_{HV} = S_{VH}$. Then the relative scattering matrix can be written as follows.

$$\mathbf{S}_R = \begin{bmatrix} |S_{HH}|e^{j\phi_{HH}} & |S_{HV}|e^{j\phi_{HV}} \\ |S_{HV}|e^{j\phi_{HV}} & |S_{VV}|e^{j\phi_{VV}} \end{bmatrix} = \begin{bmatrix} |S_{HH}| & |S_{HV}|e^{j(\phi_{HV}-\phi_{HH})} \\ |S_{HV}|e^{j(\phi_{HV}-\phi_{HH})} & |S_{VV}|e^{j(\phi_{VV}-\phi_{HH})} \end{bmatrix} \tag{1.13}$$

Here the relative scattering matrix is parameterized by five parameters; the three amplitudes and the two relative phases. Therefore for monostatic case, a given target can be characterized by five parameters.

1.2.2.2 Scattering target vector

The 2 × 2 target scattering matrix **S** can be represented by a target vector as follows [16].

$$\mathbf{S} = \begin{bmatrix} S_{xx} & S_{xy} \\ S_{yx} & S_{yy} \end{bmatrix} \Rightarrow \underline{k} = \frac{1}{2}Tr(\mathbf{S}\Psi) \tag{1.14}$$

where ψ is a complete set of 2 × 2 complex basis matrices which are constructed as an orthogonal set under the Hermitian inner product.

There exist in literature different basis sets. However two special sets that have been used in the polarimetric radar literature are the Pauli and the Lexicographic basis sets. The Pauli spin matrix basis set Ψ_P for bistatic scattering is defined as

$$\{\Psi_P\} = \left\{ \sqrt{2}\begin{bmatrix} 1 & 0 \\ 0 & 1 \end{bmatrix} \quad \sqrt{2}\begin{bmatrix} 1 & 0 \\ 0 & -1 \end{bmatrix} \quad \sqrt{2}\begin{bmatrix} 0 & 1 \\ 1 & 0 \end{bmatrix} \quad \sqrt{2}\begin{bmatrix} 0 & -j \\ j & 0 \end{bmatrix} \right\}. \tag{1.15}$$

The corresponding target vector $\underline{k}$ becomes

$$\underline{k} = \frac{1}{\sqrt{2}} \begin{bmatrix} S_{xx} + S_{yy} & S_{xx} - S_{yy} & S_{xy} + S_{yx} & j\left(S_{xy} - S_{yx}\right) \end{bmatrix}^T. \tag{1.16}$$

The second Lexicographic matrix basis set Ψ_P for bistatic scattering is defined as

$$\{\Psi_L\} = \left\{ 2\begin{bmatrix} 1 & 0 \\ 0 & 0 \end{bmatrix} \quad 2\begin{bmatrix} 0 & 1 \\ 0 & 0 \end{bmatrix} \quad 2\begin{bmatrix} 0 & 0 \\ 1 & 0 \end{bmatrix} \quad 2\begin{bmatrix} 0 & 0 \\ 0 & 1 \end{bmatrix} \right\}. \tag{1.17}$$

The corresponding target vector $\underline{\Omega}$ becomes

$$\underline{\Omega} = \begin{bmatrix} S_{xx} & S_{xy} & S_{yx} & S_{yy} \end{bmatrix}^T. \tag{1.18}$$

For monostatic backscattering case, the target vectors are given by

$$\underline{k} = \frac{1}{\sqrt{2}} \begin{bmatrix} S_{xx} + S_{yy} & S_{xx} - S_{yy} & 2S_{xy} \end{bmatrix}^T, \quad \underline{\Omega} = \begin{bmatrix} S_{xx} & S_{xy} & \sqrt{2}S_{yx} \end{bmatrix}^T. \tag{1.19}$$

1.2.2.3 Kennaugh and Mueller matrices

Using the BSA convention, Stokes vector of the backscattered wave is related to the incident-wave Stokes vector through Kennaugh matrix, **K** [18].

$$\underline{G}^s = \mathbf{K}\underline{G}^i \tag{1.20}$$

The 4 × 4 Kennaugh matrix is defined as

$$\mathbf{K} = \mathbf{A}^*(\mathbf{S} \otimes \mathbf{S}^*)\mathbf{A}^{-1} \tag{1.21}$$

where ⊗ corresponds to the Kronecker product and the matrix **A** is given by

$$\mathbf{A} = \begin{bmatrix} 1 & 0 & 0 & 1 \\ 1 & 0 & 0 & -1 \\ 0 & 1 & 1 & 0 \\ 0 & j & -j & 0 \end{bmatrix}. \tag{1.22}$$

For forward scattering alignment (FSA) case, this matrix is known as Mueller matrix **M**. **M** and **K** are related by

$$\mathbf{M} = diag \begin{bmatrix} 1 & 1 & 1 & -1 \end{bmatrix} [\mathbf{K}]. \tag{1.23}$$

Pure or deterministic targets can be described by using either the scattering matrix **S** or the Mueller/Kennaugh matrix. For such targets there exists a one to one correspondence between the scattering matrix and the Mueller/Kennaugh matrix and the two descriptions are equivalent. For backscattering case, there are five independent parameters in the relative scattering matrix. Therefore only five real elements will completely characterize **M** or **K**. It then follows that the nine elements of Mueller/Kennaugh matrix are not independent. There must be four equations relating the Mueller/Kennaugh matrix elements to each other.

However, distributed targets can not be described by a single scattering matrix. A distributed target re-radiates a partially polarized waves. Since Stokes vector exists for a partially polarized waves, it follows that the distributed target can be described by Mueller/Kennaugh matrix. Sixteen real elements are needed to fully characterize the system in the general case, and nine elements are needed under the reciprocity assumption.

1.2.2.4 Target covariance and coherency matrices

Similar to **M** and **K**, two other matrices named target covariance matrix and target coherence matrix can be used for the characterization of distributed targets [19]. Distributed targets can be described by the second order moments of the fluctuations which are captured in the forms of polarimetric coherency or covariance matrices. The polarimetric Pauli coherency **T** matrix and the Lexicographic covariance **C** matrix are generated from the ensemble averaging of the outer product of the corresponding target vector with its conjugate transpose as

$$\mathbf{T} = \left\langle \underline{k} \cdot \underline{k}^{*\mathrm{T}} \right\rangle, \mathbf{C} = \left\langle \underline{\Omega} \cdot \underline{\Omega}^{*\mathrm{T}} \right\rangle, \tag{1.24}$$

where $\langle . \rangle$ indicates spatial ensemble averaging.

The expressions for the backscattering coherency matrix for a pure target is given by [16]

$$\mathbf{T} = \begin{bmatrix} 2A_0 & C - jD & H + jG \\ C + jD & B_0 + B & E + jF \\ H - jG & E - jF & B_0 - B \end{bmatrix}, \tag{1.25}$$

where all the nine parameters are called "Huynen parameters" and each of them contains real physical target information [16,20]. Analogous to Mueller matrix, for pure target case, only five real elements should completely characterize the backscattering coherency matrix **T**. It then follows that the nine Huynen parameters are related to each other by four equations that are called the "monostatic target structure equations" [16]. The monostatic target structure equations can be derived by noting that for rank 1 matrix, all its principal minors are zero. As the coherency matrix in such a case is a rank 1 Hermitian matrix, its nine principal minors are set to zero. From these nine equation, four equations are derived and presented below.

$$\begin{aligned} 2A_0(B_0 + B) &= C^2 + D^2 \\ 2A_0(B_0 - B) &= G^2 + H^2 \\ 2A_0 E &= CH - DG \\ 2A_0 F &= CG + DH \end{aligned} \tag{1.26}$$

If these four monostatic target structure equations are satisfied, then the measured coherency matrix has a single corresponding scattering matrix.

1.3 Objective of the thesis

The objective of this thesis are three folds. These are as follows.

- To develop new approaches and algorithms to extract information from PolSAR images. The thesis deals with two major applications of remote sensing, viz. landcover mapping and crop classification. The main focus is on developing new algorithms that can correctly discriminate different land features using PolSAR images.
- To realize the potential of recently introduced hybrid-Pol data in comparison to the full polarimetric SAR data. Secondly, to analyze the hybrid-Pol data to extract information from its images.
- To develop polarimetric SAR image enhancement techniques based on sidelobe noise suppression, and to extract information from the PolSAR images after removal of sidelobe noise.

1.4 Thesis organization

A schematic of the thesis organization is shown in Figure 1.2. The complete thesis work can be presented under three major areas as shown in this figure.

The rest of the thesis is organized as follows:

Chapter 2 presents a review of information extraction techniques from PolSAR images, quantitative techniques for the analysis of hybrid-Pol data and noise suppression algorithms developed for PolSAR images.

In Chapter 3, a thorough investigation of Wishart-entropy/alpha method is carried out and its limitations are specified. We propose three different unsupervised landcover classification algorithms. We also show that these proposed techniques outperform the classic Wishart-entropy/alpha technique.

In Chapter 4, a comparison of hybrid-Pol system with quad-Pol system is carried out to realize the potential of hybrid-Pol system. Along with this, three new approaches for the

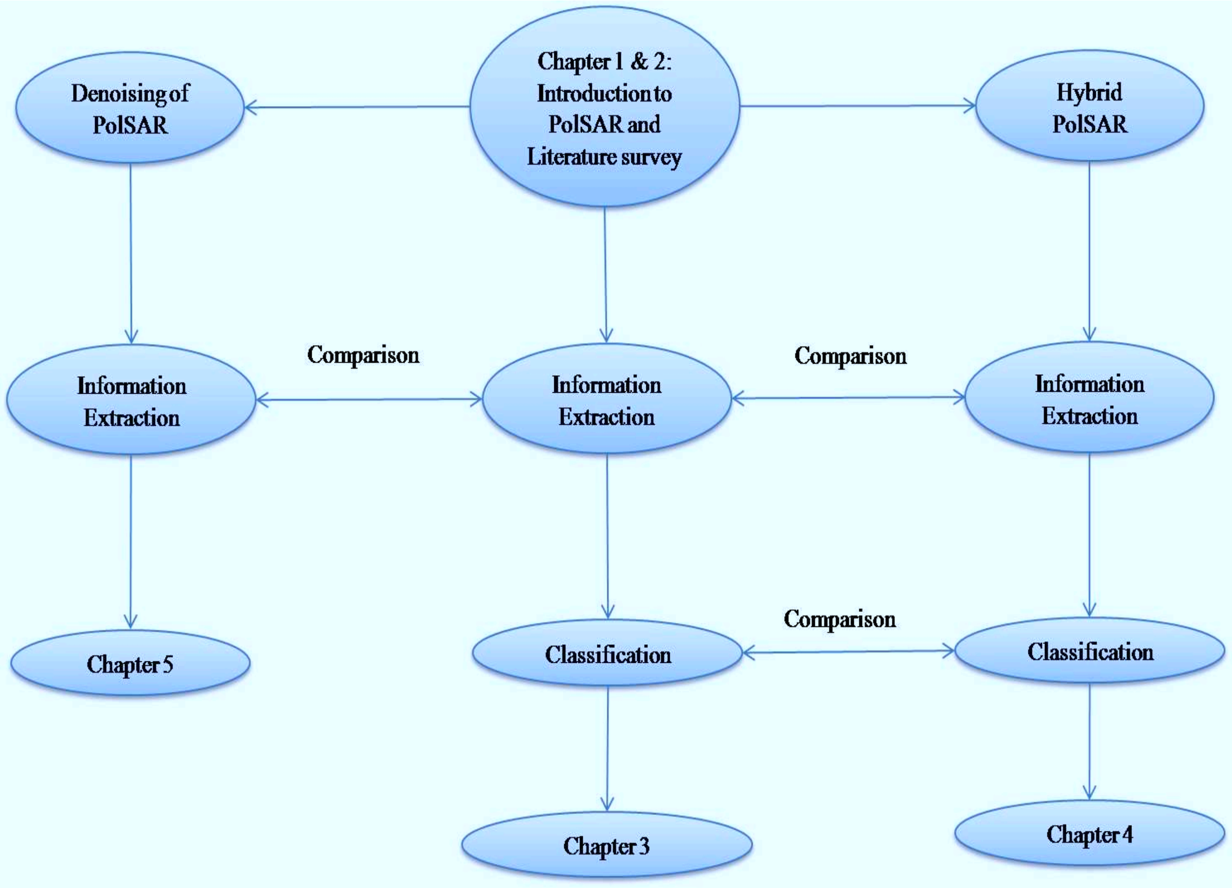

Figure 1.2: A schematic of the thesis organization.

analysis of hybrid-Pol system are proposed.

Chapter 5 deals with PolSAR image enhancement using non linear apodization (NLA) techniques. In this chapter, we propose a new NLA algorithm for PolSAR image enhancement. We also develop a 2-D version of CDA algorithm which can be used for PolSAR image enhancement. Information extraction from PolSAR images, before and after implementation of image enhancement techniques, are considered.

2

Information Extraction from Polarimetric SAR Images: A Review

Contents

This chapter provides a review of existing approaches pertinent to the thesis. The objective of this thesis are three folds as detailed in Section 1.3. The main motive of the thesis is to extract information from polarimetric SAR (PolSAR) images. Therefore, at first, we will review various information extraction techniques developed for PolSAR images. Several parameters are obtained from these techniques, which help in interpretation and classification of PolSAR images. There are many supervised and unsupervised approaches which have been developed for classification of landcover types. However, the thesis is concerned with unsupervised landcover classification techniques based on physics of scattering mechanisms. A thorough review of such techniques is provided in this chapter. The second objective of the thesis is to exploit the potential of recently proposed hybrid-Pol system. There are quite a few reports published in the open literature on hybrid-Pol architecture. Those will be reviewed here. Thirdly, the thesis deals with PolSAR image enhancement techniques based on sidelobe noise suppression. Therefore, a comprehensive study of different sidelobe suppression techniques will also be done in this chapter.

The rest of the chapter is organized as follows. In the next section, we will give a review of various information extraction techniques which have been applied to PolSAR images. In Section 2.2, a review of landcover classification techniques is provided. Section 2.3 reviews the techniques developed for analysis of the hybrid-Pol data. Section 2.4 presents a review of radar image enhancement through different sidelobe noise suppression techniques. In Section 2.5, the scope of this thesis is discussed.

2.1 Information extraction through target decomposition techniques

A fully polarimetric radar system, which alternately transmits two orthogonal polarized waves and measures the scattered wave by dual coherent orthogonal polarized channels, contains all the information about the scattering process in the backscattered wave [1] [7,8]. Information from the PolSAR images can be extracted by either using scattered wave

---

[1] *All information* in this context means all information that can be captured using the given bandwidth.

parameters [17, 21] or receive wave parameters [22], or target decomposition techniques. Here, only algorithms based on decomposition techniques will be reviewed.

Data measured by a polarimetric radar system is usually represented in the form of either scattering matrix, Mueller matrix or covariance matrix. These matrices contain all the information about the scattering properties of the target at each sample point. Physical information from these matrices can be extracted by using a set of algorithms known as target decomposition algorithms [19]. The objective of target decomposition theory is to express the scattering matrix, Mueller matrix or covariance matrix as the sum of independent components, such that a physical scattering mechanism can be associated to each of the components.

2.1.1 Phenomenological Huynen decomposition

The first target decomposition technique was developed by Chandrasekhar [23], in his work on light scattering by small anisotropic particles. Chandrasekhar decomposed the phase matrix into the sum of three independent components, where the first and second yield an physical interpretation. Huynen, in his Ph.D. dissertation [20], introduced a target decomposition theorem, in which he decomposed an average Mueller matrix $\mathbf{M}$ into the sum of a Mueller matrix that corresponds to a pure target $\mathbf{M}_0$, and a 'residue target' or 'N-target' which represents noise $\mathbf{M}_N$.

$$\langle \mathbf{M} \rangle = \mathbf{M}_0 + \langle \mathbf{M}_N \rangle. \tag{2.1}$$

$\mathbf{M}_0$ has an equivalent single scattering matrix that can be characterized by five independent parameters. As nine parameters are required to fully characterize the average Mueller matrix $\mathbf{M}$, it follows that the residual N-target contains the four remaining degree of freedom. Both the targets are independent of each other. The N-target is chosen such that it represents non-symmetric target parameters. This decomposition was not made arbitrarily, but follows from the fact that N-target is roll invariant. The Huynen decomposition can equally be applied on target coherency matrix [19]:

$$\langle \mathbf{T} \rangle = \mathbf{T}_0 + \langle \mathbf{T}_N \rangle. \tag{2.2}$$

Unlike Chandrasekhars decomposition, however, Huynen decomposition is not unique [16, 24]. There can be another two principal Huynen type decompositions [25]. Mathematically, the roll-invariance property of the N-target $\mathbf{T}_N$ can be expressed as

$$\mathbf{T}_N(\theta) = \mathbf{U}_B(\theta)\mathbf{T}_N\mathbf{U}_B(\theta)^{-1}, \tag{2.3}$$

where change of base matrix $\mathbf{U}_B$ is given by

$$\mathbf{U}_B(\theta) = \begin{bmatrix} 1 & 0 & 0 \\ 0 & \cos 2\theta & \sin 2\theta \\ 0 & -\sin 2\theta & \cos 2\theta \end{bmatrix}. \tag{2.4}$$

The invariance under rotation requires that the null space of the N-target remains unchanged under the transformation of Equation (2.3) [19]. Any arbitrary vector $\underline{q}$ belongs to the null space of N-target, if

$$\mathbf{T}_N(\theta)\underline{q} = 0. \tag{2.5}$$

Since the vector space generated by $\mathbf{T}_N$ is orthogonal to the vector space generated by the pure target $\mathbf{T}_0$, mathematically, it can be stipulated that $\mathbf{T}_0$ contains all the vectors that lie in the null space of N-target.

By substituting Equation (2.3) into Equation (2.5), it can be shown that the vector $\underline{q}$ is an eigenvector of the matrix $\mathbf{U}_B$.

$$\begin{aligned} &\mathbf{U}_B(\theta)\mathbf{T}_N\mathbf{U}_B(\theta)^{-1}\underline{q} = 0 \\ &\Rightarrow \mathbf{U}_B(\theta)^{-1}\underline{q} = \lambda\underline{q} \end{aligned} \tag{2.6}$$

The matrix $\mathbf{U}_B$ has three eigenvectors as given below,

$$\underline{q}_1 = \begin{bmatrix} 1 \\ 0 \\ 0 \end{bmatrix}, \ \underline{q}_2 = \begin{bmatrix} 0 \\ 1 \\ j \end{bmatrix}, \ \underline{q}_3 = \begin{bmatrix} 0 \\ j \\ 1 \end{bmatrix}. \tag{2.7}$$

It then follows that there can be three Huynen type decompositions corresponding to three eigenvectors of the rotation matrix $\mathbf{U}_B$. Choosing the eigenvector $\underline{q}_1$ corresponds to the original decomposition proposed by Huynen. However, by choosing one of the other eigenvectors, a different $\mathbf{T}_0$ matrix is generated. That results in a different factorizations of the coherence matrix $\mathbf{T}$, known as Barnes and Holm decomposition [16, 25].

2.1.2 Eigenvector-based decompositions

A second class of target decomposition theorems are those based on eigenvector analysis of the coherency matrix [19, 26]. This decomposition technique is useful, since it provides a basis invariant description of the scatterer. According to this method, the coherency matrix $\mathbf{T}$, which is a Hermitian positive semidefinite matrix, can be unitarily diagonalized by a unitary matrix with non-negative eigenvalues as follows.

$$\mathbf{T} = \mathbf{U}\boldsymbol{\Sigma}\mathbf{U}^{-1}, \tag{2.8}$$

where $\boldsymbol{\Sigma}$ is a 3×3 diagonal matrix with nonnegative real elements known as eigenvalues, and $\mathbf{U} = [\underline{u}1 \ \underline{u}2 \ \underline{u}3]$ is a 3×3 unitary matrix, where $\underline{u}1$, $\underline{u}2$, and $\underline{u}3$ are the three unit orthogonal eigenvectors.

By considering these eigenvectors as target vectors, a set of three uncorrelated targets can be obtained as shown below.

$$\mathbf{T} = \sum_{i=1}^{3} \lambda_i \underline{u}_i \cdot \underline{u}_i^{*T} = \mathbf{T}_{01} + \mathbf{T}_{02} + \mathbf{T}_{03}, \tag{2.9}$$

where λ_i is the i^{th} eigenvalue. The three independent targets $\mathbf{T}_{0i\,(i=1,2,3)}$, each of which represents a deterministic scattering mechanism associated with a single equivalent scattering matrix. The contribution from each deterministic scattering mechanism is specified by the corresponding eigenvalue λ_i, while the type of scattering is specified by the corresponding eigenvector $\underline{u}_i$.

Cloude was the first to consider such a decomposition [27], which is based on an algorithm that identifies the dominant scattering mechanism through extraction of the larger eigenvalues. This method provides a unique result. However, when these results are interpreted in terms of scattering mechanisms, some approximations have to be made [28].

Holm provided an alternative method to analyze the eigenvector spectrum. In this method, the target is interpreted as a sum of a single scattering **S** matrix (rank 1 coherency matrix) plus two noise or remainder terms. This is a hybrid approach, combining an eigenvalue based analysis with the concept of the target plus noise model of Huynen's approach [16]. This method decomposes the eigenvalues matrix $\mathbf{\Sigma}$ as follows.

$$\begin{aligned}\mathbf{\Sigma} &= \begin{bmatrix} \lambda_1 & 0 & 0 \\ 0 & \lambda_2 & 0 \\ 0 & 0 & \lambda_3 \end{bmatrix}_{\lambda_1 \geq \lambda_2 \geq \lambda_3} \\ &= \begin{bmatrix} \lambda_1 - \lambda_2 & 0 & 0 \\ 0 & 0 & 0 \\ 0 & 0 & 0 \end{bmatrix} + \begin{bmatrix} \lambda_2 - \lambda_3 & 0 & 0 \\ 0 & \lambda_2 - \lambda_3 & 0 \\ 0 & 0 & 0 \end{bmatrix} + \begin{bmatrix} \lambda_3 & 0 & 0 \\ 0 & \lambda_3 & 0 \\ 0 & 0 & \lambda_3 \end{bmatrix} . \\ &= \mathbf{\Sigma}_1 + \mathbf{\Sigma}_2 + \mathbf{\Sigma}_3 \end{aligned} \tag{2.10}$$

Then follows the Holm decomposition of the coherency matrix which is given by

$$\mathbf{T} = \mathbf{U}\mathbf{\Sigma}_1\mathbf{U}^{-1} + \mathbf{U}\mathbf{\Sigma}_2\mathbf{U}^{-1} + \mathbf{U}\mathbf{\Sigma}_3\mathbf{U}^{-1} = \mathbf{T}_1 + \mathbf{T}_2 + \mathbf{T}_3, \tag{2.11}$$

where $\mathbf{T}_1$ matrix represents a pure target as it has a single non-zero eigenvalue, $\mathbf{T}_3$ matrix represents noise as it has three nonzero eigenvalues which are equal and $\mathbf{T}_2$ matrix represents mixed target state.

2.1.3 Model-based decompositions

A third class of target decomposition techniques has been introduced by Freeman and Durden [29] which fits a physically based, three-component scattering model to the polarimetric SAR data. This decomposition technique decomposes the polarimetric covariance matrices into a sum of three covariance matrices. Here each decomposed covariance matrix corresponds to one of the three scattering mechanisms. The three basic scattering mechanisms are:

- volume scattering, modeled by a cloud of randomly oriented dipoles for tree canopy and vegetation;
- double bounce scattering, modeled by a dihedral corner reflector; and
- surface or odd bounce scattering, modeled by a first order Bragg surface scattering.

The contribution of odd, double bounce and volume scattering mechanism, viz. P_{odd}, P_{dbl} and P_{vol} can be estimated by the span or total scattered power P as:

$$P = P_{odd} + P_{dbl} + P_{vol}, \tag{2.12}$$

where

$$P = |S_{HH}|^2 + 2|S_{HV}|^2 + |S_{VV}|^2. \tag{2.13}$$

This model-fitting method has the advantage that it is based on the physics of radar scattering, and is not a purely mathematical construct. The results can be directly interpreted through the components covariance matrix.

One basic assumption of this scattering model is reflection symmetry, which limits its applicability to only reflection symmetric targets. For example, the reflection symmetry condition does not hold for scattering from an urban area. To circumvent this problem, Yamaguchi et al. [30] proposed a four-component scattering model by introducing an additional term corresponding to non reflection symmetric cases: $\langle S_{HH}S_{HV}^*\rangle \neq 0$ and $\langle S_{VV}S_{HV}^*\rangle \neq 0$.

In 2007, Freeman proposed a two component scattering model for polarimetric SAR observations of forest areas [31]. The two mechanisms are canopy scattering from randomly oriented dipoles, and a ground scatter term that either represents double-bounce scatter or Bragg surface scatter. The contribution of Bragg surface and volume scattering mechanism, viz. P_G and P_v are estimated by the span or total scattered power P as:

$$P = P_G + P_V. \tag{2.14}$$

2.1.4 Coherent target decomposition

A fourth class of target decomposition theorems is based on coherent decomposition of scattering matrix. Coherent decomposition is more suitable for pure targets which can be described by a scattering matrix. The objective of the coherent target decomposition technique is to express the scattering matrix as a combination of basis matrices, where an elementary scattering mechanism is associated to each basis matrix. Some examples of coherent decomposition techniques are Pauli, Krogager, and Cameron decompositions [16, 19]. Here, we will review only Pauli decomposition technique which is by far the most frequently used algorithm by the polarimetric radar community.

Pauli decomposition expresses the scattering matrix $\mathbf{S}$ as the coherent sum of the Pauli matrices, where an elementary scattering mechanism is associated to each basis matrix [19].

$$\mathbf{S} = \begin{bmatrix} S_{HH} & S_{HV} \\ S_{VH} & S_{VV} \end{bmatrix} = \frac{a}{\sqrt{2}} \begin{bmatrix} 1 & 0 \\ 0 & 1 \end{bmatrix} + \frac{b}{\sqrt{2}} \begin{bmatrix} 1 & 0 \\ 0 & -1 \end{bmatrix} + \frac{c}{\sqrt{2}} \begin{bmatrix} 0 & 1 \\ 1 & 0 \end{bmatrix} + \frac{d}{\sqrt{2}} \begin{bmatrix} 0 & -j \\ j & 0 \end{bmatrix} \tag{2.15}$$

where a, b, c, and d are all complex and are given by

$$a = \frac{S_{HH} + S_{VV}}{\sqrt{2}},\ b = \frac{S_{HH} - S_{VV}}{\sqrt{2}},\ c = \frac{S_{HV} + S_{VH}}{\sqrt{2}},\ \text{and } d = j\frac{S_{HV} + S_{HV}}{\sqrt{2}}. \tag{2.16}$$

The interpretation of Pauli decomposition is done according to the matrices in the basis. Pauli decomposition of targets may be considered as the coherent composition of four scattering mechanisms. The first matrix corresponds to odd-bounce scattering, the second and the third matrix correspond to scattering mechanism of a dihedral with a relative orientation of 0^0 and 45^0, respectively, and the last matrix corresponds to all the antisymmetric components of the scattering matrix.

2.2 Landcover classification using PolSAR images

Classification of earth surface types is one of the important applications of radar based remote sensing. Polarimetric SAR imagery provides a day-and-night, all-weather and all polarization mapping capabilities, which are required for landcover classification. The aim of landcover classification is to categorize all the pixels in a digital image into one of the several landcover classes. Many such classification techniques are supervised in the sense that training datasets are used to do the signature analysis and based on that a statistical decision is taken to determine which class a pixel from a test image belongs to. However, it is often difficult to obtain useful training datasets. Therefore, several unsupervised techniques have been developed which classify the image automatically by finding clusters based on a given strategy. Different supervised and unsupervised polarimetric classification procedures are outlined in some of the classic review papers [24, 32]. Combinations of the supervised and unsupervised classification techniques were also reported in literature to enhance the classification accuracy further [33–35]. In the present context, only the unsupervised algorithms, based on physical scattering characteristics, are reviewed.

Van Zyl was the first to introduce an unsupervised classification technique based on the scattering mechanism of each pixel in an image [7]. This algorithm compares the polarization properties of each pixel in an image to that of known scattering characteristics of single bounce, double bounce, and volume scattering. Based on this comparison, the pixel is classified into one of the four classes, viz. single bounce, double bounce, volume scattering, and a class for undetermined pixels. The comparison is based on the relationship of the orientation and handedness of the transmitted wave with the corresponding parameters of the scattered wave. The information, about the relationship between orientation and handedness of the transmitted wave with the corresponding parameters of the scattered wave, can directly be read from Mueller matrix. Therefore, an image may be classified into the four categories by comparing the Mueller matrix for every pixel in an image with the Mueller matrix for the three basic types of scattering, viz. single bounce, double bounce, and volume scattering. When this algorithm is implemented on an L band image of San Francisco datasets, it classifies the ocean and baresoil as single bounce; city blocks as double bounce, except for building oriented off the radar look direction; forest, park area and vegetation as diffuse scattering. Therefore, this algorithm can be used for terrain type identification and classification.

A fast analytical procedure was proposed in [17], which can compute the maximum and minimum value of the degree of polarization, (p_{max} and p_{min}), and the total scattered intensity (R_{max} and R_{min}). From these four values, different discriminators such as the coefficient of variation (V) ([22]), the fractional polarization (F), the dynamic range of degree of polarization Δp and the span can be obtained as follows.

$$\begin{aligned} V &= \tfrac{p_{\min}}{p_{\max}} \\ F &= \tfrac{p_{\max}-p_{\min}}{p_{\max}+p_{\min}} \\ \Delta p &= p_{\max} - p_{\min} \\ \text{span} &= R_{\max} + R_{\min} \end{aligned} \tag{2.17}$$

A classification based on maximum degree of polarization (p_{max}) and Δp is introduced in [17]. The p_{max} is used to identify the type of scattering mechanism, whereas Δp measures the complexity of scattering mechanisms.

One of the successful unsupervised classification techniques was proposed by Cloude and Pottier in [36], which classifies the image into more number of scattering categories. This classification technique is based on two parameters, viz. entropy (H) and alpha angle (α). The entropy and alpha parameters are derived from an eigenvector decomposition of the target coherency matrix [19]. Entropy provides information about the degree of randomness of a scattering phenomena. Alpha angle identifies the dominant scattering mechanism. All random scattering mechanisms can be represented in the H/α plane. For classification, H/α plane is divided into nine zones or classes of different dominant physical scattering characteristics. However, the classification results are not satisfactory in some cases, due to the fact that not all the polarimetric information contained in the target coherency matrix have been used. Lee et al. [34] introduced a combined use of unsupervised classification based on H/α and supervised maximum likelihood (ML) classifier based on complex Wishart distribution to improve the classification accuracy. The classified pixels in each zone in the H/α plane are taken as an initial training set for classification based on complex Wishart distribution. The classification results are then used as training sets for the next iteration. To enhance the discrimination capability of the technique further, zones are further subdivided into two zones based on the pixel's anisotropy (A) value. This Wishart-$H/A/\alpha$ [33] constitutes a complete landcover classification scheme. A detailed survey of entropy based landcover classification schemes is provided later in Section 3.1.

An unsupervised classification technique may be developed by using Freeman and Durden decomposition technique [37]. Pixels are divided into three scattering categories, viz. double bounce, single bounce, and volume scattering, based on the dominance in backscattering power of each scattering mechanisms, as illustrated below.

$$A\ pixel \in \begin{cases} Cluster_{odd},\ if\ P_{odd} = \max\{P_{odd}, P_{dbl}, P_{vol}\} \\ Cluster_{dbl},\ if\ P_{dbl} = \max\{P_{odd}, P_{dbl}, P_{vol}\} \\ Cluster_{vol},\ if\ P_{vol} = \max\{P_{odd}, P_{dbl}, P_{vol}\} \end{cases} \tag{2.18}$$

To further improve the classification performance, Lee et al. [37] proposed an unsupervised classification algorithm based on the combined use of this classification technique with the ML classifier based on complex Wishart distribution. This combined technique preserves the dominant scattering mechanism, and has better stability in convergence than the Wishart-H/α technique. In comparison to Wishart-H/α technique, this technique also has the flexibility in terms of choosing the number of classes. The algorithm initially classifies the pixels into the three categories by Equation 2.18. Then the pixels in each category are distributed equally into 30 clusters based on the backscattering power of the corresponding scattering mechanisms. A new and efficient class initialization scheme was proposed in [37] to merge clusters based on the between-cluster Wishart distance measure. The merged clusters in each category are used to initialize the training sets for the corresponding Wishart based classifiers for that category. All Pixels are iteratively classified by the Wishart classifier within each scattering category. Finally, an automated colour rendering scheme based on the scattering category of classes was proposed in [37], which colours the classification map.

2.3 Hybrid-PolSAR configurations

Now a days, there has been a growing interest in dual-Pol systems. In comparison to quad-Pol system, dual-Pol systems have the advantage of halved average transmit power, doubled swath coverage and less complexity. However, dual-Pol systems can not contain as much information as quad-Pol systems. Hence, it is quite necessary to understand the amount of information content of these dual-Pol systems, as compared to quad-Pol system. Souyris et al. have demonstrated that dual-Pol SAR systems can reproduce aspects of fully polarimetric data based on few simple assumptions [38]. They have introduced a radar scattering model to construct pseudo quad-Pol data from $\Pi/4$ mode data. However these models make two assumptions which limit their applicability to azimuthally symmetric scatterers only. However, the advantage with this method is that all the polarimetric tools developed for quad-Pol SAR image analysis can be applied to any dual-Pol modes by generating the corresponding pseudo quad-Pol data. A comparison of the information content between any dual-Pol mode and the corresponding pseudo quad-Pol data generated by using scattering model is carried out in [10]. In that work, it is reported that the classification accuracy of the pseudo quad-Pol data is the same as the classification accuracy obtained directly from the underlying dual-Pol data. A modified version of the radar scattering model is proposed in [9], which shows improvement over the original result in the construction of pseudo quad-Pol data. In the above work, a study of different dual-Pol modes was carried out to determine which dual-Pol configuration allows for superior reconstruction of the fully polarimetric data.

It is established in Section 1.1.5 that hybrid-Pol mode is the optimum configuration among different dual-Pol modes. Raney has promoted dual-Pol, in particular the use of the hybrid-Pol for its simpler architecture and benefits over other configurations. In his work [12, 39], he has shown that the analysis of hybrid-Pol data can be started from the Stokes parameters of the backscattered field for hybrid-Pol system.

$$G^s = \begin{bmatrix} G_0 \\ G_1 \\ G_2 \\ G_3 \end{bmatrix} = \begin{bmatrix} \left\langle |\underline{E}_{RH}|^2 + |\underline{E}_{RV}|^2 \right\rangle \\ \left\langle |\underline{E}_{RH}|^2 - |\underline{E}_{RV}|^2 \right\rangle \\ 2\mathrm{Re}\left\langle \underline{E}_{RH}\underline{E}_{RV}^* \right\rangle \\ 2\mathrm{Im}\left\langle \underline{E}_{RH}\underline{E}_{RV}^* \right\rangle \end{bmatrix}. \tag{2.19}$$

Here, $\underline{E}_{RH}$ and $\underline{E}_{RH}$ are the horizontal (H) and vertical (V) components of the backscattered field $\underline{E}$ for transmitted right-hand circular polarization (R) wave, respectively. The four-element Stokes vector captures all of the information of backscattered signals for hybrid-Pol system. Stokes parameters are linear combinations of the like-polarized power, the cross-polarized power, and the cross product between the complex image amplitudes in the two receive channels. Many secondary parameters, such as degree of polarization (DoP) m, relative phase δ, and circular polarization ratio μ_c can be derived from the Stokes parameters as follows.

$$m = \frac{\sqrt{G_1^2 + G_2^2 + G_3^2}}{G_0}. \tag{2.20}$$

$$\delta = a\tan\left(\frac{G_3}{G_2}\right). \tag{2.21}$$

$$\mu_c = \frac{G_0 - G_3}{G_0 + G_3}, \quad 0 \leq \mu_c. \tag{2.22}$$

In order to extract information from hybrid-Pol data, an $m-\delta$ decomposition of hybrid dual-Pol data is proposed by Raney in [12]. An unsupervised classification algorithm based on $m-\delta$ decomposition technique is developed in [40], which is capable of distinguishing the three basic scattering mechanisms, viz. single bounce, double bounce and volume scattering. The contribution of total backscattering power in odd bounce ($Phyb_{odd}$), double bounce ($Phyb_{dbl}$) and volume scattering ($Phyb_{vol}$) mechanisms can be estimated as follows.

$$\begin{aligned} P\_hyb_{odd} &= G_0 \cdot m \cdot \tfrac{(1+\sin\delta)}{2} \\ P\_hyb_{dbl} &= G_0 \cdot m \cdot \tfrac{(1-\sin\delta)}{2} \\ P\_hyb_{vol} &= G_0 \cdot (1-m) \end{aligned} \tag{2.23}$$

Pixels are then divided into the three categories, based on the dominance in backscattering power of each scattering mechanisms as shown in Equation 2.18. Chen et al. further improved the $m-\delta$ classification results by combining $m-\delta$ with span and Wishart classifiers [41]. Span is a rotation-invariant parameter which is equal to the first Stokes parameter G_0. Using the span value, each of the three classes are further divided into five classes, in such a way that all five classes contain equal number of pixels. The resulting 15 classes were then used as initial training set for complex Wishart classifiers.

In another work, Loi et al. provide an estimation of soil moisture and Faraday rotation from bare surface using hybrid-Pol data [42]. In their work, they have introduced a new coefficient, known as conformity coefficient, which can be estimated from hybrid-Pol data as:

$$\mu = 2\frac{\langle S_{HH}S_{VV}^{*}\rangle - |S_{HV}|^2}{|S_{HH}|^2 + |S_{VV}|^2 + 2\,|S_{HV}|^2}. \tag{2.24}$$

A major advantage with the μ parameter is that it is insensitive to Faraday rotation. This coefficient can also be used to discriminate between surface, volume and double bounce scattering by setting two threshold values, $t1$ and $t2$ as follows.

- Single bounce, if $1 > \mu > t1$.

- Double bounce, if $t2 > \mu > -1$.
- Volume scattering, if $t1 > \mu > t2$.

These thresholds have been set by using confusion matrices between the conformity coefficient and both H/α and Freeman−Durden classifications.

2.4 PolSAR image enhancement techniques

Radar images are affected by two types of noise, viz. speckle noise and the sidelobe noise. Speckle reduction in SAR imagery has been extensively reported in literature [43–47]. Speckle reduction in polarimetric SAR had been a current research topic and a lot of research work have been reported in literature [48–51]. In the current work, the thesis deals with PolSAR image enhancement through sidelobe noise removal techniques. There are different class of algorithms reported in literature to reduce sidelobe induced artifacts in SAR imagery.

One such class of algorithm is the CLEAN algorithm. The CLEAN algorithm was introduced in radio astronomy to reduce sidelobe-induced artifacts [52, 53]. In [54], for the first time, it was used as a technique to alleviate sidelobe artifacts in SAR images. An improved CLEAN algorithm for inverse SAR was proposed in [55], where enhanced recognizability of ISAR images is reported. The CLEAN algorithm separates large targets and their sidelobe responses by subtracting the point spread function of the receiving system. The implementation of CLEAN algorithm is given in Algorithm 1. The CLEAN technique has been extended to Polarimetric-CLEAN technique [56] that can extract the positions of scatterers in the presence of sidelobe noise. The position of scatterers can be used as a feature set for automated target classification.

A class of adaptive weighting functions and adaptive sidelobe reduction (ASR) algorithms that can be used to reduce sidelobes in SAR imaging, in a computationally efficient manner, is discussed in [57]. The key to ASR algorithm is the use of adaptive weighting functions which are defined as follows.

Algorithm 1 CLEAN algorithm

```
Require: An Fourier image $I$ and a noise threshold value $T$.
Ensure: The sidelobes are suppressed.
  Initialize variable $A$ with higher value than $T$
  while $A \geq T$ do
    Find the brightest spot in the image $I$.
    Measure its complex amplitude $A$ and position $x$, $y$.
    Calculate radiation field due to a source $A$ at location $x, y$.
    Subtract radiation field from $I$ and store it back in $I$.
    Save the location $x, y$ and amplitude $A$.
  end while
  Develop the list of targets at location $x$ and $y$.
  Form the final image by plotting a main lobe at each spatial location defined by location $x, y$ with amplitude $A$.
  The final image is free from sidelobe noise.
```

$$W\left(n,k\right) = 1 + \sum_{m=1}^{M} a\left(n,m\right)\cos\left(\frac{2\pi mk}{K}\right) \quad \text{for} \;\; k,n = 0 \text{ to } K-1 \tag{2.25}$$

These classes of algorithms are applicable to any problem involving spectral analysis.

A class of non linear techniques, known as non linear apodization (NLA), capable of completely suppressing the sidelobes in SAR imagery without broadening the mainlobe width was introduced in [58]. These NLA techniques have potential application in radar field [58] and a range of other fields [59,60]. There are different types of NLA techniques, viz. dual apodization (DA), complex dual apodization (CDA) and spatially variant apodization (SVA). A short review of NLA techniques is provided in Section (5.1). SVA is the most general NLA technique that eliminates the sidelobes completely. SVA is based on the use of special properties of cosine-on-pedestal weighting functions [61]. The cosine-on-pedestal function can be written as

$$A(n) = 1 + 2w\cos(\frac{2\pi n}{N-1}), \quad 0 < n \leq N-1. \tag{2.26}$$

This family of weightings range from $w = 0$ to $w = 0.5$. However, SVA technique can not be implemented on data sampled at non-integer multiples of Nyquist-frequency. To overcome this problem, a non-integer SVA algorithm was proposed in [62]. In this algorithm, a new frequency domain aperture function was introduced as

$$W(f) = a + 2\gamma \cos\left(\frac{\pi f}{f_s}\right), \tag{2.27}$$

where f_s is the sampling frequency and a and γ are two spatially variant parameters determined by this algorithm for each pixel. This algorithm provides reduction of sidelobes. However, a small amount of sidelobe energy is still leftover and is called residual sidelobes. To remove the residual sidelobes in case of non-integer SVA, a modified version of non integer SVA algorithm was developed in [63]. In the modified version of the algorithm, a constant phase p is added to non-integer Nyquist aperture functions to remove the residual sidelobes in the non-integer SVA algorithm. The modified form of the frequency domain aperture function is given by

$$W(f) = a + 2\gamma \cos\left(\frac{\pi f}{f_s} + p\right). \tag{2.28}$$

However, the modified version of the non-integer SVA algorithm could not remove all the residual sidelobes completely. It is able to remove only those residual sidelobes which are nearer to the mainlobe. Stankwitz *et al.* proposed a super-SVA technique for further enhancement in resolution based on image upsampling interpolation along with sidelobe suppressions [63, 64].

Another disadvantage with SVA algorithm is that it yields poor results when implemented on squinted SAR image. To overcome this a new SVA implementation was proposed in [65] that is able to suppress the sidelobes completely in squinted SAR image.

A class of apodization algorithm based on sidelobe rotation method is proposed in [66]. At first the sidelobes are rotated at different angels to uncover image information and then by combining the resultant images in an apodization scheme, the sidelobes in the image can be suppressed.

A class of sidelobe apodization using Kaiser window is proposed in [67], that yields sidelobe suppressed images when applied to SAR images. However in these algorithms, the computation of optimal window weighting function requires a substantial amount of computation.

2.5 Scope of the present work

Classification of earth surface types is one of the important remote sensing applications of radar polarimetry. At present, there is no unsupervised classification technique has been reported in the open literature that can discriminate different landcovers correctly and accurately. One of the widely used and most famous unsupervised classification techniques is Wishart-$H/A/\alpha$ algorithm. However, when this algorithm is implemented for crop type classification, it fails to correctly classify many types of crops. The above fact suggests that further investigations are required to develop unsupervised classification techniques for accurate crop types classification using polarimetric SAR images.

Recently, there has been a growing interest in dual-polarimetric (dual-Pol) systems. In comparison to quad-Pol system, the dual-Pol system has the advantage of halved average transmitted power and doubled swath coverage. However, dual-Pol systems use only half of the space of polarization information provided by fully polarimetric SAR. Therefore, no dual-Pol systems contain as much information as quad-Pol systems. Hence, it is quite necessary to understand the amount of information content of dual-Pol systems, as compared to quad-Pol system. In Section 1.1.5, it was learnt that hybrid-Pol mode is the optimum architecture among all dual-Pol modes. Presently, there are few methods available in literature for the analysis of hybrid-Pol data as reviewed in Section 2.3. This gives us the motivation to carry out further analysis of hybrid-Pol data. The thesis investigate possible ways of analyzing the hybrid-Pol data to extract information from hybrid-Pol images.

Generally, Classification and segmentation algorithms perform better if noise is removed from the image to be classified. Though several works have been reported in literature on speckle reduction, there is little effort in the direction of sidelobe noise suppression in SAR and PolSAR images. Also the sidelobe suppression techniques originally developed for SAR imagery have not been extended to PolSAR images. From the literature survey, it is observed that, presently, there is no algorithm that can suppress the sidelobes completely and simultaneously reduce the mainlobe width to further enhance the resolution when implemented on images sampled at non integer multiple of Nyquist rate. The present thrust is to formulate a simple algorithm which can completely wipe out the sidelobes and simultaneously reduce the mainlobe width to further enhance the resolution when implemented on SAR images sampled at non integer or unknown multiples of Nyquist rate. In this thesis, we address these issues.

3

Landcover Mapping and Crop Classification Using PolSAR Images

Contents

Anthropogenic changes in landcover is one of the alarming factors affecting global ecology. Therefore the importance of acquiring complete, accurate and timely landcover information has grown over the years with the increasing concern about the ecological changes. Landcover classification is one of the major remote sensing applications of radar polarimetry and has been a subject of recurring interest for the last few decades. Several techniques have been developed, recently, to correctly classify different landcover types. Various methods for supervised and unsupervised landcover classification have been reported in literature [24]. An unsupervised classification scheme based on the use of polarimetric entropy and alpha angle is widely used for land cover classification. In this chapter, we propose three different landcover classification algorithms. These three algorithms are similar in principle to entropy/alpha based landcover classification scheme. We have shown that these algorithms perform better than the classic entropy/alpha based classification scheme in terms of classification accuracy and computational cost. The performance analysis of the proposed techniques are carried out using NASA/JPL AIRSAR L band datasets for San Francisco bay, USA and Flevoland, The Netherlands. The San Francisco data covers a mixture of ocean, urban, and vegetation land covers [7]. This dataset is used for terrain type classification. The Flevoland data covers a large agricultural area of horizontally flat topography and homogeneous soils. It contains several classes of crops and three other classes of bare soil, water, and forest [19]. This dataset is used for crop type classification and identification.

The rest of the chapter is organized as follows. In the next section, a brief description about entropy based landcover classification technique is provided. The three proposed algorithms are discussed in Sections 3.2, 3.3 and 3.4, respectively. Section 3.5 gives summary of the work presented in this chapter.

3.1 An entropy based landcover classification scheme

One of the successful unsupervised classification techniques based on entropy (H) and alpha angle (α) was proposed in [36]. The entropy and alpha parameters are derived from an eigenvector based decomposition of the target coherency matrix $\mathbf{T}$ [19]. According to this method, the coherency matrix can be decomposed as follows.

$$\mathbf{T} = \sum_{i=1}^{3} \lambda_i \underline{u}_i \cdot \underline{u}_i^{*T}, \tag{3.1}$$

where λ_i and $\underline{u}_i$ are the eigenvalues and eigenvectors of the coherency matrix, and $\underline{u}_i$'s are given by

$$\underline{u}_i = e^{j\phi_i} \begin{bmatrix} \cos\alpha_i & \sin\alpha_i \cos\beta_i e^{j\delta_i} & \sin\alpha_i \sin\beta_i e^{j\gamma_i} \end{bmatrix}^T, \tag{3.2}$$

where α corresponds to different scattering mechanisms, β angle is twice the polarization orientation angle, ϕ_i's are equivalent to target absolute phases and δ and γ are the phase differences of second and third terms relative to the first term.

Depending upon the scatterer types, the eigenvalues are different. Here, we consider three types of scatterers and find out the corresponding eigenvalues.

Case 1: For pure target, the coherency matrix has only one non zero eigenvalue.

Case 2: For distributed or random target, the coherency matrix has non zero and equal eigenvalues.

Case 3: In between these two extremes lies the partial target. The coherency matrix of these targets has non equal and non zero eigenvalues.

From the eigenvalues and eigenvectors, two parameters, viz. entropy and alpha angle, are derived. The polarimetric entropy H, which is used to measure the target disorder is given by

$$H = -P_1 \log P_1 - P_2 \log P_2 - P_3 \log P_3, \tag{3.3}$$

where P_1, P_2, and P_3 are the pseudo-probabilities. These pseudo-probabilities are defined as

$$P_i = \frac{\lambda_i}{\sum\limits_{j=1}^{3} \lambda_j}, \text{ for } i = 1, 2, 3. \tag{3.4}$$

Entropy values for various scatterer types are:

Case 1: For pure target, entropy is equal to 0.

Case 2: For distributed target, entropy is equal to 1.

Case 3: For partial targets, entropy is in between 0 to 1.

All the three eigenvalues of the coherency matrix are roll-invariant and hence, the pseudo-probabilities are also roll-invariant. It then follows that the polarimetric entropy is also a roll-invariant parameter. This is one of the major advantages of entropy, as this property ensures that this parameter is independent of the orientation of targets about the line of sight. The drawback with entropy parameter is that if any of the eigenvalues is zero, then the corresponding P_i becomes zero and hence entropy cannot be evaluated. For that reason a small absolute value is added to P_i which results in a small amount of error in the analysis of polarimetric SAR data.

Alpha angle is obtained from the α_i angle of each eigenvector as follows.

$$\alpha = \sum_{i=1}^{3} P_i \alpha_i. \tag{3.5}$$

Alpha angle denotes the average or dominant scattering mechanism. $\alpha = 0^0$ indicates surface scattering, $\alpha = 45^0$ indicates volume scattering, while $\alpha = 90^0$ represents a dihedral scattering from metallic surfaces [68].

Cloude and Pottier proposed an unsupervised classification scheme based on the use of the H/α plane [36]. All random scattering mechanisms can be represented in this H/α plane. However because of spatial averaging, not all regions are equally populated. There are bounds on the maximum and minimum values of alpha angle that can be obtained for a particular value of entropy. For example, when H=1 there is only one possible value for alpha and for zero entropy, alpha can take any value in between 0^0 to 90^0. The possible variations of alpha as a function of entropy is defined by curve I and II, as shown in Figure 3.1. The curve I and II are determined by the H/α variation for a coherency matrix with degenerate minor eigenvalues varying in between 0 to 1. The feasible region in H/α plane is bounded by these two curves. These two curves tend to the same alpha point (60^0)

for maximum entropy $H = 1$. From this figure, it can be seen that the possible choices of alpha reduces as entropy increases. This means the discrimination capability of this classification scheme reduces as underlying entropy increases. The H/α classification space was sub-divided into nine basic classes of different scattering behavior, out of which eight zones lie in the feasible region. These nine zones are numbered as Z1 to Z9. Pixels in a particular zone belong to a class associated with that zone. The location of the boundaries within the permitted H and α space is set based on the general properties of the scattering mechanisms. The physical scattering characteristics of each of the nine zones are outlined in [36]. The classification map alongside the pixels distribution in H/α plane for San Francisco area are shown in Figure 3.2.

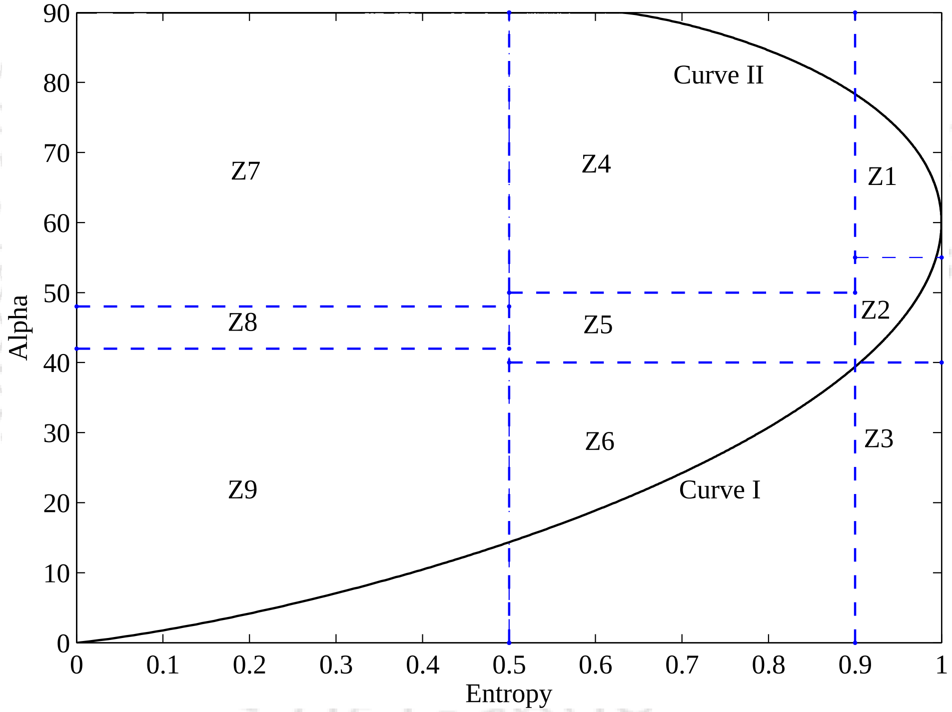

Figure 3.1: Feasible region in H/α classification plane.

3.1.1 Wishart-H/α classification technique

The H/α classification technique is used to segment the image in terms of physical scattering mechanisms. However, the classification results are not satisfactory in some cases, due to the fact that not all the polarimetric information contained in the target coherency matrix has been used. Also the fixed linear decision boundaries in the H/α plane greatly affect the classification results. A cluster may fall on a boundary or may not be confined in a single zone. Besides, it may be possible that a group of clusters may be enclosed in the same zone.

Therefore to improve the classification accuracy, a combined use of unsupervised classification based on H/α and supervised algorithm based on statistics of the coherency matrix has been introduced in [34]. This supervised algorithm is a maximum likelihood (ML) classifier based on the complex Wishart distribution for the coherency matrix. The complex Wishart distribution of coherency matrix is given by [34]

$$p_T^{(n)}\left(\langle \mathbf{T} \rangle\right) = \frac{n^{qn} \left|\langle \mathbf{T} \rangle\right|^{n-q} \exp\left[-n\mathrm{Tr}\left(V^{-1}\left\langle \mathbf{T} \right\rangle\right)\right]}{K\left(n,q\right)\left|V\right|^{n}}, \tag{3.6}$$

where

$$K\left(n,q\right) = \pi^{\left(\frac{1}{2}\right)q(q-1)}\Gamma\left(n\right)...\Gamma\left(n-q+1\right). \tag{3.7}$$

Here, $q = 3$ is the case for monostatic backscattering, $\mathrm{Tr}(\cdot)$ and $|\cdot|$ denote the trace and determinant of a matrix, n is the number of looks and K is a normalization factor and $V = E[\langle \mathbf{T} \rangle]$.

The classified pixels in each zone of H/α plane are taken as an initial training set for classification based on complex Wishart distribution. The classification results are then used as training sets for the next iteration. Improvements in classification accuracy through each iteration has been observed as the cluster centers in the H/α plane are updated after each iteration. The iteration stops when the number of pixels, switching classes, becomes smaller than a predetermined value, or when other termination criteria are met [34]. The classification results of the combined technique (Wishart-H/α) is shown in Figure 3.3(a). The Wishart-H/α technique gives better classification results over H/α technique. Grass fields and city blocks are much clearly defined. The minute details such as polo field and golf course which were indistinguishable in H/α classification map (Figure 3.2(b)), are more clearly visible now.

3.1.2 Wishart-H/A/α classification technique

To further improve the classification accuracy, the Wishart-H/α technique has been extended and complemented by the use of polarimetric anisotropy (A). It is obtained using the second and third eigenvalues as [16]

$$A = \frac{\lambda_2 - \lambda_3}{\lambda_2 + \lambda_3}, \text{ if } \lambda_1 > \lambda_2 > \lambda_3. \tag{3.8}$$

Since the eigenvalues are rotational invariants, the polarimetric anisotropy A is also a roll-invariant parameter. The discrimination capability is further enhanced by subdividing the zones into two zones based on pixel's anisotropy value greater or smaller than 0.5. This increases the number of feasible classes from 8 to 16 [16]. These 16 classes were then used as initial training set for complex Wishart classifiers. Then the same procedure as explained in Section 3.1.1 is followed, the only difference is being that now entropy/anisotropy/alpha ($H/A/\alpha$) is used as the initial training set for classification based on complex Wishart distribution [33]. The combined strategy is referred to as Wishart-$H/A/\alpha$ classifier. The classification results of the combined technique (Wishart-$H/A/\alpha$) is shown in Figure 3.3(b). Further improvement in classification of details can be observed, particularly in city blocks and in ocean areas.

3.2 A Gini-index based landcover classification scheme

In this section, we report improved classification accuracy by introducing a new parameter, i.e. Gini-index (G) [69, 70] as an alternative to entropy parameter in entropy/alpha classification scheme. It also overcomes the drawback of entropy calculation and the computation is simpler as it does not involve logarithmic operation. In many fields, particularly in economics, Gini-index has been used to measure the dispersion of a distribution [69]. In literature, this index is also known as coefficient of concentration. Gini-index for PolSAR is defined as follows [70].

$$G = 0.5 \left(1 - \sum_{i=1}^{3} P_i^2 \right), \tag{3.9}$$

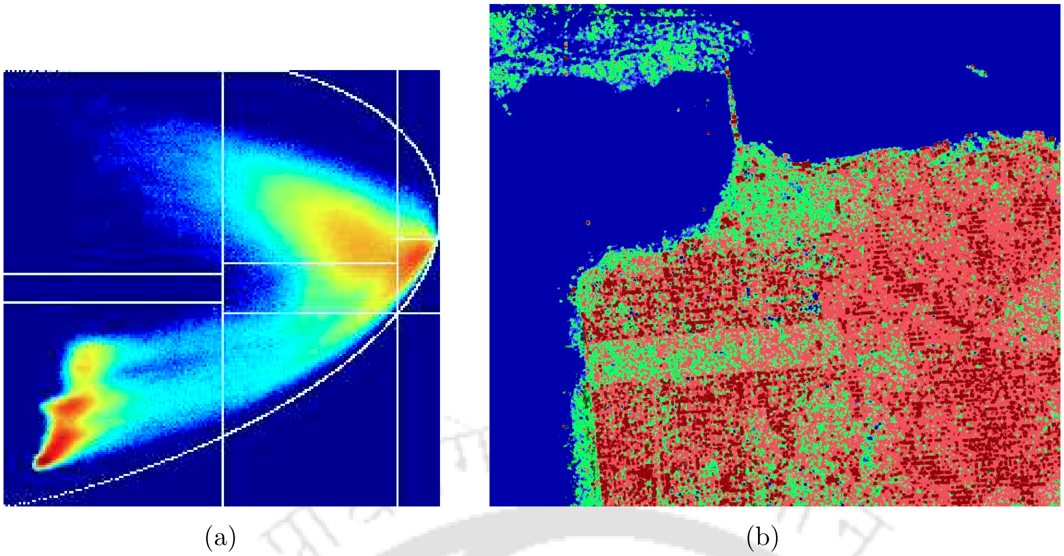

Figure 3.2: (a) H/α occurrence plane and (b) H/α classification map.

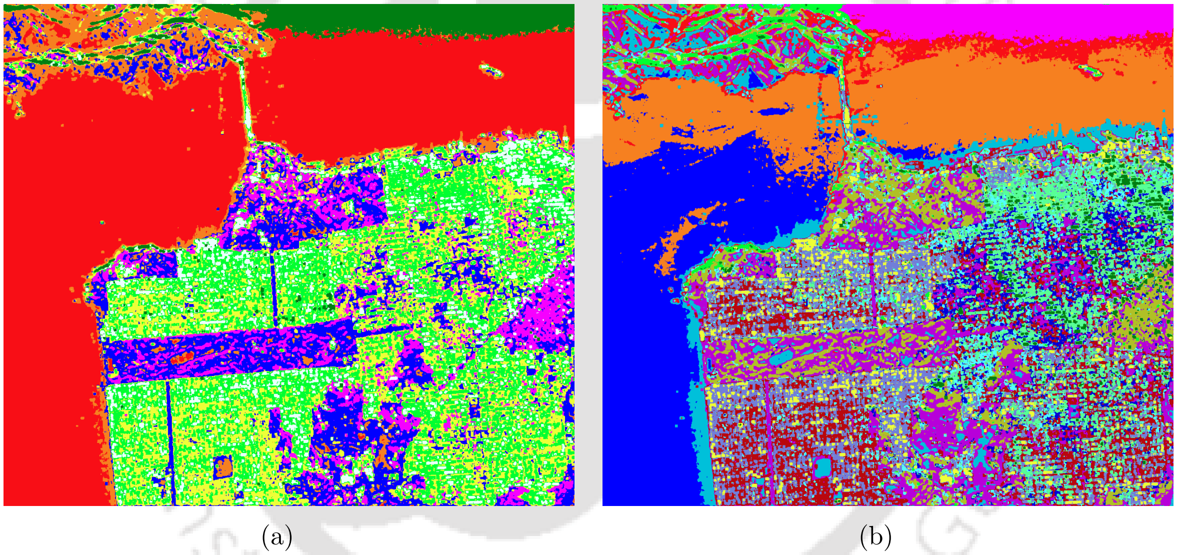

Figure 3.3: Classifications results of (a) Wishart-H/α and (b) Wishart-$H/A/\alpha$ after two iterations.

where P_i's are the pseudo-probabilities. For various scatterer types, the Gini-index value is evaluated as follows.

Case 1: For pure target, Gini-index is equal to 0.

Case 2: For distributed target, Gini-index is equal to 1/3.

Case 3: For partial targets, Gini-index is in between 0 to 1/3.

To make the same extreme value as of entropy, we modify the formula for Gini-index as

$$G_i = 1.5\left(1 - \sum_{i=1}^{3} P_i^2\right). \tag{3.10}$$

Where (G_i) is the modified Gini-index. Now onwards we will be using this modified Gini-index and we still call it as Gini-index (G) to maintain the simplicity. Like entropy, Gini-index is also a roll-invariant parameter.

3.2.1 The proposed landcover classification scheme

Using Gini-index and alpha angle, we propose an unsupervised classification technique similar to H/α classification technique. The definition of alpha angle remains the same as before. The G/α classification plane is sub-divided into nine zones of different scattering behaviors. The proposed land cover classification scheme is based on the combined use of Gini/alpha with anisotropy A and Wishart classifications. Here, we use Gini/anisotropy/alpha ($G/A/\alpha$) instead of ($H/A/\alpha$) as the initial training set for classification based on complex Wishart distribution. This new combination is referred to as Wishart-$G/A/\alpha$ classifier.

3.2.1.1 Results and observations

The entropy and Gini-index parameters are evaluated for San Francisco data and plotted in Figures 3.4 and 3.5, respectively. From these figures, it can be observed that the ocean part is more clearly distinguished in the Gini-index image. A general function that relates entropy and Gini-index is plotted in Figure 3.6. In this figure, one can observe that entropy value is always larger than Gini-index value for lower values of entropy. For higher values of entropy, both the parameter values are comparable. Usually the lower entropy values correspond to surface scattering and the higher entropy values correspond to volume scattering. So we expect a significant change in surface scattering and a small change in volume scattering, if Gini-index is used instead of entropy in H/α classification.

To validate the above hypothesis, H/α and the proposed G/α schemes are evaluated on the Flevoland dataset for crop classification. The H/α and G/α classification maps are shown in Figures 3.7(a) and 3.7(b), respectively. The corresponding pixel distributions in these classification planes along with the colour code of each zones are shown in Figures 3.8(a) and 3.8(b), respectively. Here, we considered the RGB colour coded Pauli image as the ground truth, which is shown in Figure 3.7(c). The relative performance of G/α and H/α classification schemes may be evaluated by comparing the corresponding classification maps with the ground truth. To facilitate the comparison, we have marked four regions #1, #2, #3 and #4 on Figures 3.7(a), 3.7(b) and 3.7(c). On comparing the corresponding regions, one may observe that G/α's performance is better in the violet-coloured regions. It can be observed that the regions with ocean surfaces or slightly rough earth surfaces are represented by violet colour. Therefore, it may be inferred that the Gini-index based classification scheme performs better for specular scattering and Bragg surface scattering. The other coloured regions in both the Figures 3.7(a) and 3.7(b) remains almost unchanged. Hence, the performances of both the classification techniques for volume scattering remain the same. To validate this, we obtain entropy and Gini-index as a function of scattering order in volume backscatter [36]. As the scattering order increases, the backscattered signal becomes more depolarized and entropy value reaches to 1. The comparison of these two parameters is shown in Figure 3.9. From this figure, it is apparent that the performances of both Gini-index and entropy for volume backscattering are almost the same.

To study the change in pixel distribution quantitatively, the confusion matrix for H/α and G/α's segmented zones was obtained as shown in Table 3.1. Each row shows the percentage of pixels in one particular zone moved from that zone to all other zones. Most of the pixels in each zone in the H/α plane have been branded into the corresponding zones in the G/α plane. However, the mapping from Z2 to Z2 and Z6 to Z6 is not good. In fact, 10.28% (78930 numbers of pixels) of the total pixel are reclassified into zones other than the originating zones. Out of differently reclassified pixels, 89% (70284 numbers of pixels) of pixels has moved from Z6 to Z9 zone. This validates that G/α's performance is different from H/α in case of surface scattering. The G/α plot may be interpreted as if pixels were moving towards lower entropy values in H/α plot. Only 0.24% (191 numbers

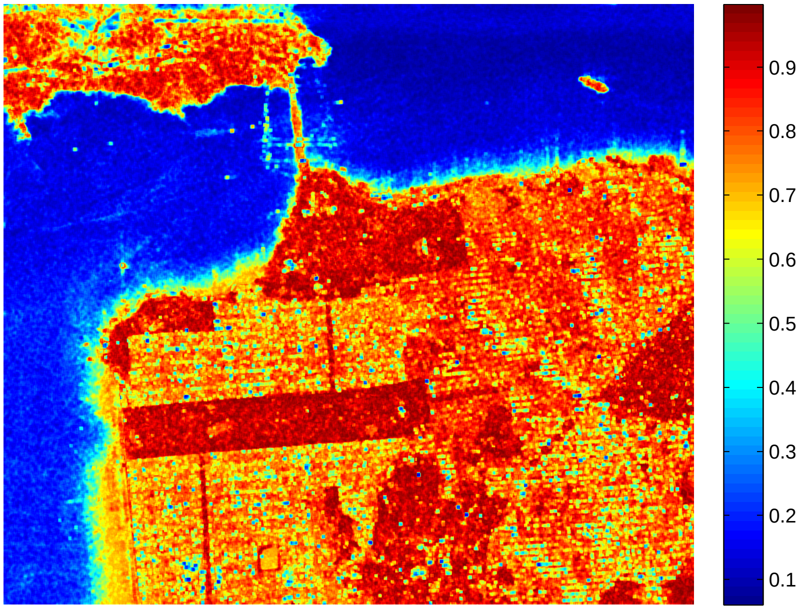

Figure 3.4: Entropy H: San Francisco data.

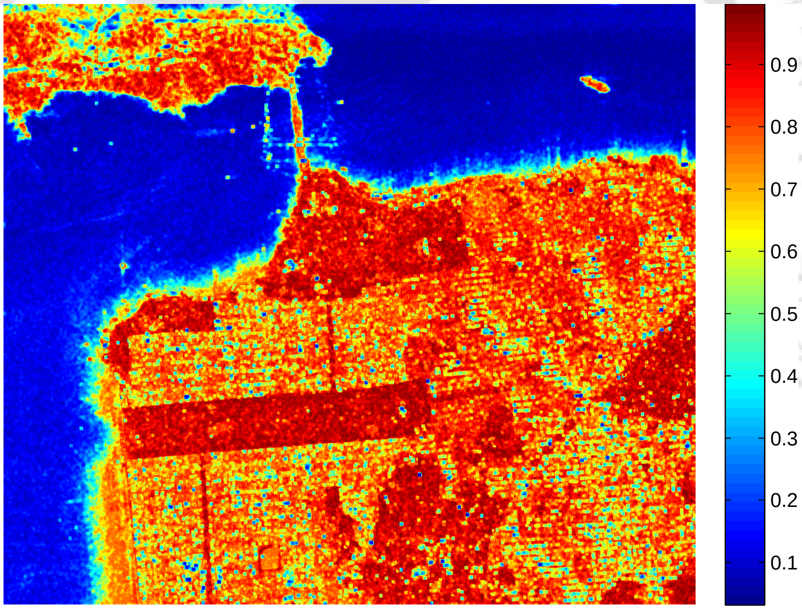

Figure 3.5: Gini-index G: San Francisco data.

of pixels) of reclassified pixels are moving towards larger entropy values. As the entropy value of the pixels decreases, the scattering mechanisms are more easily distinguished. Therefore Gini/alpha based land cover classification technique performs better than the

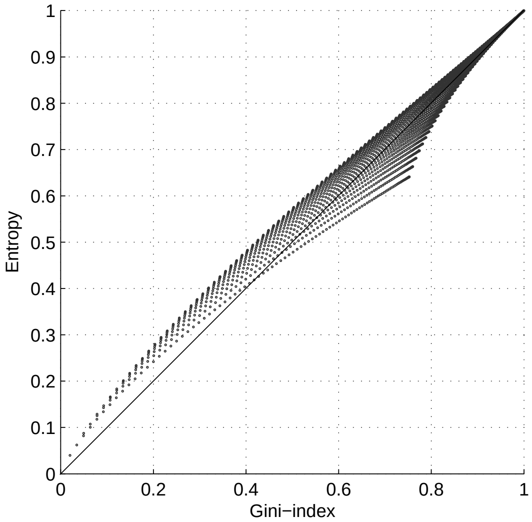

Figure 3.6: Pixels distribution in the Entropy/Gini space.

classic entropy/alpha based land cover classification technique.

Table 3.1: Confusion matrix for H/α and G/α's segmented zones.

$G/\alpha \backslash H/\alpha$	Z1	Z2	Z4	Z5	Z6	Z7	Z8	Z9
Z1	92.9	0	7.1	0	0	0	0	0
Z2	0	80.07	1.08	18.22	0	0	0	0
Z4	0.03	0.51	98.22	0	0	1.24	0	0
Z5	0	0.08	0	99.79	0	0.02	0.06	0.05
Z6	0	0	0	0	83.4	0	0	16.6
Z7	0	0	0	0	0	1	0	0
Z8	0	0	0	0	0	0	1	0
Z9	0	0	0	0	0	0	0	1

To further evaluate the performance of both the classification techniques, the combination of supervised and unsupervised technique as discussed in Section 3.1.2 is used. The results of Wishart-$H/A/\alpha$ and Wishart-$G/A/\alpha$ after 10 iterations are shown in Figures 3.10(a) and 3.10(b), respectively. The same colour code as shown in Figure 3.10(c) has been used throughout the iterations. The results can be compared with the ground truth map, which is shown in Figure 3.10(d) [71]. The size of the ground truth area is 400×300 pixels. There are seven identified crop classes and one class of bare soil in the ground truth image [71]. This ground truth area is marked in both the Figures 3.10(a) and 3.10(b). Upon comparison of the marked areas in these figures with the ground truth separately, one can observe that Wishart-$G/A/\alpha$ scheme is in better agreement with the ground truth as compared to Wishart-$H/A/\alpha$ scheme.

Percentage of different classes correctly classified in Wishart-$G/A/\alpha$ and Wishart-$H/A/\alpha$ schemes in comparison to the ground truth is given in Table 3.2. From inspection of Table 3.2, the following observations can be made.

Table 3.2: Percentage of different classes correctly classified by Wishart-$G/A/\alpha$ and Wishart-$H/A/\alpha$ methods in comparison to the ground truth. If a class is not correctly classified, we mark it as ×.

Class type	Wishart-$G/A/\alpha$	Wishart-$H/A/\alpha$
Potato	92.17	77.30
Lucerne	86.67	44.56
Pea	80.49	78.43
Beet	59.05	75.08
Bare Soil	×	×
Barley	×	×
Rape seed	×	×
Wheat	×	×

- Potato, lucerne and pea are more correctly classified by the proposed method (Wishart-$G/A/\alpha$).
- For beets, Wishart-$H/A/\alpha$'s performance is better.
- Wheat is often confused with rape seed and both the techniques fail to correctly classify them.
- Similarly bare soil and barley are misclassified as belong to the same class.

However, if we consider wheat and rape seed as a single class, then they are more correctly classified by the proposed classification scheme. Similarly, bare soil and barley together is more correctly classified by the proposed classification scheme.

3.3 Analysis of different entropies based landcover classification schemes

Even though the proposed Gini-index based classification algorithm performs better than entropy based classification algorithm in crop type discrimination, it fails in correctly classifying all types of crops. When this scheme is applied to Flevoland PolSAR datasets, some crops such as rape seed, barley, and potato are not correctly classified by Gini-index based classification scheme. So, there is a need to develop an algorithm that will correctly discriminate all type of crops. From Section 3.2.1.1, it has been learnt that as the entropy value of the pixels decreases, the scattering mechanisms are more easily distinguished. This led us to search for more entropy like parameters that can move pixels more towards the lower entropy region in the entropy/alpha plane. Entropy in the classic entropy based classification scheme is the Shannon entropy. However, there are different versions of Shannon entropy reported in literature that we are going to discuss next.

3.3.1 Different forms of entropy

In the early 1850s, Rudolf Clausius set forth the concept of entropy in the context of classical thermodynamics. The name “entropy” is derived from the Greek word *en-trepein*, meaning energy turned to waste. Entropy is the quantitative measure of the degree of uncertainty, which exists in a system. Although entropy was originally a thermodynamic concept, it has been used in other fields of study, including information theory, psychodynamics, economics, and evolution. In information theory, entropy is a measure of the uncertainty associated with a random variable and is usually referred to as Shannon entropy.

Definition of Shannon entropy: Let $P = (p_1, p_2, ..., p_n)$ *be a finite discrete probability distribution, that is, suppose* $p_k \geq 0, \texttt{for}\ k = 1, 2, ..., n\ \texttt{and} \sum_{k=1}^{n} p_k = 1$. *The amount of uncertainty of the distribution* P, *that is, the amount of uncertainty concerning the outcome of an experiment, the possible results of which have the probabilities* $p_1, p_2, ..., p_n$, *is called the entropy of the distribution* P *and is usually measured by the quantity* $H[P] = H(p_1, p_2, ..., p_n)$ *, is defined by* [72]

$$H\left(p_1, p_2, ..., p_n\right) = \sum_{k=1}^{n} p_k \log_2 \frac{1}{p_k}. \tag{3.11}$$

The entropy parameter is characterized by a set of postulates given by Fadeev [72]. These postulates are as follows.

- Symmetry: $H(p_1, p_2, ..., p_n)$ is a symmetric function of its variable for $n = 2, 3, ...$
- Continuity: $H(p, 1-p)$ is a continuous function of p for $0 \leq p \leq 1$
- Maximum: $H(0.5, 0.5) = 1$
- Additivity: $H[t \times p_1, (1-t) \times p_2, ..., p_n] = H(p_1, p_2, ..., p_n) + p1 \times H(t, 1-t)$

As a matter of fact, there can be many quantities other than entropy if the fourth postulate is relaxed to a weaker requirement. A generalization of Shannon entropy, the Rényi entropy, is one of a family of functionals for quantifying the randomness of a system. It is named after Alfréd Rényi [72].

Rényi entropy of order β, where $\beta \geq 0$ and $\beta \neq 1$, is defined as

$$R_\beta = \frac{1}{1-\beta} \log_2 \left(\sum_{i=1}^{n} p_i^\beta \right). \tag{3.12}$$

Rényi entropy tends to Shannon entropy as $\beta \rightarrow 1$ [73].

In statistical mechanics, Boltzmann-Gibbs entropy has been used to give a probabilistic definition of entropy [74]. It is defined as

$$S(\text{Boltzmann-Gibbs}) = -k \sum p_i \log p_i \tag{3.13}$$

where k is known as Boltzmann constant.

Tsallis proposed a generalization of the Boltzmann-Gibbs entropy [75,76]. This entropy has the form

$$T_q = \frac{1}{q-1} \left(1 - \left(\sum_{i=1}^{n} p_i^q \right) \right). \tag{3.14}$$

It can be easily checked that Tsallis entropy with $q = 2$ is the same as Gini-index.

3.3.2 Different entropies based landcover classification schemes

A comparative study of different entropies based landcover classification schemes is carried out. The motive here is to find the entropy index that provides the best landcover classification results. The two different generalized versions of entropy, viz. Tsallis entropy and Rényi entropy are considered here. A comparative study among Tsallis entropy and Rényi entropy based classification schemes is carried out separately. Finally, we compare among these two generalized versions of entropy and conclude. The performance of different entropies based classification algorithms are evaluated on the Flevoland data for crop classification.

3.3.2.1 Tsallis entropy based landcover classification

At first, a comparative study of different Tsallis entropies based landcover classification schemes is carried out. As shown in Equation (3.14), Tsallis entropy is a function of a variable q. Tsallis entropy with $q = 2$ ($T2$) is similar to Gini-index. In Section 3.2.1.1, it was observed that Gini-index based land cover classification technique performs better than the classic entropy based land cover classification technique. This is because almost all pixels have lower Gini value than entropy value. A comparative graph of entropy and Gini-index value was shown in Figure 3.6. In this figure, if the scatter plot is above the diagonal line, then the Gini value is smaller than the entropy value. As large part of the plot lying above the diagonal line, so for most of the pixels, entropy value is larger than the Gini-index value. Therefore, if entropy in entropy/alpha classification technique is replaced by Gini-index, the pixels moves towards the lower entropy region in H/α plane; thereby increasing the discrimination capability of this technique.

Next, a complete landcover classification with Tsallis entropy with $q = 3$ ($T3$) is developed. The values of $T3$ for various scatterer types are as follows.

Case 1: For pure target, $T3$ is 0.

Case 2: For distributed target, $T3$ is 4/9.

Case 3: For partial targets, $T3$ is in between 0 to 4/9.

To make the same extreme value as of entropy, we modify the formula for $T3$ as

$$T3 = \frac{9}{8}\left(1 - \left(\sum_{i=1}^{n} P_i^3\right)\right), \tag{3.15}$$

where P_i's are the pseudo-probabilities; defined in Equation (3.4). The comparison graph of $T3$ with entropy and the Wishart-$T3/A/\alpha$ classification map are shown in Figure 3.11. It can be observed that, the scatter plot in Figure 3.11(a) moves downward in comparison to the Gini-entropy scatter plot in Figure 3.6. Therefore now, a large part of the scatter plot of $T3$-entropy is lying below the diagonal line. Hence most of the pixels have lower entropy value than $T3$. That means as value of q increases from 2 to 3, the pixels start moving towards higher entropy values. Thereby, the classification result deteriorates as can be seen in Figure 3.11(b). As we further increase the value of q, the scatter plot moves more downward and the result further deteriorates. Therefore Tsallis entropy with $q = 2$ (minimum), which is the same as Gini-index, is the best performing index among all the Tsallis entropies. This validates the concept that classification accuracy increases if the pixels move towards the lower entropy region. Now, we can speculate that if the scatter plot moves upward, then classification accuracy will increase.

3.3.2.2 Rényi entropies based landcover classification schemes

Here we made a comparison of different Rényi entropies based landcover classification schemes. As shown in Equation 3.12, Rényi entropy is a function of variable β. As β tends to 1, Rényi entropy becomes Shannon entropy. At first, a landcover classification based on Rényi entropy with $\beta = 2$ ($R2$) is developed.

The values of $R2$ for various scatterer types are as follows.

Case 1: For pure target, $R2$ is 0.

Case 2: For distributed target, $R2$ is $\log_2 3$.

Case 3: For partial targets, $R2$ is in between 0 to $\log_2 3$.

To make the same extreme value as of entropy, we modify the formula for R2 as

$$R2 = \frac{1}{\log_2 3} \log_2 \left(\sum_{i=1}^{n} P_i^2 \right). \tag{3.16}$$

The comparison graph of $R2$ with entropy and the Wishart-$R2/A/\alpha$ classification map are shown in Figure 3.12. From Figure 3.12(a), it can be observed that the scatter plot moves upward in comparison to the Gini-entropy scatter plot in Figure 3.6 and therefore now, most of the pixels have Gini value smaller than entropy value. This means that the pixels move towards lower entropy value in entropy/alpha plane, if entropy is replaced by $R2$. As expected, the performance of $R2$ based classification scheme is better than entropy and Gini based classification scheme.

Next the value of β increases to three. A landcover classification scheme based on Rényi entropy with $\beta = 3$ ($R3$) is developed. The values of $R3$ for various scatterer types are as follows.

Case 1: For pure target, $R3$ is 0.

Case 2: For distributed target, $R3$ is $(\log_2 9)/2$.

Case 3: For partial targets, $R3$ is in between 0 to $(\log_2 9)/2$.

To make the same extreme value as of entropy, we modify the formula for $R3$ as

$$R3 = \frac{1}{\log_2 9} \log_2 \left(\sum_{i=1}^{n} P_i^3 \right). \tag{3.17}$$

The scatter plot for $R3$ and Wishart-$R3/A/\alpha$ classification map are shown in Figure 3.13. From Figure 3.13(a), it is observed that the scatter plot moves further upward and therefore push pixels more towards the lower entropy value. Thereby the classification accuracy has been further enhanced as shown in Figure 3.13(b). Therefore it is expected that as we will go on increasing the value of β, the scatter plot will move more upward and the results will go on improving.

Next the value of β increases to 4. A complete landcover classification scheme for Rényi with $\beta = 4$ ($R4$) is realized. The values of $R4$ for various scatterer types are as follows.

Case 1: For pure target, $R4$ is 0.

Case 2: For distributed target, $R4$ is $(\log_2 27)/3$.

Case 3: For partial targets, $R4$ is in between 0 to $(\log_2 27)/3$.

To make the same extreme value as of entropy, we modify the formula for $R4$ as

$$R4 = \frac{1}{\log_2 27} \log_2 \left(\sum_{i=1}^{n} P_i^4 \right). \tag{3.18}$$

The corresponding scatter plot for $R4$ and Wishart-$R4/A/\alpha$ classification map are shown in Figure 3.14. From the Figure 3.14(a), it can be observed that the scatter plot further moves upward. However, as shown in Figure 3.14(b), the classification result deteriorates. This nullifies our assumption that as we will go on stretching the scatter plot upward, the classification results goes on improving. The reason behind this is that as the scatter plot moves upward, simultaneously entropy/alpha space gets narrower. The various entropies/alpha spaces are shown in Figure 3.15. From this figure, it can be seen that as one moves from entropy→ Gini ($T2$)→ $R2 \rightarrow R3 \rightarrow R4$, the corresponding entropy/alpha space gets narrower. This means that the choice of alpha that denotes the dominant scattering mechanism for a particular value of entropy gets reduced. This reduces the discrimination capability of the entropy based classification algorithm. Therefore the optimum choice for the variable β is 3. Hence, we conclude that Rényi entropy, with $\beta = 3$, based classification scheme provides the best result among all the Rényi entropies.

3.3.2.3 Comparison of different entropies based landcover classification schemes

A comparison among different types of entropy based classification is carried out based on the performance of each in crop type classification. Percentage of different classes correctly classified by different entropies based Wishart classifiers are shown in Table 3.3. From this performance table, following observations are noted as follows.

- Rényi with $\beta = 3$ is the best performing index among all types of entropy.

- The classification efficiency goes on increasing as one moves from entropy → $T3$ → Gini ($T2$) → $R4$ → $R2$ → $R3$.
- Only classification schemes based on Rényi with $\beta = 2$ and $\beta = 3$ are able to classify all types of crops correctly.
- Generally, classification schemes based on Rényi entropy is performing better than Tsallis entropy based classification scheme.

Table 3.3: Percentage of different classes correctly classified by different entropies based Wishart classifiers.

	Tsallis3	Entropy	Tsallis2	Rényi2	Rényi3	Rényi4
Lucerne	63.65	44.56	86.67	89.34	79.22	×
Beet	66.03	75.08	59.05	30.80	80.06	67.74
Potato	88.75	77.30	92.17	89.29	66.22	77.7
Pea	82.70	78.43	80.49	80.58	76.48	94.67
Bare soil	×	×	×	98.81	97.89	99.64
Barley	×	×	×	84.76	87.97	×
Wheat	×	×	×	82.22	82.85	44.04
Rape seed	×	×	×	53.32	74.37	32.81

3.4 A Fully automated landcover classification scheme

In the entropy/alpha classification technique, the entropy/alpha plane is sub-divided into nine basic classes of different scattering mechanisms. The location of the boundaries within the feasible H/α space is set based on the general properties of the scattering behaviors and is independent of any particular dataset. However, there is some degree of arbitrariness over the location of entropy and alpha boundaries that offers a sensible segmentation of PolSAR images [36]. Also, the fixed linear decision boundaries in the H/α plane greatly affects the classification results. A cluster may fall on a boundary or may not be confined in a single zone. In addition, it may be possible that a group of clusters may be enclosed in the same zone. The Wishart-H/α technique provides a reasonable image segmentation by moving the cluster-centroids. However, its performance highly depends on the initial input clusters.

If the initial input clusters are not properly chosen, then the Wishart based classification algorithm either requires more number of iteration to converge or may not converge at all. Particularly it does not perform adequately when the clusters are not confined to a single zone. As an example, for Flevoland dataset, the clusters are not confined to a single zone as shown in Figure 3.16. As a result, the corresponding Wishart-$H/A/\alpha$ classification scheme does not perform satisfactorily as can be observed in Figure 3.10(a).

This led us to investigate the location of boundaries that facilitate the Wishart based classifiers to perform better. We propose a fully automated landcover classification using Wishart-$H/A/\alpha$ technique. Here, the boundaries in entropy/alpha plane is decided based on the nature of a particular dataset. At first, the entropy boundary is decided by using Gaussian mixture models (GMM). GMM has been one of the popular data clustering methods where each cluster is assumed to be Gaussian distributed. Expectation Maximization (EM) algorithm is used to obtain maximum likelihood estimation of the parameters in a Gaussian mixture model. Here, we have considered that GMM consists of three components. The reason behind choosing three components is that only two boundaries are needed. However, if probability of any component in the complete distribution is very small then we go for GMM with four components and neglect the component with less weight attached to it. Here, the cluster boundary is considered as the entropy/alpha boundary. Gaussian mixture distribution for the entropy of PolSAR images for the Flevoland site is shown in Figure 3.17. As shown in this figure, the entropy boundaries estimated are 0.56 and 0.78. Based on these boundaries, the pixels are divided into three regions of entropy. Next, alpha boundaries for three entropy regions can be estimated using the same procedure.

3.4.1 Results

The new and old entropy/alpha boundaries' values for Flevoland and San Francisco datasets are tabulated in Tables 3.4 and 3.5, respectively. First, for Flevoland dataset, we obtained the H/α classification maps for the old and new boundary set as shown in Figures 3.18(a) and 3.18(b), respectively. On comparison of both the figures, it is observed that the H/α classification map with new boundary set has the following merits:

- It is more informative.
- The rectangular patches of agricultural land are more clearly visible.
- The pixels are classified into more clusters (classes), thereby increases the discrimination capability of the H/α classification technique.

Table 3.4: The change in boundaries for Flevoland data.

Parameters	Old boundaries	New boundaries
Entropy	0.5 & 0.9	0.56 & 0.78
Alpha1	42 & 48	20.8 & 41.1
Alpha2	40 & 50	28.5 & 44
Alpha3	55	43

Table 3.5: The change in boundaries for San Francisco data.

Parameters	Old boundaries	New boundaries
Entropy	0.5 & 0.9	0.26 & 0.63
Alpha1	42 & 48	14.5 & 41.1
Alpha2	40 & 50	26.64 & 44.8
Alpha3	55	48

These observations thus validate that boundaries should not be same for all the cases. Rather, it should be specific to the nature of a particular dataset. As it is expected that this approach will increase the efficacy of Wishart based classifier, we obtained Wishart-$H/A/\alpha$ result for the old and new boundary sets; as shown in Figures 3.19(a) and 3.19(b), respectively. To do the performance evaluation, these results are compared with the ground truth, which is shown in Figure 3.10(d). Percentage of different crops correctly classified by entropy based Wishart classifier with old and new boundary sets are shown in Table 3.6. From this table, following observations are made.

- Wishart-$H/A/\alpha$ with the new boundary is performing better than its counterpart.
- All crops are correctly segmented in new boundary case.
- The overall classification accuracy of crops correctly classified by new boundary scheme is higher than the old boundary scheme.

Also with new entropy/alpha boundary set, the iterative Wishart based supervised classifier takes fewer numbers of iterations to converge. This saves a lot of computational cost. As in each iteration, 76800 number of pixels in Flevoland image are reclassified by the Wishart based iterative algorithm, which requires a finite amount of time.

Similarly for San Francisco data, the Wishart-$H/A/\alpha$ results for old and new boundaries sets are shown in Figure 3.20. Here, we compared both the results after two iterations. Upon comparison, it is observed that the details are more clearly classified in new boundary case. For example, polo field and golf course are become more clearly visible.

Table 3.6: Percentage of different classes correctly classified by Wishart-$H/A/\alpha$ methods with new and old boundary sets.

Class type	Old boundary	New boundary
Potato	53.74	72.65
Lucerne	43.93	84.66
Pea	93.18	92.89
Beet	79.90	78.26
Bare Soil	×	88.14
Barley	×	76.7
Rape seed	×	54.52
Wheat	×	69

3.5 Summary

In this chapter, we have proposed three new landcover classification algorithms. These three classification algorithms have been developed and validated. First, a new Gini-index based land cover classification technique was proposed. Using this algorithm, enhanced crop classification accuracy has been reported. This proposed Gini-index based classification scheme is also computationally more efficient than the classic entropy based classification scheme. Secondly, landcover classification schemes based on various types of entropies were developed for the segmentation of PolSAR images and was being compared as per their discriminating abilities. The optimum one that correctly classifies all types of crops with good classification efficiency has been reported. In the third, we have proposed a fully automated landcover classification using Wishart-$H/A/\alpha$ technique. Here, the boundaries in entropy/alpha plane were decided based on the particular dataset. It was shown that the crop classification capability and computational efficiency of Wishart-$H/A/\alpha$ scheme are enhanced by following this approach. All crops were observed to be correctly segmented with good classification accuracy by this approach.

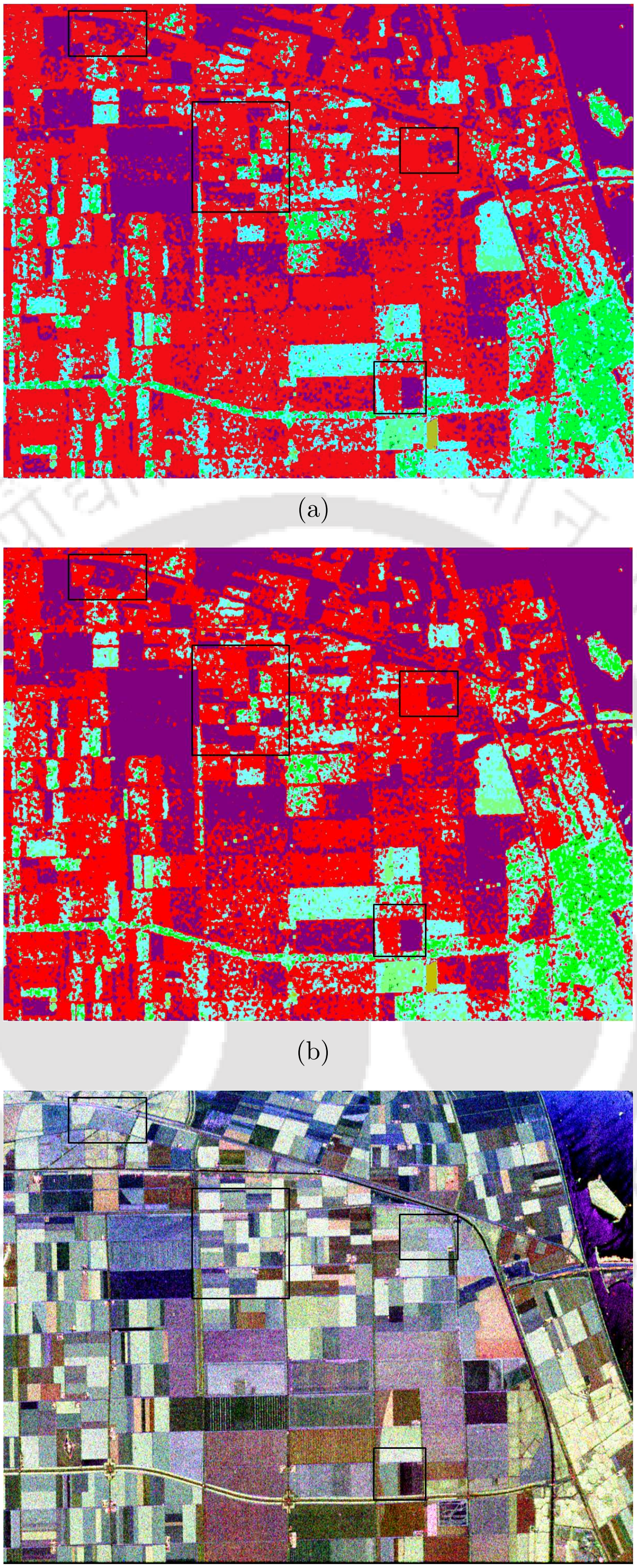
(a)

(b)

(c)

Figure 3.7: Comparison of G/α and H/α Classification map. From top: (a) H/α Classification map, (b) G/α Classification map, and (c) Pauli RGB image. The four outlined areas demark (from left to right) region #1, #2, #3, and #4, respectively.

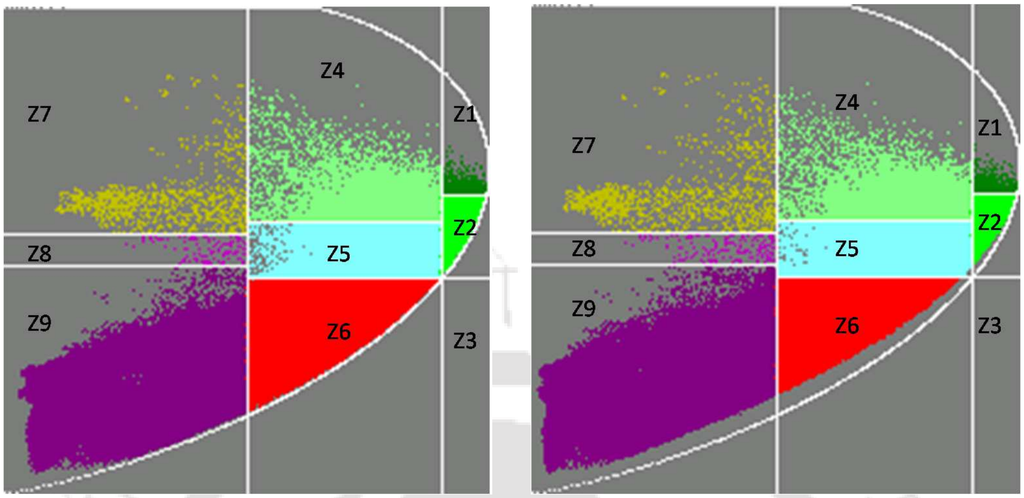

(a) (b)

Figure 3.8: The distribution of pixels for Flevoland data in (a) H/α and (b) G/α segmented plane. No. of pixels in each zone of the H/α segmented plane is Z9=163042, Z8=137, Z7=1168, Z6=423691, Z5=121120, Z4=16321, Z3=0, Z2=41635, Z1=886.

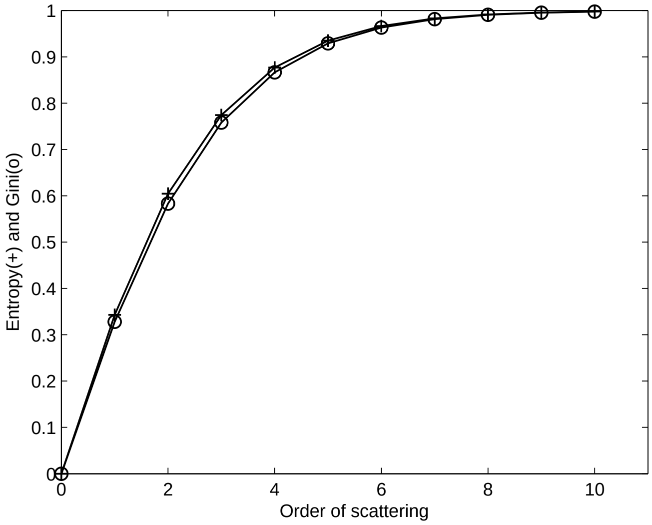

Figure 3.9: Variation of entropy and Gini-index as a function of scattering order in volume backscatter.

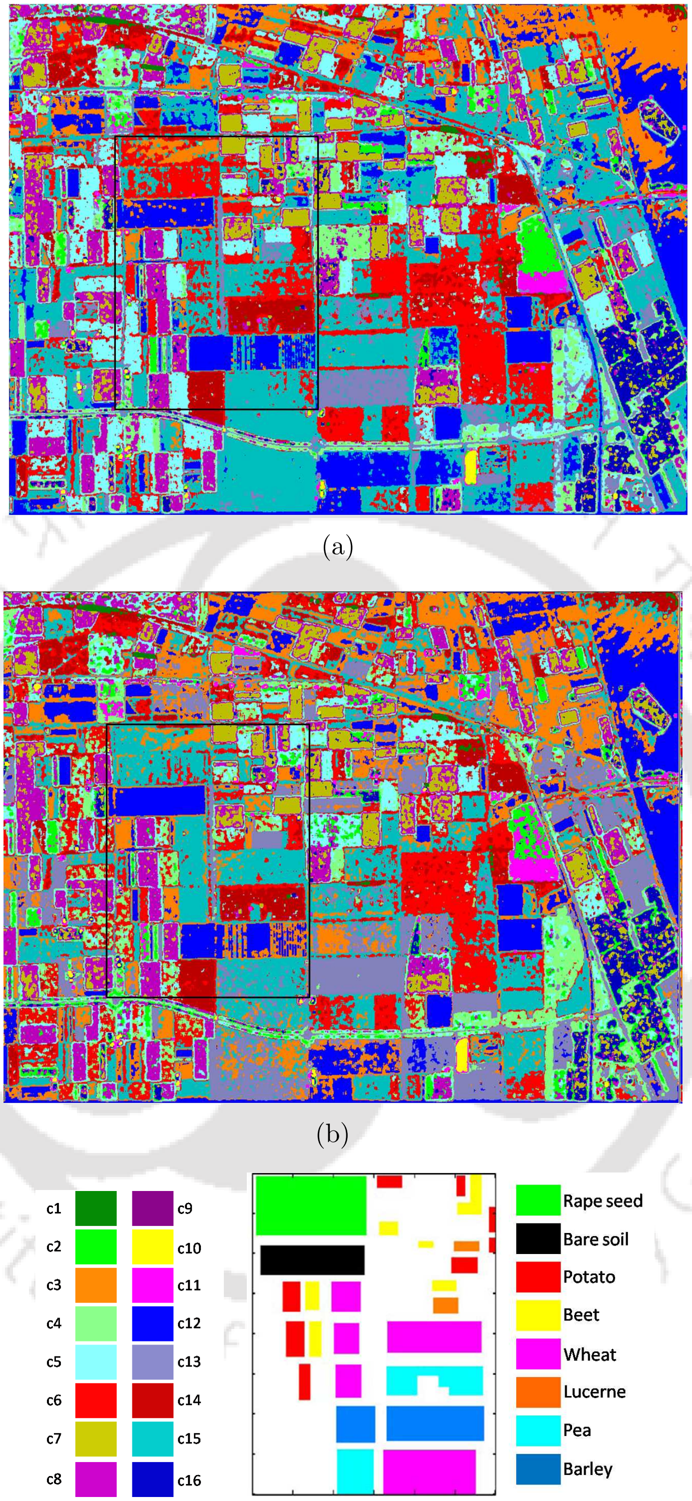

Figure 3.10: The performance evaluation of Wishart-$G/A/\alpha$ and Wishart-$H/A/\alpha$ w.r.t. the ground truth. From top: (a) Wishart-$H/A/\alpha$ Classification after 10 iterations, (b)Wishart- $G/A/\alpha$ Classification after 10 iterations, (c) Colour code for the 16 classes, and (d) Ground truth map.

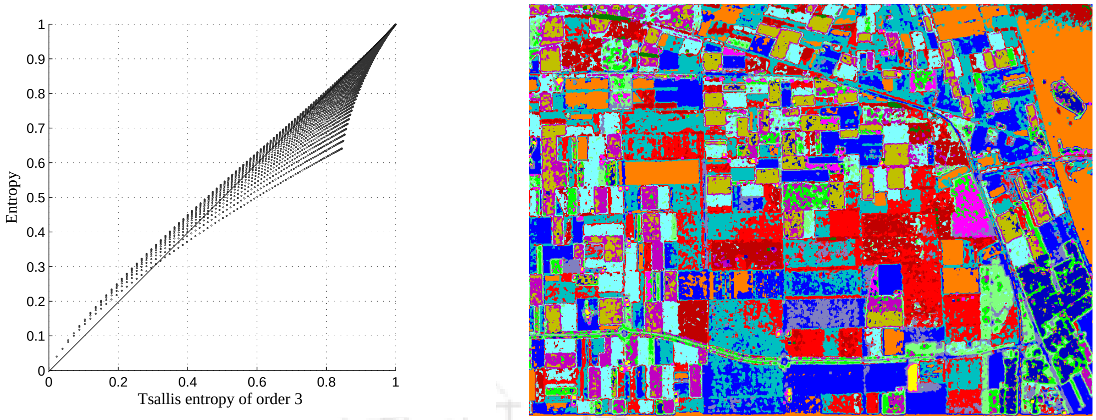

(a) (b)

Figure 3.11: (a) Pixels distribution in the Entropy/Tsallis3 space and (b) Wishart-$T3/A/\alpha$.

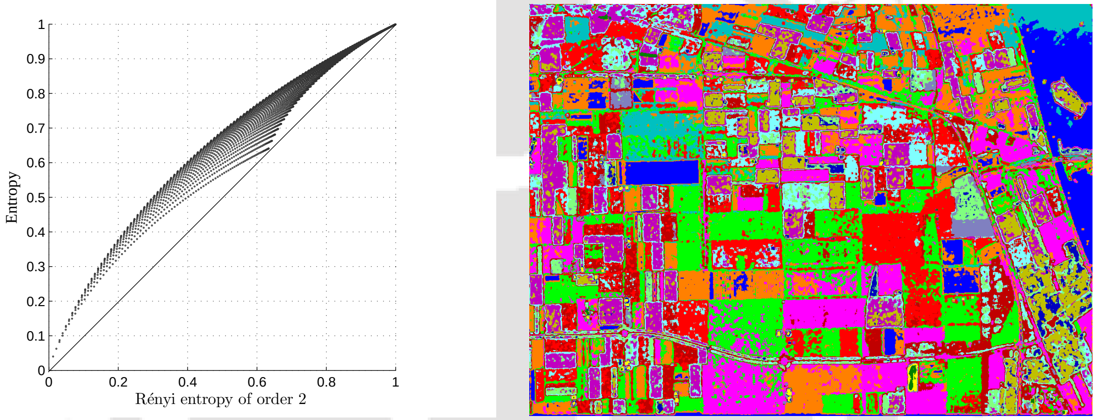

(a) (b)

Figure 3.12: (a) Pixels distribution in the Entropy/Rényi2 space and (b) Wishart-$R2/A/\alpha$.

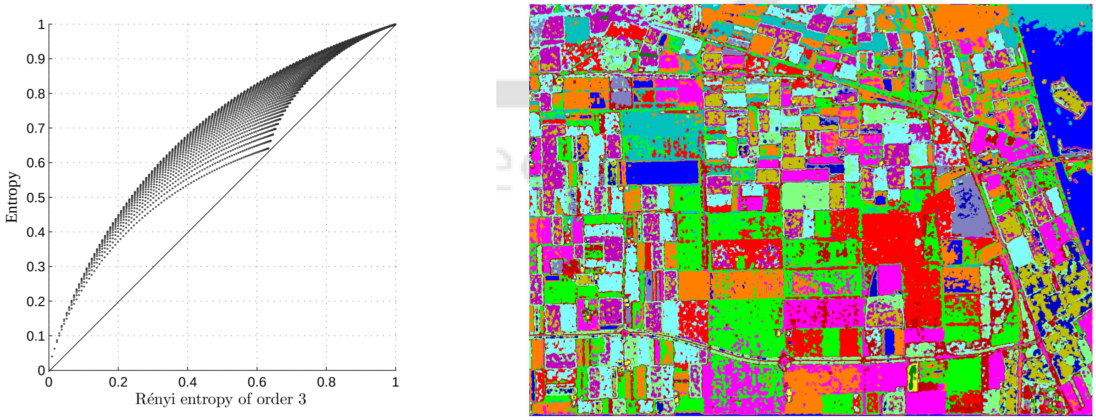

(a) (b)

Figure 3.13: (a) Pixels distribution in the Entropy/Rényi3 space and (b) Wishart-$R3/A/\alpha$.

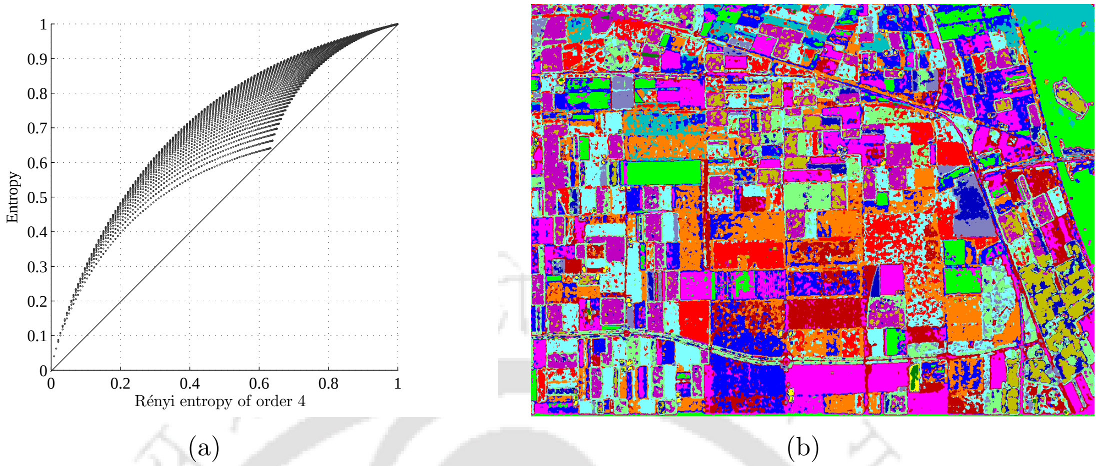

Figure 3.14: (a) Pixels distribution in the Entropy/Rényi4 space and (b) Wishart-$R4/A/\alpha$.

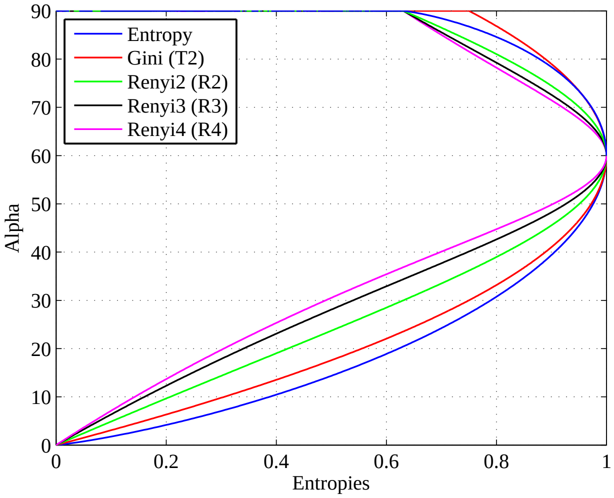

Figure 3.15: Feasible region for various entropies/alpha plane.

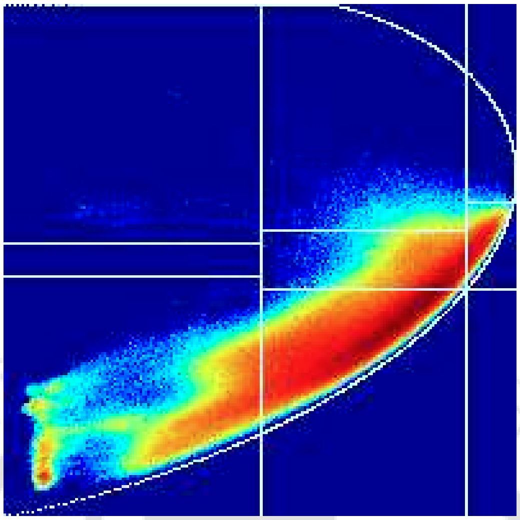

Figure 3.16: H/α occurrence plane: Flevoland data.

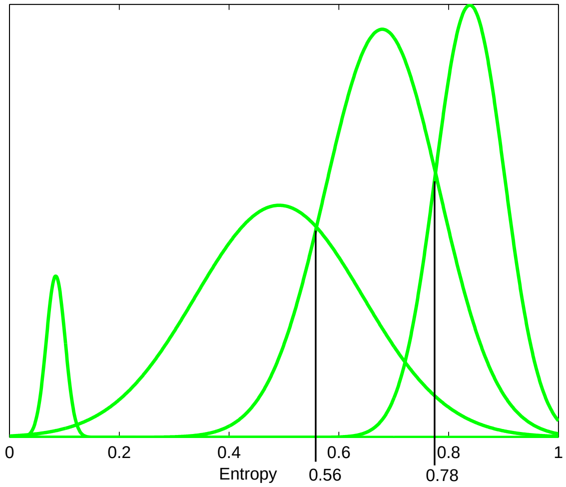

Figure 3.17: Gaussian mixture distribution for the entropy of PolSAR images for the Flevoland data.

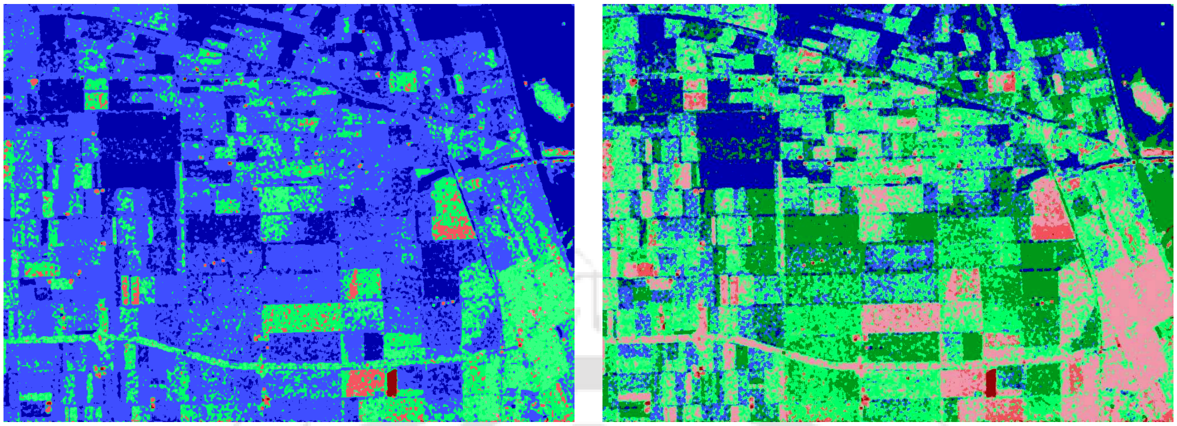
(a) (b)

Figure 3.18: *H/alpha* classification map with (a) old boundary and (b) new boundary.

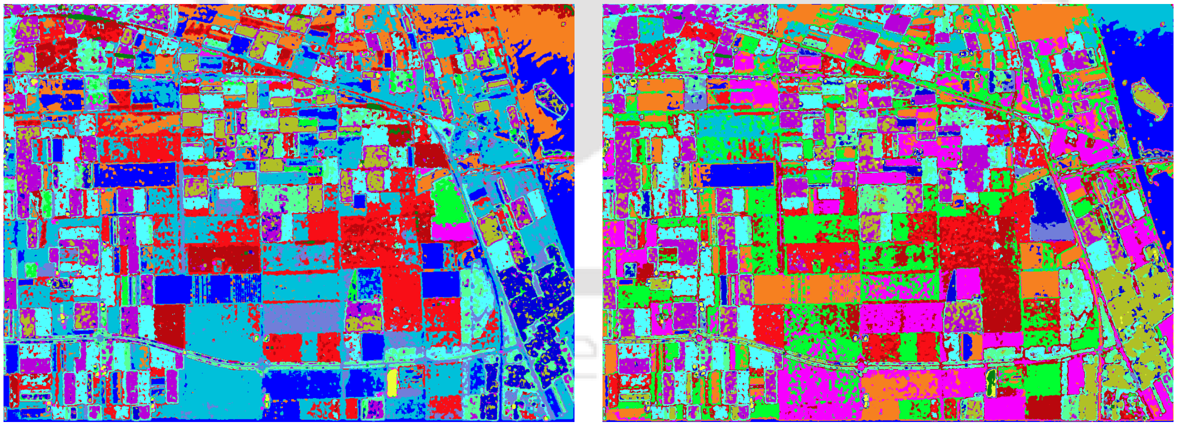
(a) (b)

Figure 3.19: Wishart-$H/A/\alpha$ classification map for Flevoland data with (a)old boundary: converged after 6 iterations and (b) new boundary: converged after 3 iterations.

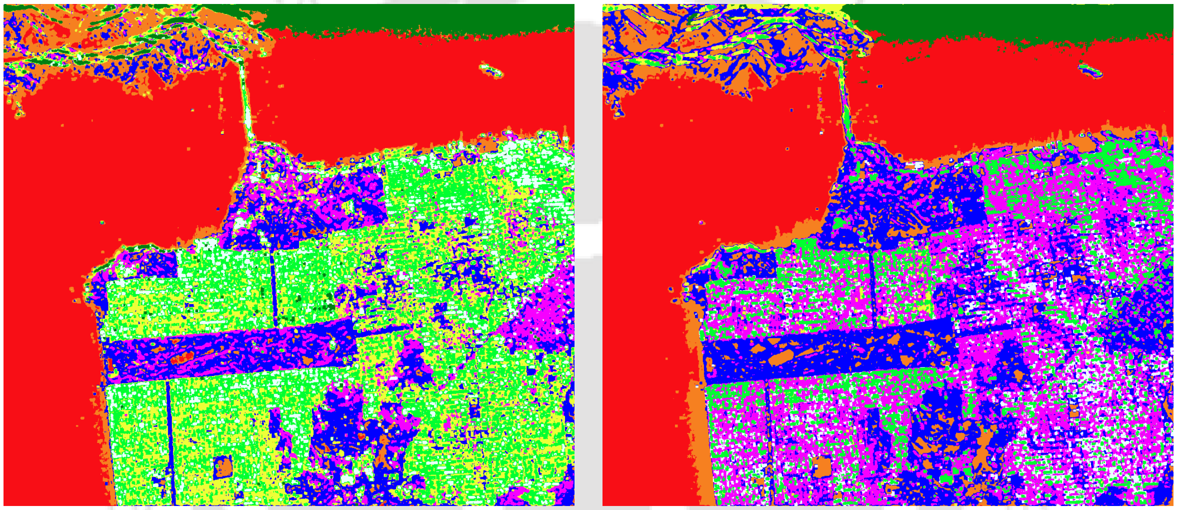

(a) (b)

Figure 3.20: Wishart-$H/A/\alpha$ classification map for San Francisco data after two iterations: (a) old boundary and (b) new boundary.

4

Analysis of Hybrid-PolSAR Images

Contents

Recently there has been a growing interest in dual-polarimetric (dual-Pol) systems, especially in hybrid-Pol mode. A hybrid-Pol system transmits circular polarization and receives two mutually orthogonal coherent linear polarizations. This configuration is the optimum choice when there is a requirement for wider swath coverage with constraint of limited average transmitted power and bandwidth. However, like any other dual-Pol systems, the hybrid-Pol system occupies only half of the polarization information-space provided by fully polarimetric SAR (quad-Pol) system. Therefore, at first, a comparison of information provided by hybrid-Pol with quad-Pol configuration is carried out. The comparison results show that the information content in hybrid-Pol data is less but comparable with that of a quad-Pol data. Secondly, as far as the analysis of hybrid-Pol data is concerned, there have been quite a few approaches reported in the open literature as can be observed in Section 2.3. These studies have demonstrated the rich potential of hybrid-Pol system for further quantitative analysis. This gives us the motivation to analyze hybrid-Pol data to extract information from its images. We propose three different approaches for the analysis of hybrid-Pol data. These analysis demonstrated that a meaningful information can be extracted from the hybrid-Pol images.

The rest of the chapter is organized as follows. In the next section, we provide a comparison of the information provided by hybrid-Pol and quad-Pol SAR data. In Section 4.2, we discuss about the proposed techniques for the analysis of hybrid-Pol data. Section 4.3 gives summary of the work presented in this chapter.

4.1 Comparison of hybrid-Pol with quad-Pol

In this section, a comparison of the information provided by hybrid-Pol and quad-Pol SAR data based on two approaches is carried out. In the first approach, the information content of hybrid-Pol with quad-Pol is compared by using compact scattering models [38]. In the second approach, comparison among both the configurations is carried out on the basis of information about the scattering processes.

4.1.1 Using compact polarimetry scattering model

Compact polarimetry scattering model is a technique that allows construction of pseudo quad-Pol data from dual-Pol SAR data [38]. Here, we discuss the technique of generating pseudo quad-Pol data from hybrid-Pol data. At first, the hybrid-Pol data is derived from the quad-Pol data. Then the pseudo quad-Pol data is constructed from the derived hybrid-Pol data. This method is explained in details below.

The scattering matrix for the quad-Pol configuration, in linear (H,V) basis, is given by

$$\mathbf{S} = \begin{bmatrix} S_{HH} & S_{HV} \\ S_{VH} & S_{VV} \end{bmatrix}, \tag{4.1}$$

where the first and second subscripts denote received and transmitted wave polarizations, respectively. In monostatic backscattering case, reciprocity constrains the Sinclair scattering matrix to be symmetrical, i.e. $S_{HV} = S_{VH}$. The scattering information can also be represented in terms of target vector as shown in Section 1.2.2.2. The lexicographic target vector $\underline{\Omega}$ for monostatic backscattering case is shown in Equation (1.19). The related 3×3 backscattered covariance matrix can be generated as shown in Equation (1.24). The expression for the generated covariance matrix is given by

$$\mathbf{C} = \left\langle \begin{bmatrix} |S_{HH}|^2 & \sqrt{2}S_{HH}S_{HV}^* & S_{HH}S_{VV}^* \\ \sqrt{2}S_{HV}S_{HH}^* & 2|S_{HV}|^2 & \sqrt{2}S_{HV}S_{VV}^* \\ S_{VV}S_{HH}^* & \sqrt{2}S_{VV}S_{HV}^* & |S_{VV}|^2 \end{bmatrix} \right\rangle. \tag{4.2}$$

From the quad-Pol data, the hybrid-Pol data is generated as follows. The lexicographic target vector for the hybrid-Pol system that transmits a right hand circular polarization (RHCP) wave is given by

$$\underline{\Omega} = \frac{1}{\sqrt{2}} \begin{bmatrix} S_{HH} - iS_{HV} & -iS_{VV} + S_{HV} \end{bmatrix}^T. \tag{4.3}$$

The related 2×2 covariance matrix for hybrid-Pol is then given by

$$\begin{aligned}\mathbf{C}_{Hyb} = 1/2 &\begin{bmatrix} |S_{HH}|^2 & iS_{HH}S_{VV}^* \\ -iS_{VV}S_{HH}^* & |S_{VV}|^2 \end{bmatrix} \\ +1/2 &\begin{bmatrix} |S_{HV}|^2 & -i|S_{HV}|^2 \\ i|S_{HV}|^2 & |S_{HV}|^2 \end{bmatrix} \\ +1/2 &\begin{bmatrix} -2\Im(S_{HH}S_{HV}^*) & S_{HH}S_{HV}^* + S_{VV}^*S_{HV} \\ S_{HH}^*S_{HV} + S_{VV}S_{HV}^* & 2\Im(S_{VV}S_{HV}^*) \end{bmatrix}\end{aligned} \quad . \tag{4.4}$$

The individual terms of $\mathbf{C}_{Hyb}$ can be obtained from quad-Pol covariance matrix $\mathbf{C}$. Thus the hybrid-Pol data can be generated from the quad-Pol data. To compare the information content of both the modes, we generate the pseudo quad-Pol data from the hybrid-Pol data by using compact polarimetry scattering models [38]. These scattering models assume that polarimetric scattering is reflection symmetric. The assumption of reflection symmetry implies that, the cross-polar scattering coefficients will be uncorrelated with the co-polar coefficients, i.e.

$$\langle S_{HH}S_{HV}^* \rangle = \langle S_{VV}S_{HV}^* \rangle = 0. \tag{4.5}$$

This assumption is valid for most of the natural surfaces at practical frequencies [38]. Under this assumption the quad-Pol covariance matrix becomes a function of five independent parameters.

$$\mathbf{C} = \left\langle \begin{bmatrix} |S_{HH}|^2 & 0 & S_{HH}S_{VV}^* \\ 0 & 2|S_{HV}|^2 & 0 \\ S_{VV}S_{HH}^* & 0 & |S_{VV}|^2 \end{bmatrix} \right\rangle \tag{4.6}$$

However, the 2×2 hybrid-Pol covariance matrix measures only four independent parameters. Therefore, an additional constrain is required to reconstruct the pseudo quad-Pol data from the hybrid-Pol data. A relationship between the magnitudes of the linear coherence and the cross-polarization ratio may be used as a another constrain [38], i.e.

$$\frac{\langle |S_{HV}|^2 \rangle}{\langle |S_{HH}|^2 \rangle + \langle |S_{VV}|^2 \rangle} = \frac{1-|\rho|}{4}, where$$
$$\rho \equiv \frac{\langle S_{HH} S_{VV}^* \rangle}{\sqrt{\langle |S_{HH}|^2 \rangle * \langle |S_{VV}|^2 \rangle}}. \tag{4.7}$$

These two equation are iteratively solved for $|S_{HV}|^2$. The iteration process starts with an initial value of $|S_{HV}|^2$ as:

$$|S_{HV}|^2 = \frac{C_{11}+C_{22}}{2} \times \frac{1-|\rho_0|}{3-|\rho_0|},$$

where

$$\rho_0 = \frac{iC_{12}}{\sqrt{C_{11}C_{22}}}. \tag{4.8}$$

Then the following equations are solved iteratively until convergence.

$$\rho_{n+1} = \frac{iC_{12} + (|S_{HV}|^2)_{(n)}}{\sqrt{(C_{11} - (|S_{HV}|^2)_{(n)})(C_{22} - (|S_{HV}|^2)_{(n)})}}$$
$$(|S_{HV}|^2)_{(n+1)} = \frac{C_{11}+C_{22}}{2} \times \frac{1-|\rho_{n+1}|}{3-|\rho_{n+1}|} \tag{4.9}$$

The variable C_{xy} corresponds to the elements of the hybrid-Pol covariance matrix. The assumption of reflection symmetry reduces this hybrid-Pol covariance matrix to:

$$[\mathbf{C}_{Hyb}] = \begin{bmatrix} C_{11} & C_{12} \\ C_{12} & C_{22} \end{bmatrix}$$
$$= 1/2 \begin{bmatrix} |S_{HH}|^2 & iS_{HH}S_{VV}^* \\ -iS_{VV}S_{HH}^* & |S_{VV}|^2 \end{bmatrix}. \tag{4.10}$$
$$+1/2 \begin{bmatrix} |S_{HV}|^2 & -i|S_{HV}|^2 \\ i|S_{HV}|^2 & |S_{HV}|^2 \end{bmatrix}$$

As the components of the hybrid-Pol covariance matrix are known to us, so the estimated value of $|S_{HV}|^2$ yields values for $|S_{HH}|^2$, $|S_{VV}|^2$ and $S_{HH}S_{VV}^*$.

The pseudo quad-Pol covariance matrix $\mathbf{C}_{pseudo}$ is then constructed as

$$\mathbf{C}_{pseudo} = \left\langle \begin{bmatrix} C_{11} - |S_{HV}|^2 & 0 & -iC_{12} + |S_{HV}|^2 \\ 0 & 2|S_{HV}|^2 & 0 \\ iC_{12} + |S_{HV}|^2 & 0 & C_{22} - |S_{HV}|^2 \end{bmatrix} \right\rangle . \tag{4.11}$$

4.1.1.1 Results and discussions

To compare the performance of hybrid-Pol with quad-Pol system, we used NASA/JPL AIRSAR L band quad-Pol data for Flevoland region. A sub-region from the full image, as shown in Figure 4.1(a), is considered here. This area consists of various crops such as wheat, potato, pea, beet, and lucerne. The assumption of reflection symmetry is valid here, as crops on horizontal surfaces do not induce polarization orientation angle shifts. At first, the hybrid-Pol data is derived from the quad-Pol data. Then the pseudo quad-Pol data is constructed from the derived hybrid-Pol data by using compact scattering model.

Figures 4.1(b)-4.1(d) show the comparison of reconstructed pseudo quad-Pol data with the original quad-Pol data set. In all the figures, the abscissa contains the original values and the ordinate contains the reconstructed values. It can be observed from these figures that the pseudo quad-Pol values of $|HH|$,$|VV|$ and $|HV|$ match with the corresponding original quad-Pol values. $|HV|$ matching is relatively poorer as it is always $7-10dB$ below $|HH|$ and $|VV|$. From this observation, it can be inferred that information content in hybrid-Pol images is almost same to that of a quad-Pol.

4.1.2 Based on scattering information

A further comparison between both the configurations based on information about the scattering process is carried out here. The scattering contribution of each of the three basic scattering mechanisms can be estimated by using Freeman and Durden decomposition technique [29]. Freeman and Durden proposed a three-component scattering model for polarimetric data which has been discussed in Section 2.1.3. One basic assumption of this three-component scattering model is reflection symmetry, i.e. the same assumption as of compact scattering model. So, there will not be any further loss of information when we

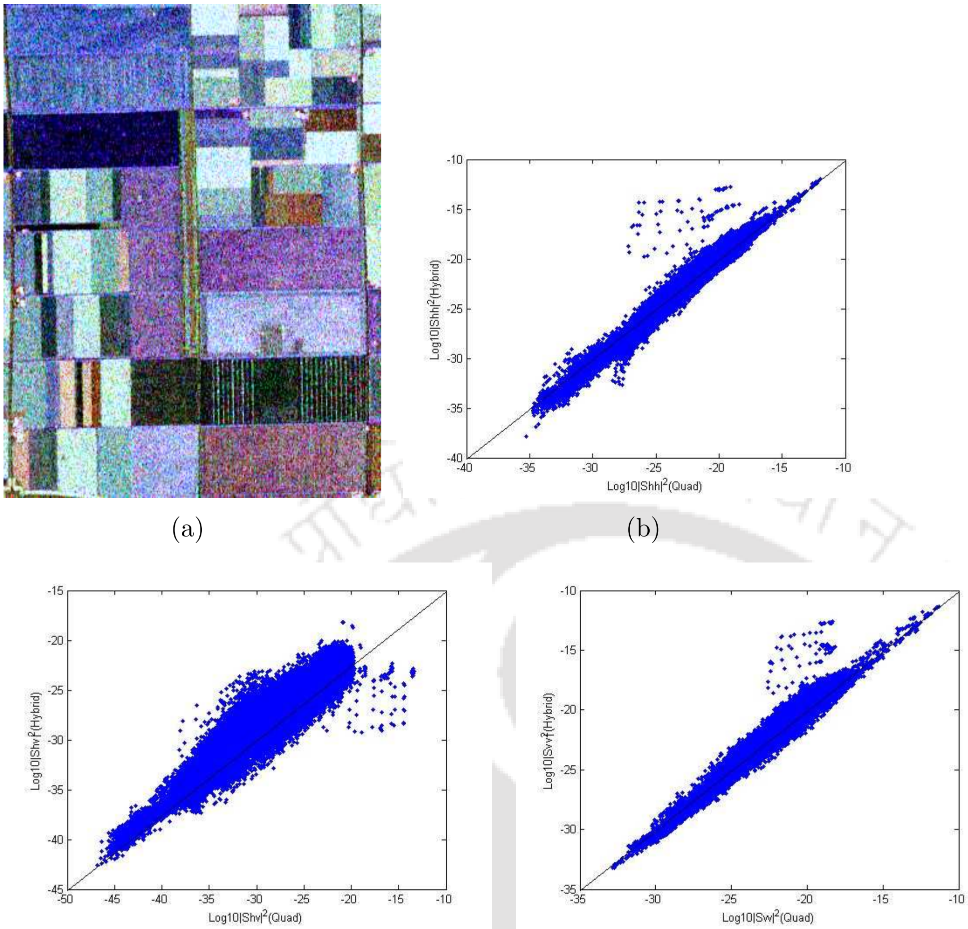

(a) (b)

(c) (d)

Figure 4.1: Hybrid-Pol mode reconstructed data. (a) Pauli basis image showing subarea of AIRSAR Flevoland data used in this paper, (b) $\log_{10}|S_{HH}|^2$, (c) $\log_{10}|S_{HV}|^2$, (d) $\log_{10}|S_{VV}|^2$.

employ this decomposition techniques on pseudo quad-Pol data.

4.1.2.1 Results and discussions

Again the same subarea of Flevoland region as shown in Figure 4.1(a) has been considered here for the demonstration. First, the pseudo quad-Pol data is generated from hybrid-Pol data as described in Section 4.1.1. Then by applying Freeman and Durden decomposition technique, the scattering contribution of each of the three basic scattering mechanisms for both quad-Pol and pseudo quad-Pol data are evaluated.

The contribution of surface scattering mechanism for both the data are represented in Figures 4.2(a) and 4.2(b), respectively. Similarly for double bounce and volume scattering, refer Figures 4.3 and 4.4, respectively. On comparison, one can observe that there are differences between both the configurations in scattering information content. The comparison of contributions of each scattering mechanism, viz. single bounce, double bounce and volume scattering, of hybrid-Pol and quad-Pol are shown in Figures 4.2(c), 4.3(c) and 4.4(c), respectively. In these figures, the abscissa represents the original quad-Pol values and the ordinate represents the pseudo quad-Pol values. The comparative graphs show that there are some differences among both the configurations for single bounce and double bounce scattering cases, but they are almost the same for the volume scattering case. Figure 4.5 presents the colour-coded image with P_d as red, P_v as green and P_s as blue for both quad-Pol and pseudo quad-Pol data. On visual inspection of both the RGB image, it is observed that the scattering information content in case of hybrid-Pol configuration is less but comparable with that of a quad-Pol configuration.

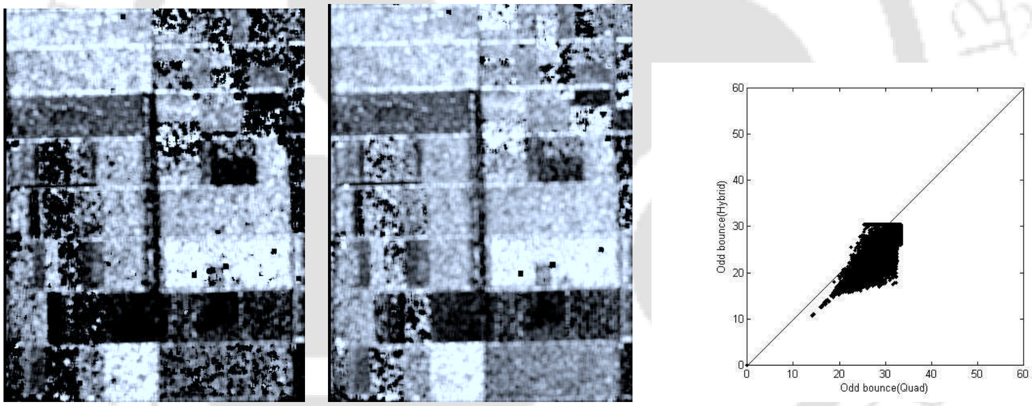

(a) (b) (c)

Figure 4.2: Contribution from single bounce scattering mechanism estimated after Freeman-Durden decomposition of (a) hybrid-Pol and (b) quad-Pol, and (c) shows the comparison between single bounce scattering contribution of both the configurations.

4.2 Analysis of hybrid-PolSAR images

It has been realized that the amount of scattering information in case of hybrid-Pol is less but contains enough information about the target scene that may be extracted and used. This leads us to analyze the hybrid-Pol data to extract meaningful information from its

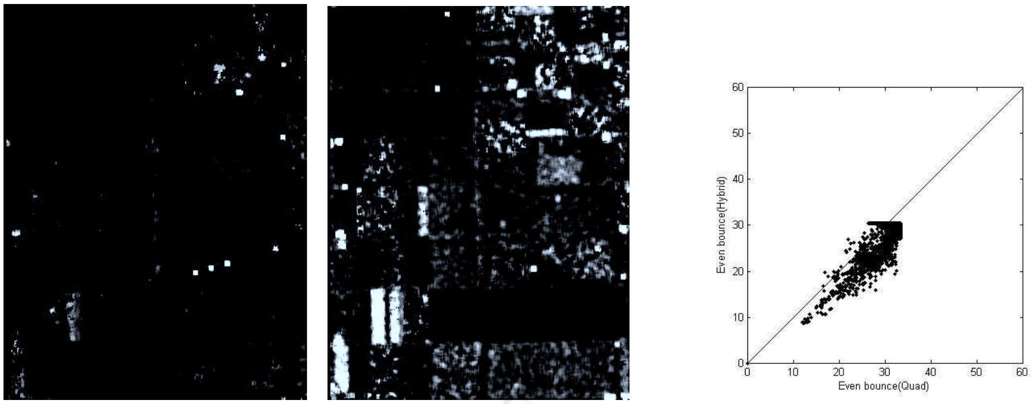

(a) (b) (c)

Figure 4.3: Contribution from double bounce scattering mechanism estimated after Freeman-Durden decomposition of (a) hybrid-Pol and (b) quad-Pol, and (c) shows the comparison between double bounce scattering contribution of both the configurations.

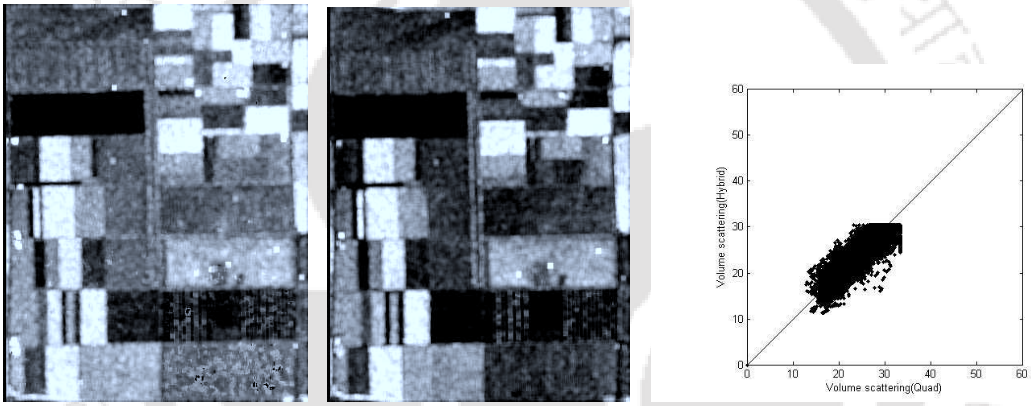

(a) (b) (c)

Figure 4.4: Contribution from volume scattering mechanism estimated after Freeman-Durden decomposition of (a) hybrid-Pol and (b) quad-Pol, and (c) shows the comparison between volume scattering contribution of both the configurations.

images. The analysis of hybrid-Pol may start with the knowledge of stokes vector of the received signal as shown in Section 2.3.

The Stokes vector that corresponds to a hybrid-Pol can be generated from the available fully polarimetric SAR dataset. The procedure of obtaining the hybrid-Pol data from quad-Pol is as follows.

- Step 1: The backscattered electric field $\underline{E}_B$ is related to the transmitted right hand

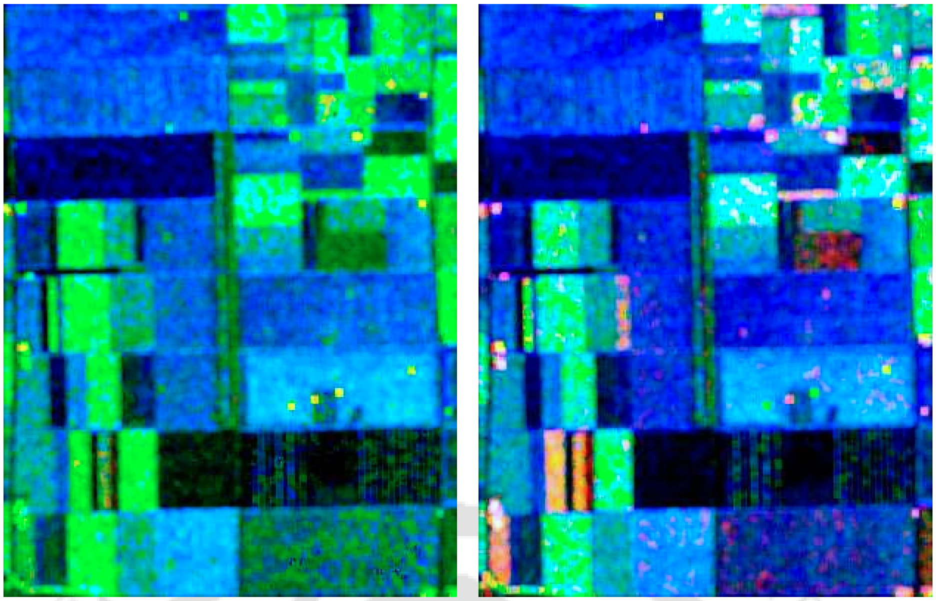

(a) (b)

Figure 4.5: Colour-coded image with red,P_d; green,P_v; blue,P_s estimated after Freeman-Durden decomposition of (a) hybrid-Pol and (b) quad-Pol.

circular polarization (RHCP) wave $\underline{R}$ through the scattering matrix $\mathbf{S}$ as follows.

$$\underline{E}_B = \mathbf{S}\underline{R}, \tag{4.12}$$

where

$$\underline{R} = \left(\frac{1}{\sqrt{2}}\right)\begin{bmatrix} 1 & -j \end{bmatrix}^T \tag{4.13}$$

- Step 2: Derive the corresponding $\underline{E}_H$ and $\underline{E}_V$ vectors from $\underline{E}_B$, which is received by the dual polarized antenna.

$$\begin{aligned} \underline{E}_H &= \begin{bmatrix} 1 & 0 \end{bmatrix} \underline{E}_B = \left(\tfrac{1}{\sqrt{2}}\right)[S_{xx} - jS_{xy}] \\ \underline{E}_V &= \begin{bmatrix} 0 & 1 \end{bmatrix} \underline{E}_B = \left(\tfrac{1}{\sqrt{2}}\right)[S_{xy} - jS_{yy}] \end{aligned} \tag{4.14}$$

- Step 3: From $\underline{E}_H$ and $\underline{E}_V$, evaluate the four elements of the coherency matrix $\mathbf{J}$ as shown in Section 1.2.1.1.

$$
\begin{aligned}
2J_{xx} &= \left\langle |S_{xx}|^2 \right\rangle + \left\langle |S_{xy}|^2 \right\rangle + j\left\langle S_{xx}S_{xy}^* \right\rangle - j\left\langle S_{xy}S_{xx}^* \right\rangle \\
2J_{xy} &= \left\langle S_{xx}S_{xy}^* \right\rangle + \left\langle S_{xy}S_{yy}^* \right\rangle - j\left\langle |S_{xy}|^2 \right\rangle + j\left\langle S_{xx}S_{yy}^* \right\rangle \\
J_{yx} &= J_{xy}^* \\
2J_{yy} &= \left\langle |S_{yy}|^2 \right\rangle + \left\langle |S_{xy}|^2 \right\rangle - j\left\langle S_{yy}S_{xy}^* \right\rangle + j\left\langle S_{xy}S_{yy}^* \right\rangle
\end{aligned}
\tag{4.15}
$$

- Step 4: From the coherency matrix **J**, the Stokes vector $\underline{G}$ parameters are obtained as follows.

$$
\begin{aligned}
G_0 &= J_{xx} + J_{yy} \\
G_1 &= J_{xx} - J_{yy} \\
G_2 &= \mathrm{Re}\left\{\left\langle S_{xx}S_{xy}^* \right\rangle + \left\langle S_{xy}S_{yy}^* \right\rangle\right\} - \mathrm{Im}\left\langle S_{xx}S_{yy}^* \right\rangle \\
G_3 &= -\mathrm{Im}\left\{\left\langle S_{xx}S_{xy}^* \right\rangle + \left\langle S_{xy}S_{yy}^* \right\rangle\right\} - \mathrm{Re}\left\langle S_{xx}S_{yy}^* \right\rangle + \left\langle |S_{xy}|^2 \right\rangle
\end{aligned}
\tag{4.16}
$$

Two parameters directly obtained from Stokes parameters are degree of polarization (DoP) m and the relative phase (RP) δ. The DoP and RP are defined in Equation (2.20) and (2.21), respectively.

DoP values for various scatterer types are as follows.

- For pure target, $m = 1$.
- For distributed target, $m = 0$.
- For partial targets, the DoP has the range of $0 < m < 1$.

RP values for various scattering mechanisms are as follows.

- For trihedral or single bounce, $\delta = 90^0$.
- For dihedral or double bounce, $\delta = -90^0$.

For single bounce, the transmitted polarization change the sense of rotation after reflection. For double bounce, it remains the same. Therefore if RHCP is transmitted, then for single bounce and double bounce, received polarization will be LHCP (left-hand circular polarization) and RHCP, respectively.

For San Francisco image, the DoP and RP histograms are plotted in Figure 4.6. The RP histogram plot suggests that double bounce (urban area) is the dominant scattering mechanism followed by single bounce (ocean area).

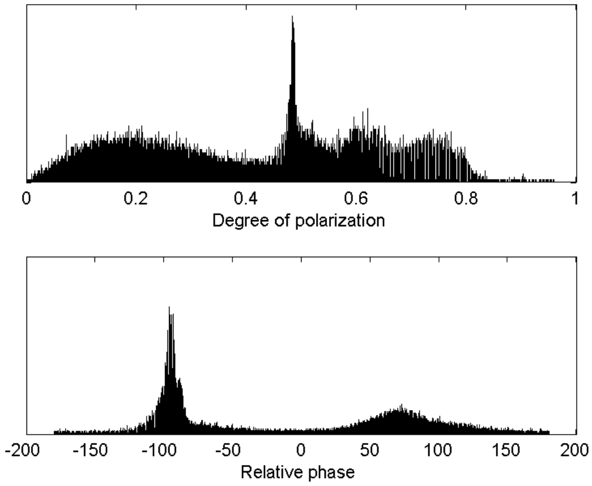

Figure 4.6: DoP and RP histograms for full image of San Francisco region.

From the literature survey on hybrid-Pol in Section 2.3, it was observed that there are quite a few methods reported in literature for the analysis of recently proposed hybrid-Pol data. These methods show that hybrid-Pol data has a rich potential for further quantitative analysis. This led us to find new approaches for the analysis of hybrid-Pol data. Three new approaches are proposed for the analysis of the hybrid-Pol data that we will discuss in next.

4.2.1 A unsupervised classification of hybrid-Pol data based on relative phase

We develop an unsupervised classification scheme for hybrid-Pol data based on the relative phase angle δ. It has been observed that for single and double bounce the δ values are $+90^0$ and -90^0, respectively, if RHCP is transmitted. We found that for volume scattering δ is uniform distributed over the range -180^0 to 180^0. This is because, when the multiple reflections from different branches of a tree are added, it is equiprobable that they add in phase or out of phase. Hence the phase data is uniformly distributed over the range -180^0 to 180^0. So, for the three basic scattering mechanisms, δ values are different. This inspired us to design an unsupervised classification based on the parameter δ.

The phase histogram of different landcover types that corresponds to the three basic scattering mechanisms have been studied and some observations are made as follows.

- Single bounce (Ocean and Bare soil): The phase histogram is Gaussian distributed with mean -88^0 and variance of 8 as shown in Figure 4.7(a).
- Double bounce (Urban Area and semi-deciduous forest): The phase histogram is Gaussian distributed with mean 73^0 and variance of 700 as shown in Figure 4.7(b).
- Volume scattering (Forest): The phase histogram is uniform distributed over the range -180^0 to 180^0. Phase histogram for forest area is shown in Figure 4.7(c).

Note: If RHCP is transmitted, the ideal value of δ for single and double bounce are $+90^0$ and -90^0, respectively. However, due to imperfect circular transmission, δ will not be exactly at $\pm 90^0$.

The observed phase histograms for different land types were approximated by continuous density functions. Maximum likelihood estimation (MLE) is used for fitting a statistical model to the data, and providing estimates for the model's parameters. Then the image-pixels are classified by maximizing the aposteriori probabilities obtained using Bayes' rule. Figure 4.8 shows the block diagram of the Bayes classifier, where d_i represents the discriminant function. Specifically, we have $d_i = p(x|C_i)$, where $p(x|C_i)$ is the probability that a pixel with feature vector $\underline{x}$ belongs to class C_i. The classified image, as obtained using this algorithm, is shown in Figure 4.9. This result may be compared with the H/α classification of quad-Pol data shown in Figure 3.2(b). From visual inspection of both the classification results, it can be observed that the performance of both the techniques are almost same. This illustrates the rich potential of hybrid-Pol system as a single parameter produces a classification results which is comparable to H/α classification results obtained from quad-Pol data.

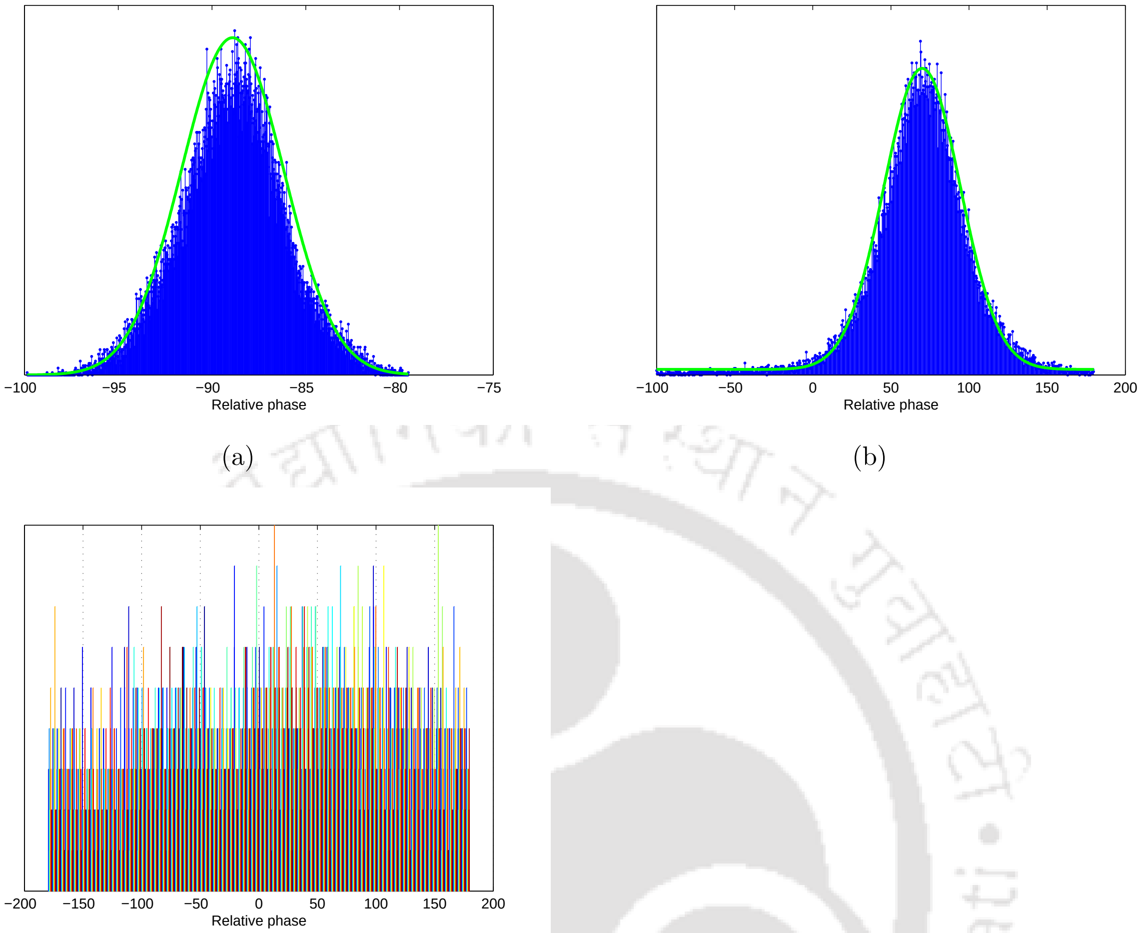

(a)

(b)

(c)

Figure 4.7: Relative phase histogram for (a) ocean area, (b) urban area and (c) forest area in San Francisco image.

4.2.2 H/α decomposition of hybrid-PolSAR images

In this subsection, we develop a hybrid-Pol version of the entropy/alpha decomposition method. The dual linear Pol version of the entropy/alpha decomposition method has been reported in [40, 77]. For hybrid-Pol systems, the wave coherency matrix $\mathbf{J}_{hyb}$ is given by

$$\mathbf{J}_{hyb} = \begin{bmatrix} \langle S_{RH} S_{RH} \rangle & \langle S_{RH} S_{RV} \rangle \\ \langle S_{RV} S_{RH} \rangle & \langle S_{RV} S_{RV} \rangle \end{bmatrix} \tag{4.17}$$

This coherency matrix is a complex, positive semi-definite, Hermitian, 2 × 2 matrix. The eigenvector decomposition of the covariance matrix produces two eigenvalues, λ_1 and

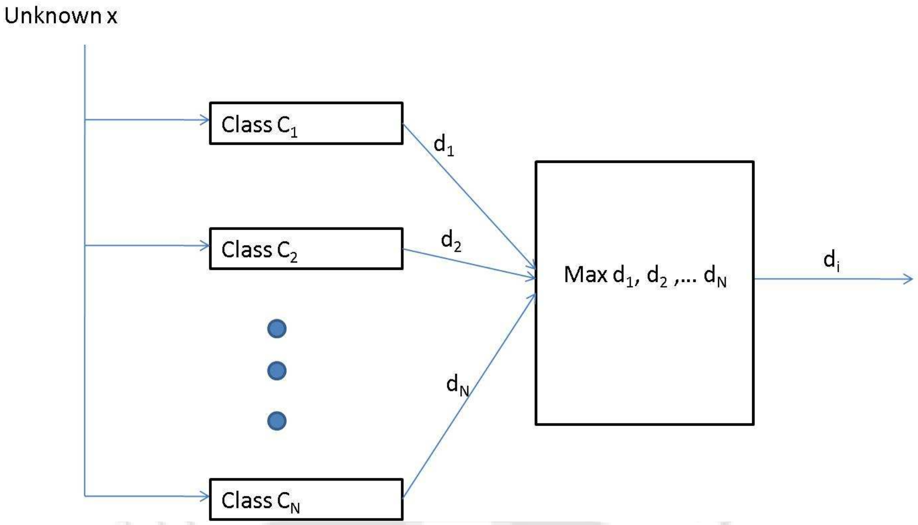

Figure 4.8: Block diagram of Bayes classifiers.

λ_2 and the two corresponding eigenvectors.

The hybrid-Pol entropy is then defined by

$$H = -P_1 \log P_1 - P_2 \log P_2, \tag{4.18}$$

where P_1 and P_2 are the pseudo-probabilities. The pseudo-probabilities are defined as

$$P_i = \frac{\lambda_i}{\sum\limits_{k=1}^{2} \lambda_k}, \ with \ \sum_{k=1}^{2} P_k = 1. \tag{4.19}$$

The role of entropy is the same as entropy of quad-Pol data which accounts for target randomness. The eigen vectors are given by

$$u_i = e^{j\phi_i} \begin{bmatrix} \cos\alpha_i & \sin\alpha_i e^{j\delta_i} \end{bmatrix}^T. \tag{4.20}$$

α angle is obtained from the α_i angle of each eigenvector as follows.

$$\alpha = \sum_{i=1}^{2} P_i \alpha_i \tag{4.21}$$

Here the alpha angle characterizes the average scattering mechanisms of hybrid-Pol

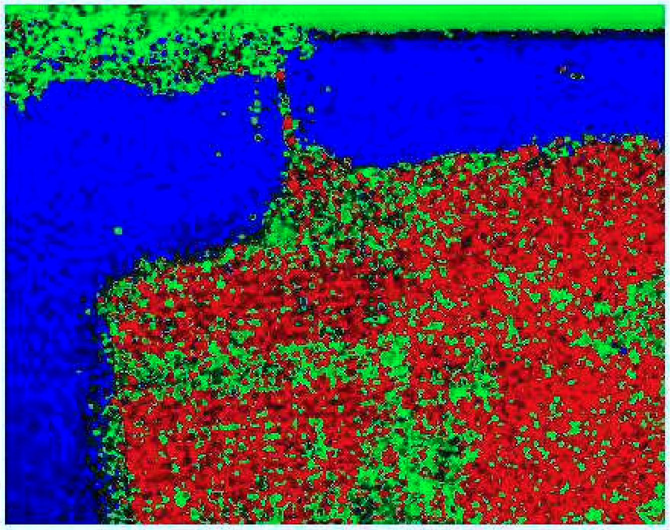

Figure 4.9: Classification of San Francisco image using relative phase.

SAR system. Considering the same boundary sets for hybrid-Pol as for quad-Pol, the H/α classification map has been obtained. We have also obtained a H/α classification map with new boundaries estimated from the procedure discussed in Section 3.4. Both the results are plotted in Figure 4.10. It is observed that different land features are poorly classified in both the classification maps, with the new boundary classification map performing slightly better.

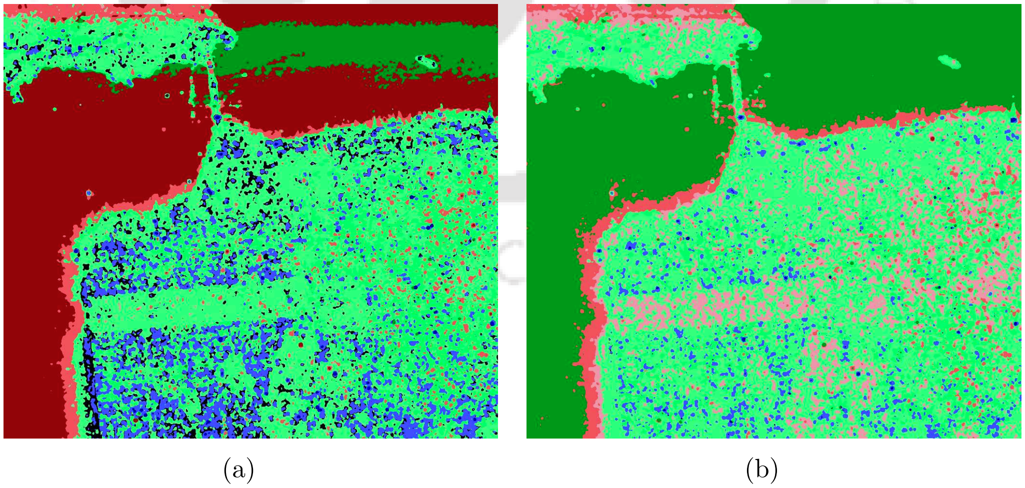

(a) (b)

Figure 4.10: Hybrid-Pol H/α classification map with (a) old boundary and (b) new boundary.

4.2.3 PCA decomposition of hybrid-Pol data

In radar polarimetric field, principle component analysis (PCA) is used as a target decomposition technique. In the current work, PCA decomposition of hybrid-Pol data is carried out. At first, we discussed about the application of PCA to radar image dataset. Then the PCA algorithm is implemented on hybrid-Pol data.

4.2.3.1 Application of PCA to radar image dataset

The main purpose of PCA is to convert a set of correlated random variables (RV) into a new set of uncorrelated RV, such that the first few components (principal components) retain most of the variations contained in all of the original variables. PCA can be used to find a suitable representation of a dataset using less number of variables, while retaining most of the variations in the dataset [78].

Suppose that the dataset consists of N images of size $l \times m$ each. Each image is considered as a point in an n dimensional space, where $n = l \times m$. Let $x_i, i = 1, 2, ..., N$ represent the i^{th} image converted into a vector of dimension $n \times 1$. Using a linear transformation matrix $\mathbf{W}$, x_i can be mapped to y_i [79] as follows.

$$y_i = \mathbf{W}^T x_i. \tag{4.22}$$

Let the dimension of y_i be $k \times 1$, such that $k < n$. PCA is the linear transformation $y_i = \mathbf{W}_{PCA}^T\, x_i$, where $\mathbf{W}_{PCA}$ is chosen so as to preserve as much variance as possible during the transformation.

PCA is obtained through eigenvector analysis of the covariance matrix $\mathbf{C}$. We can estimate the covariance matrix $\mathbf{C}$ of the image-vectors in the training dataset by the following operation:

$$\mathbf{C} = \sum_{i=1}^{n} (x_i - m)(x_i - m)^T, \tag{4.23}$$

where $m = \frac{1}{N} \sum\limits_{i=1}^{N} x_i$.

The derivation of principal components for the image datasets can be presented with the following procedure:

- Calculate the covariance matrix $\mathbf{C}$ by using Equation (4.23). There are N images; hence the size of $\mathbf{C}$ is $N \times N$.
- Compute the eigenvalues and eigenvectors of $\mathbf{C}$ through eigenvector analysis.
- Sort the eigenvectors by eigenvalues in descending order.
- A transformation matrix is formed by stacking the desired eigenvectors as columns of the matrix.
- Finally, principal components are derived by multiplying the transpose of the transformation matrix $\mathbf{W}_{PCA}$ with the sample data.

4.2.3.2 Application of PCA to hybrid-Pol dataset

In the current work, we applied PCA decomposition techniques to hybrid-Pol data for San Francisco area. Each element of the Stokes vector, is considered here as sample point. There are 4 elements in the Stokes vector. After application of PCA, it is observed that first 3 components contain more than 90% of variance. These 3 principal components are represented in a single three-colour composite image (RGB) as shown in Figure 4.11(a). To check the efficacy of this approach, the PCA RGB image can now be compared with the Freeman-Durden RGB image, which is shown in Figure 4.11(b). The Freeman-Durden RGB image is obtained by applying Freeman-Durden decomposition to quad-Pol data. On direct visual comparison of both the images, it is observed that different land features are correctly discriminated by both the approaches.

This leads us to propose an unsupervised classification technique based on the analysis of PCA decomposition of hybrid-Pol data. An analogy between scattering mechanisms and principal components is drawn here. First, like principal components, the scattering mechanisms are also uncorrelated. Secondly, the dominant scattering mechanism is represented by the first principal component. For example, from the RPD histogram for San

Francisco image shown in Figure 4.6, it was observed that double bounce (urban area) is the dominant scattering mechanism followed by single bounce (ocean area). Similarly, here, it is observed that the first principal component is dominating for pixels in urban area, while the second principal component is dominating for pixels in ocean area. Based on the above findings, we can state that the first principal components corresponds to the dominant scattering mechanism; whereas the second principal component corresponds to next to dominant scattering mechanism and so on. Therefore, for San Francisco image, the first principal component corresponds to double bounce, the second principal component corresponds to single bounce, and third principal component corresponds to volume scattering.

Table 4.1 demonstrates the comparison of the three scattering mechanisms obtained from Freeman-Durden decomposition of fully polarimetric SAR data with the three principal components generated from application of PCA to hybrid-Pol data. The comparison shows a good agreement between both the approaches for single bounce and double bounce scattering mechanisms. However, for volume scattering the matching is not good. The reason may be that the Freeman-Durden decomposition of fully polarimetric SAR data may not be fully accurate. For example, many of the urban areas in the Freeman RGB image (Figure 4.11(b)) looks green, which is the colour assigned for volume scattering. The other reason may be that PCA decomposition is implemented on hybrid-Pol data which occupies half of the polarization information-space provided by fully polarimetric data, which is used by Freeman-Durden decomposition technique.

Table 4.1: Confusion matrix for Freeman-Durden decomposition of quad-Pol and PCA decomposition of hybrid-Pol.

FD_FP\PCA_hybrid	Single bounce	Double bounce	Volume scattering
Single bounce	83.76	07.20	9.04
Double bounce	05.73	73.79	20.48
Volume scattering	21.78	24.825	53.39

Having an insight of the correspondence between scattering mechanisms and principal components, we propose an unsupervised classification technique based on the PCA components. At first the PCA components are linked to the scattering mechanisms. Then each pixel is classified into the scattering categories based on the dominance of PCA components. The classification result is shown in Figure 4.12. It can be observed that all the land features are correctly classified. One drawback with this approach is that if the number of scattering mechanisms are higher than the number of principal components, then by principle this approach can not be implemented.

4.3 Summary

In this chapter, the potential of the recently proposed hybrid-Pol configuration was investigated. Hybrid-Pol was compared with quad-Pol configuration based on information content. The comparison has been carried out based on two different approaches. From these analysis, we have shown that information content in hybrid-Pol is less but comparable to that in quad-Pol.

We have also proposed three new approaches for the analysis of hybrid-Pol data. In the first approach, an unsupervised classification scheme based on the relative phase was developed. It was shown that by using this single parameter, the basic scattering mechanisms can be discriminated. In the second approach, we have developed a hybrid-Pol version of the entropy/alpha decomposition method. Two hybrid-Pol versions of H/α classification maps were obtained considering the new and the old entropy/alpha boundary sets as described in Section 3.4. Different land features were observed to be poorly classified in both the classification maps, with the new boundary classification map performing slightly better. In the third approach, principal component analysis of hybrid-Pol data was carried out. We have shown that there is a strong analogy between scattering mechanisms and principal components. Based on this, an unsupervised classification technique for hybrid-Pol data was proposed and developed. It was observed that all land features are correctly classified by this PCA based classification technique.

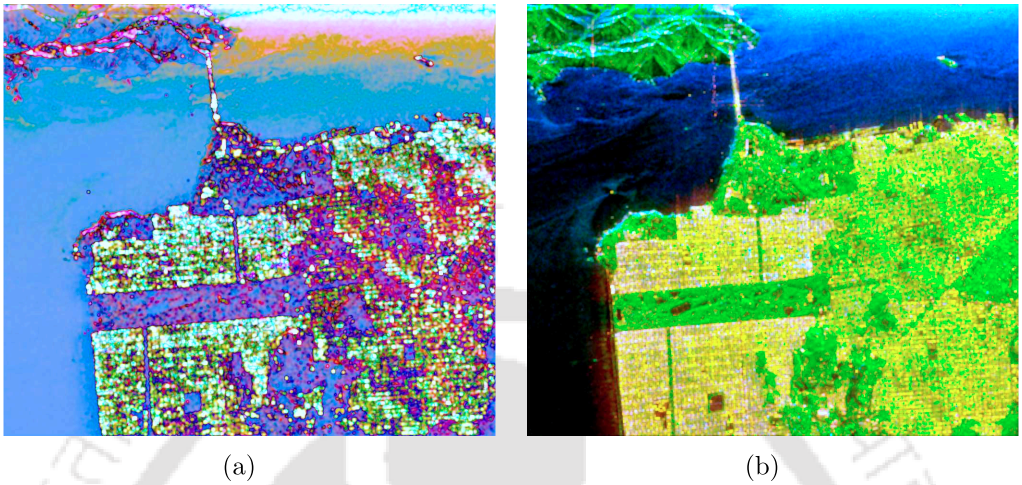

(a) (b)

Figure 4.11: (a) RGB image generated after PCA decomposition of hybrid-Pol data and (b) RGB image generated after Freeman-Durden decomposition of quad-Pol data.

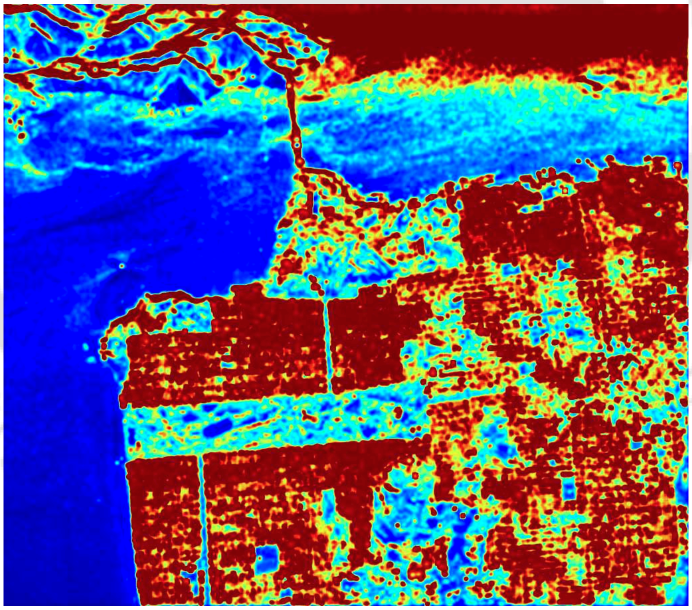

Figure 4.12: Classification using PCA decomposition of hybrid-Pol data.

5

Polarimetric SAR Image Enhancement Techniques

Contents

In this chapter, we discuss and develop different polarimetric SAR (PolSAR) image enhancement techniques based on sidelobe noise suppression. In Section 2.4, we provided a review of different classes of sidelobe noise suppression techniques. Among these techniques, non liner apodization (NLA) is an effective and computationally efficient technique used for sidelobe suppression in SAR imagery. In this chapter, the thesis deals with sidelobe noise suppression in PolSAR images using NLA techniques.

SAR data is always bandlimited due to hardware limitations. For image reconstruction, when inverse Fourier transform of these bandlimited data is taken, it produces significant high intensity sidelobes. Presence of sidelobes obscure the details of low intensity scatterers in the image. To reduce the sidelobe induced artifacts in SAR images, a class of non linear operators, known as non linear apodization techniques [58], have been developed. There are different types of NLA techniques, viz. dual apodization (DA), complex dual apodization (CDA) and spatially variant apodization (SVA). In our current work, we propose a new NLA technique that completely wipes out the sidelobes and simultaneously reduces the mainlobe width. We also develop a 2-dimensional (2-D) version of CDA algorithm. Like conventional SAR images, PolSAR images are also affected by sidelobe artifacts. The NLA techniques, which were originally developed for SAR imagery, are extended to PolSAR images. Finally, it is shown that sidelobe suppression in PolSAR images helps in better target identification.

Unlike in previous chapters, where we were using PolSAR remote sensing data, here we use airborne polarimetric dataset of ground targets. The reason is, in SAR images for remote sensing, each pixel characterizes a small geographical area on earth surface. This means that each pixel carries a certain amount of information, which can not be ignored. However, in SAR based target analysis, the objective is different; it is to identify the target in presence of various noises and background clutter. Therefore, it is suitable to apply sidelobe suppression techniques to SAR images of distinct targets.

The rest of the chapter is organized as follows. In the next section, a brief description of NLA techniques is given. In Section 5.2, a new NLA algorithm is proposed. In Section 5.3, a 2-D version of CDA algorithm is explained. In Section 5.4, PolSAR image enhancement through various NLA techniques are discussed. Section 5.5 deals with information extraction from apodized PolSAR images. Section 5.6 gives summary of the work presented in this chapter.

5.1 A short review of NLA

The most common method for time to frequency domain transformation is Fourier transform (FT). To compute the exact spectrum of a signal using FT, the values of a signal for an infinite time interval are required. However, because of practical limitations, every observed signal that we process is of finite duration. Therefore, the spectrum of a signal is approximated from a finite data record. For example, when Fourier transform of a finite duration sine wave is taken, we get a sinc function rather than an impulse function as shown in Figure 5.1. The sinc curve has a mainlobe, which contains the peak and has a width up to the first zero crossings, and a set of sidelobes comprising of the oscillating remainder on both sides of the mainlobe. The composite function of the mainlobe and the sidelobes is termed as the impulse response (IPR) of a system. Hence, the finiteness of the data causes spectral leakage and degradation of the spectral resolution in the transformed domain. These two problems are recapitulated below.

- Spectral leakage: The power of the signal that is concentrated at a single frequency spreads across the entire frequency range. This phenomenon is called spectral leakage and is characterized by sidelobes in the IPR.
- Degradation in spectral resolution: The width of mainlobe defines the spectral resolution of the system. Therefore, the spectral resolution decreases as the width of mainlobe increased to $4 \times \pi/N$ from ideally zero. Here N is the length of the data.

In an IPR, the location of the center of mainlobe is related to the frequency of the sine wave. Sidelobes of an IPR are unwanted and do not convey any information about the

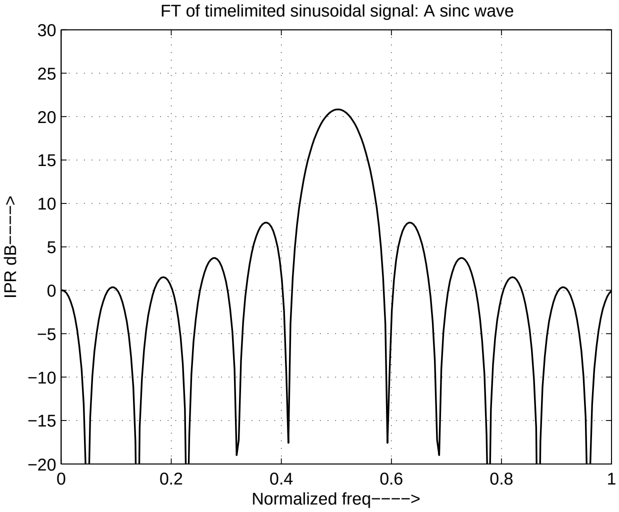

Figure 5.1: A Sinc wave.

signal[1]. Moreover, the presence of sidelobes reduces the detectability of spectral components of relatively low amplitudes. Therefore, there is a need to suppress the sidelobes in the IPR. In literature, the suppression of sidelobes is referred to as apodization. It is a term taken from optics, in which it refers to the suppression of diffraction sidelobes. Traditionally, the sidelobe of an IPR is reduced by multiplying an amplitude weighting function to the data prior to FT. However by this method, a reduction of the sidelobes is obtained at the expense of an increase in the width of the mainlobe of the IPR and hence a loss in spectral resolution. To break this compromise, in the last few decades, researchers have tried a variety of non-linear techniques to reduce sidelobes without degrading the mainlobe resolution. These techniques are known as nonlinear apodization (NLA) algorithms and have potential application in radar field [58] and a range of other fields [59, 60]. Here, we discuss three types of NLA techniques namely dual-apodization (DA), complex dual-apodization (CDA) and spatially variant apodization (SVA).

DA is a technique where output signal is computed twice, once using uniform weighting and a second time using Hanning weighting. At each spatial location, these two values are

---

[1] This is only true for band limited signal which has been sampled at Nyquist rate.

compared and the final output is taken as the lesser of the two. The DA IPR appears to have the narrow mainlobe of the uniform IPR and the lower sidelobes of Hanning IPR. CDA is similar in operation to DA, but exploits the usefulness of complex phase part. The complex dual apodized image is obtained by following a two step procedure.

(i) Compute two versions of the IPR, one using uniform weighting and the other using Hanning weighting.

(ii) At each spatial location, if the in-phase, I, components of the two IPRs have opposite signs, select value zero; otherwise select the I value which has the smaller absolute value of the two. Do likewise for the quadrature-phase, Q, component.

CDA is an efficient NLA method as the sidelobes are almost completely suppressed. This is because, the sidelobes for the two IPRs are opposite in sign. The mainlobe of the two IPRs overlap and have the same sign. Therefore, in the mainlobe region, the smaller absolute value of the two is selected.

Spatially Variant Apodization (SVA) is a generic NLA algorithm in which an arbitrary number of weighting functions are used. Thus, better sidelobe control is achieved as the number of apodization-windows increases arbitrarily from which we choose one. SVA is based on the use of special properties of cosine-on-pedestal weighting functions [61]. This algorithm can find out a weighting function from among the infinite number of cosine-on-pedestal weighting functions that provide the zero crossing for each sample in the sidelobe region. The cosine-on-pedestal function can be written as

$$A(n) = 1 + 2w\cos(\frac{2\pi n}{N-1}), \quad 0 < n \leq N-1 \tag{5.1}$$

where w is a weighting factor. This family of weightings range from uniform weighting ($w = 0$: all pedestal, no cosine) to Hanning weighting ($w = 0.5$: all cosine, no pedestal). Hamming window is a special case of cosine-on-pedestal which nulls the first sidelobe ($w = 0.43$). Similarly, any unweighted aperture sinc-function sidelobe can be suppressed using one of the family of cosine-on-pedestal weighting functions. Taking the N point discrete Fourier transform of a cosine on pedestal weighting yields the Nyquist-sampled IPR:

$$a(m) = w\delta_{m,-1} + \delta_{m,0} + w\delta_{m,1}, \tag{5.2}$$

where δ is the Kronecker delta function. Let $g(m)$ be the samples of either real (I) or imaginary (Q) component of a uniformly weighted Nyquist-sampled signal. Using the three-point convolver given in Equation (5.2) to achieve a given cosine-on-pedestal aperture weighting, $g(m)$ is replaced by $g'(m)$ as follows:

$$g'(m) = w(m) * g(m-1) + g(m) + w(m) * g(m+1). \tag{5.3}$$

As $w(m)$ varies from 0 to 0.5, the frequency domain amplitude weighting varies from cosine-on-zero pedestal (Hanning) at $w(m) = 0.5$ to uniform weighting at $w(m) = 0$. The task, therefore, is to find the $w(m)$ which minimizes $|g'(m)|^2$ with respect to $w(m)$. Solving for $w(m)$ gives

$$w(m) = \frac{-g(m)}{g(m-1) + g(m+1)}. \tag{5.4}$$

Constraining $w(m)$ in Equation (5.4) to lie in the interval $[0, 0.5]$, and inserting it into Equation (5.3) yields the output IPR.

$$g'(m) = \begin{cases} g(m) & w(m) < 0 \\ 0 & 0 \leq w(m) \leq 0.5 \\ g(m) + 0.5[g(m-1) & \\ +g(m+1)] & w(m) \geq 0.5 \end{cases} \tag{5.5}$$

Operation shown in Equation (5.5) is performed on the I and Q values independently. A 2-dimensional (2-D) version of this SVA algorithm was developed in [58].

5.2 A local gradient based NLA algorithm

In this section, we propose a new NLA technique that suppresses the sidelobes completely and also enhances the mainlobe resolution[2] by many folds . This new technique is based on the fact that mainlobe of an IPR is twice as wide as that of sidelobes. For example, from Figure 5.1, it can be observed that the mainlobe width is double of the sidelobe width. If we consider an IPR having N number of samples, then the mainlobe width is $4 \times \pi/N$ and the width of the sidelobe is $2 \times \pi/N$. Using this simple fact, it is possible to develop an algorithm that can find the location of mainlobes and the sidelobes in an IPR. To find the location of mainlobes and sidelobes in the IPR, local gradient method is being used. Hence this new NLA algorithm is referred to as Local gradient based NLA (LGNLA). Once the locations of sidelobes and mainlobes are determined, we can eliminate the unwanted sidelobes and reduce the mainlobe width. The implementation of this new algorithm is depicted in Algorithm 2. For 2-D signal, the algorithm may be implemented as depicted in Algorithm 3.

Like SVA techniques, the proposed method can suppress the sidelobes in an IPR completely. In addition to this, it has the following advantages.

- It further enhances the frequency resolution.
- It can be implemented on data sampled at non-integer multiple of Nyquist rate.
- It can be implemented on absolute valued image.
- It is computationally simpler.

5.2.1 Results and observations

Here, we compare the performance of SVA algorithm with the proposed algorithm. It is demonstrated that the proposed LGNLA method performs better in suppressing the sidelobes and enhancing the resolution. For demonstration of the said advantages, a multi-tone sinusoidal signal is considered as a test signal. The components are located at three

---

[2] The enhanced resolution in an IPR can be achieved by narrowing the mainlobe width.

Algorithm 2 Local gradient based NLA algorithm

```
Require: An absolute valued IPR y(n) of length $N$.
Ensure: The sidelobes are suppressed and the mainlobe width is reduced.
  for $i = 1$ to $N$ do
    Find all the zero crossing points $i$ (local minimum points) of the spectrum that satisfy
    the condition $y(i) <= y(i-1)$ and $y(i) <= y(i+1)$. This is nothing but the local
    gradient method which has been used for finding the zero crossing points.
    Store the value of $i$ in an array arr1.
  end for
  Let $L = length(arr1)$.
  for $i = 1$ to $L - 1$ do
    Find the difference between the two consecutive zero crossing point by using $D(i) =
    arr1(i) - arr1(i-1))$.
  end for
  Take the mean $M$ of all the differences: $M$=mean($D$).
  if $D > M + 1$ then
    return the corresponding zero crossing points of this difference determine the main-
    lobe location.
  else
    return the corresponding zero crossing points of this difference determine the sidelobe
    location.
  end if
  Once the locations of the sidelobes and mainlobes are determined, then the sidelobes can
  be eliminated and mainlobe can be represented by an impulse located at the center of
  the two zero crossing points of that mainlobe.
```

Algorithm 3 Local gradient based NLA algorithm: 2-D version

```
Require: An absolute valued image.
Ensure: The sidelobes are suppressed and the mainlobe width is reduced.
  Apply the 1-D version of the algorithm row wise to the original image.
  Then, apply the 1-D algorithm column wise to the original image.
  Take the maximum of both the resultant image.
```

different frequencies 0, 45, 89 and 90 Hz. This test signal is sampled at twice the Nyquist rate. The frequency spectrum of the unweighted data, SVA apodized spectrum and the LGNLA algorithm spectrum are shown in Figure 5.2.

From this figure, it is observed that the two components with frequency 89 and 90 Hz are merged in Fourier and SVA spectrum, but quite distinguishable in the proposed LGNLA algorithm's spectrum. These two components can be distinguished in SVA spectrum if the separation between them is atleast 6 Hz. This is demonstrated in Figure 5.3. Hence, it can be inferred that the frequency resolution has been increased by a factor of 6 by the proposed LGNLA method in comparison to classical SVA method. We have also demonstrated the performance of the proposed LGNLA algorithm in presence of noise. The effect of noise on LGNLA algorithm is evaluated at an SNR of $10dB$. This is demonstrated in Figure 5.4. From this figure, it is seen that performance of both SVA and LGNLA algorithms in presence of noise are almost the same. However as SNR decreases, LGNLA algorithm is not able to separate two closely placed frequency components. Hence, the frequency resolution decreases as SNR decreases.

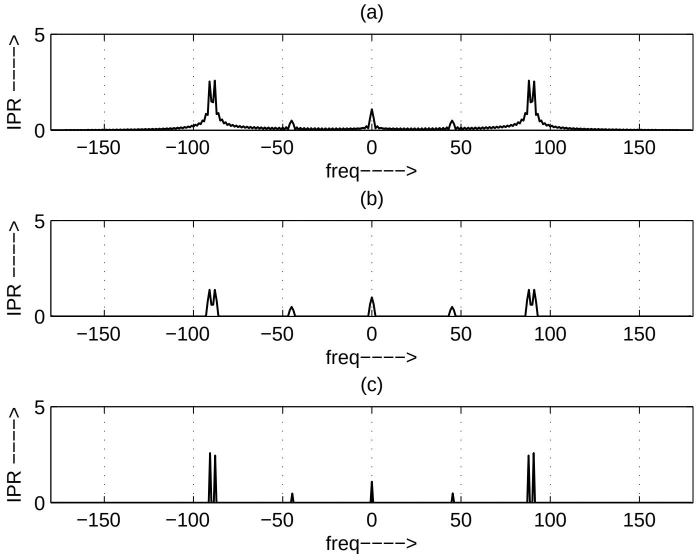

Figure 5.2: (a) The spectrum of unweighted signal. (b) SVA spectrum. (c) LGNLA spectrum.

To evaluate the performance of the proposed algorithm for 2-D case, Moving and stationary target acquisition and recognition (MSTAR) airborne SAR image public data set is used. MSTAR program was a DARPA supported project for the collection of a standardized mono-static SAR image database, collected using the Sandia National Laboratories Twin Otter SAR sensor payload operating at X-band [79]. The targets used for the present work is an MSTAR T72 tank. The original SAR image is shown in Figure 5.5(a). The resulting images after 2-D SVA and LGNLA algorithm's implementation are shown in Figures 5.5(b)

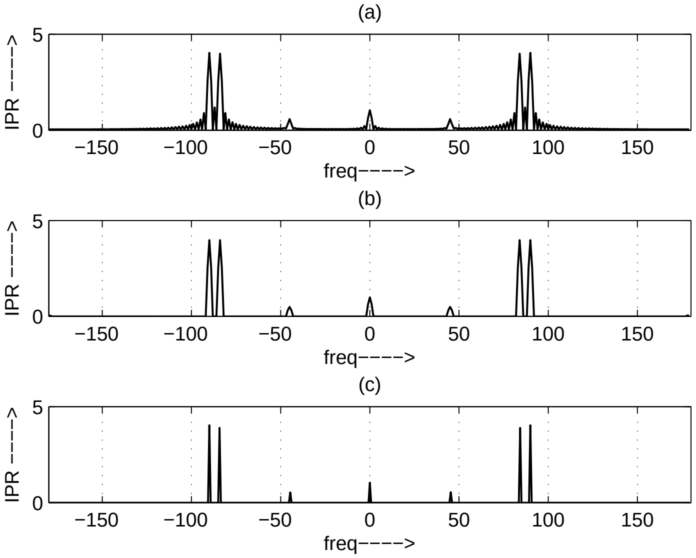

Figure 5.3: (a) The spectrum of unweighted signal. (b) SVA spectrum. (c) LGNLA spectrum.

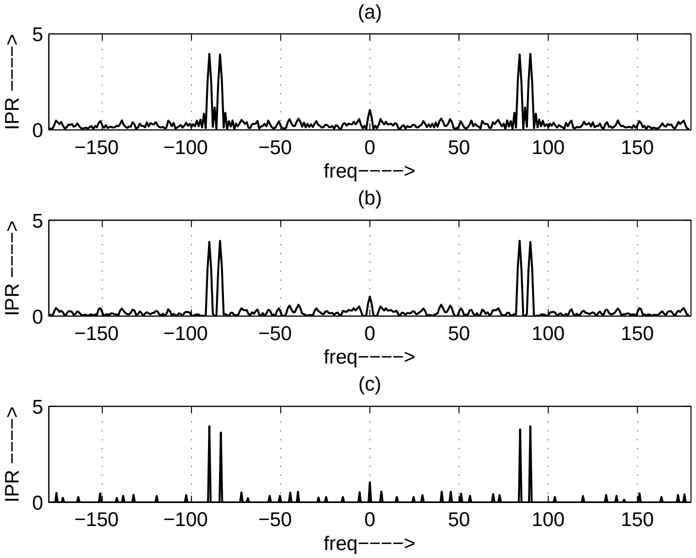

Figure 5.4: (a) The spectrum of unweighted signal+Noise. (b) SVA spectrum. (c) LGNLA spectrum.

and 5.5(c), respectively. On comparison of these two figures, it can be observed that the target in LGNLA apodized image looks clear and distinct, in comparison to SVA image.

5.3 An extended CDA technique

In this section, we present the development of a 2-D version of CDA algorithm by extending the original CDA algorithm. This extended 2-dimensional version of CDA algorithm is referred to as extended 2-dimensional CDA (E2CDA). We developed and implemented the E2CDA algorithm using the procedure as detailed in Algorithm 4.

Algorithm 4 Extended 2-dimensional CDA

```
Require: SAR complex phase history data prior to FT operation.
Ensure: The sidelobes in the image are suppressed.
  Compute two versions of the image.
  First, multiply the complex phase history data with the rectangular window and take FT.
  Second, multiply the complex phase history data with the Hanning window and take FT.

  Obtain the $I$ and $Q$ components of both the resultant images.
  for each pixel do
    Select the I components of both the image (I1 and I2).
    make a ($3 \times 3$) mask with the current pixel as the center.
    Compare the sign of all the pixels inside the mask of I1 with the corresponding pixels of I2.
    if there is atleast one mismatch then
      return assign a value zero to the variable I3.
    else
      return assign a value to I3 which has the smaller absolute value between I1 and I2.
    end if
  end for
  Repeat the same procedure for Q component
  Finally form the apodized image by combining both the components as I3+jQ3.
```

In the mainlobe region, all the neighborhood pixels of sinc IPR have the same sign as Hanning's IPR, therefore the smaller absolute value of the two is chosen to retain the mainlobe of sinc IPR. As the sidelobes of the two IPR are opposite in nature, there will be at least one sign change when we compare the neighborhood pixels of two IPR. Therefore, a zero value is assigned to the pixels which are in the sidelobe region.

5.4 PolSAR image enhancement through NLA

In this section, the thesis deals with sidelobe noise suppression in PolSAR images by using NLA techniques. The NLA techniques originally developed for SAR imagery are extended to PolSAR images. The 2-D version of SVA, E2CDA and LGNLA algorithms are used here to suppress the sidelobe noise in PolSAR images. It is expected that better information can be extracted from the PolSAR images if the sidelobe noise is removed from the images.

5.4.1 Results and observations

The results are obtained using the Georgia Technology Research Institute (GTRI) polarimetric data of T-72 tank, which is publicly available. This dataset is an extensive turntable data collected in the second half of 1980's by the GTRI [80]. The GTRI turntable data consists of multi-polarization, X-band SAR phase history. In addition to the tank, there are two corner reflectors on the turntable, which present a strong backscattered energy. Figure 5.6 shows the SAR images of the target at a certain pose for all the four polarizations (HH, HV, VH and VV). We have implemented three algorithms, viz. 2-D version of SVA, E2CDA and LGNLA on each polarization images of PolSAR to suppress the sidelobe noise. The apodized images after implementations of SVA ($HH1$, $HV1$, $VH1$ and $VV1$), E2CDA ($HH2$, $HV2$, $VH2$ and $VV2$) and LGNLA ($HH3$, $HV3$, $VH3$ and $VV3$) algorithms are shown in Figures 5.7, 5.8 and 5.9, respectively. In all the images, the horizontal axis represents the range and vertical axis the cross range dimensions.

To obtain a better knowledge about the target, we need to characterize it through its complete polarimetric scattering matrix. The individual polarization images captures different aspect of the target. Hence, the fusion of the information present in individual images allow us to gather more information about the structure of the target. Here, we have combined all the four polarizations by taking the maximum value among them for each spatial location. The result of the combined PolSAR images and its apodized PolSAR images are shown in Figure 5.10. From visual inspection, it can be observed that sidelobes are suppressed in all the apodized images. Also the strong sidelobes formed by the two corner reflectors are reduced to a large extent. On visual comparison, it is observed that the proposed E2CDA and LGNLA algorithms outperform the classic SVA technique in sidelobe noise suppression of PolSAR images.

5.5 Decomposition of apodized PolSAR images

In Section 5.4.1, all the four polarization images were combined by taking the maximum value of the images at each spatial location. However by doing so, we loose some information about the target, contained in the rest of the three images. In radar polarimetry, different decomposition techniques have been developed that can be used to extract information from the polarimetric scattering matrix and find a suitable representation for the PolSAR images [19]. Here we will discuss about the two such polarimetric decomposition techniques, viz. Pauli and principal component analysis (PCA). We applied both of these techniques to PolSAR images and to its apodized version. Then the information content in resultant image of both the cases are compared. For demonstration purpose, here we consider E2CDA algorithm for apodization of PolSAR images.

5.5.1 Pauli decomposition of apodized PolSAR images

Pauli decomposition of PolSAR images have been discussed in Section 2.1.4. The Pauli basis under reciprocity is given by

$$\begin{pmatrix} 1 & 0 \\ 0 & 1 \end{pmatrix} \begin{pmatrix} 1 & 0 \\ 0 & -1 \end{pmatrix} \begin{pmatrix} 0 & 1 \\ 1 & 0 \end{pmatrix} \tag{5.6}$$

For backscattering case, the three Pauli's components of the decomposition are as follows.

- $Pauli1 = S_{hh} + S_{vv}$, corresponds to odd-bounce scattering,
- $Pauli2 = S_{hh} - S_{vv}$, corresponds to even-bounce scattering (dihedral oriented at 0°), and
- $Pauli3 = 2S_{hv}$, corresponds to rotated dihedral (45° tilted even bounce component).

To demonstrate the efficacy of the approach of applying Pauli decomposition after apodization, we proceed as follows. First, the Pauli decomposition of GTRI PolSAR data is carried out. The resultant three Pauli components are shown in Figure 5.11. Second, the Pauli decomposition is applied on the same PolSAR images after the sidelobe noise has been removed from them using NLA algorithms. The three components of the Pauli decomposition of the apodized PolSAR images are shown in Figure 5.12. Finally, The three Pauli's components are represented in a single three-colour composite image (RGB) for visual inspection. These three components are represented as blue, red and green, respectively. The colour-coded image for the Pauli decomposition of apodized PolSAR images and its apodized version are represented in Figure 5.13. Upon comparison, it is apparent that the target (T72 tank) looks more clear and distinct in the image shown in Figure 5.13(b). Therefore, it is claimed that information extraction through target decomposition is better when sidelobe noise is removed from the PolSAR images.

5.5.2 PCA decomposition of apodized PolSAR images

In the current subsection, the application of principal component analysis (PCA) decomposition technique to PolSAR images before and after apodization is discussed.

The application of PCA to radar image datasets were discussed in Section 4.2.3.1. The same procedure is followed here, except for the change in the input data-type. The four polarization images (HH, HV, VH, and VV) are considered as the sample points in the PCA based algorithm. The principal components are obtained on the application of PCA to PolSAR images. Then, the first principal component corresponding to largest eigenvalue is retained, which contains around 80% of the total variance.

5.5.2.1 Results and observations

Figures 5.14(a) and 5.14(b) show the results of application of PCA on PolSAR images and its apodized version, respectively. Upon comparison of both the results, it is observed that the target looks more clear and distinct in the later image. Therefore, we conclude that better information about the target of interest can be extracted from the apodized PolSAR images.

5.6 Summary

In this chapter, we have discussed about PolSAR image enhancement using NLA techniques. The potential of these algorithms in suppressing the sidelobe noise in SAR image was explained. A new NLA algorithm was proposed, which can suppress the sidelobes completely and simultaneously reduce the mainlobe width beyond the limit of super-resolution. An extended CDA algorithm was also developed that can be implemented on a 2-D signal to eliminate the sidelobes. The existing and proposed NLA techniques originally developed for SAR imagery were extended to PolSAR images. Finally, it was validated that sidelobe suppression in PolSAR images helps in better target identification.

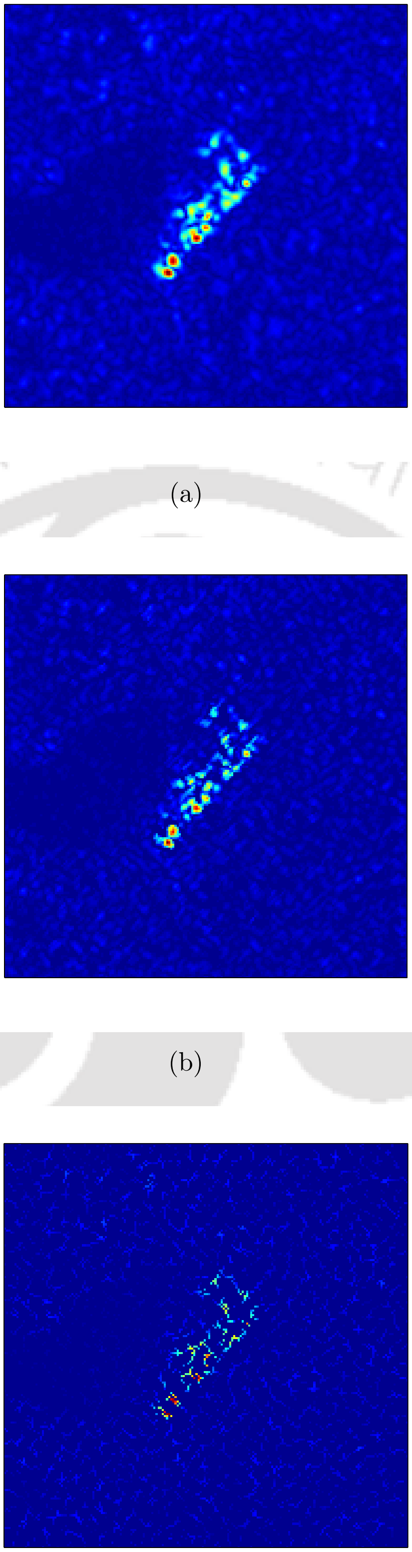

(a)

(b)

(c)

Figure 5.5: (a) Original image, (b) SVA apodized image, (c) LGNLA apodized image.

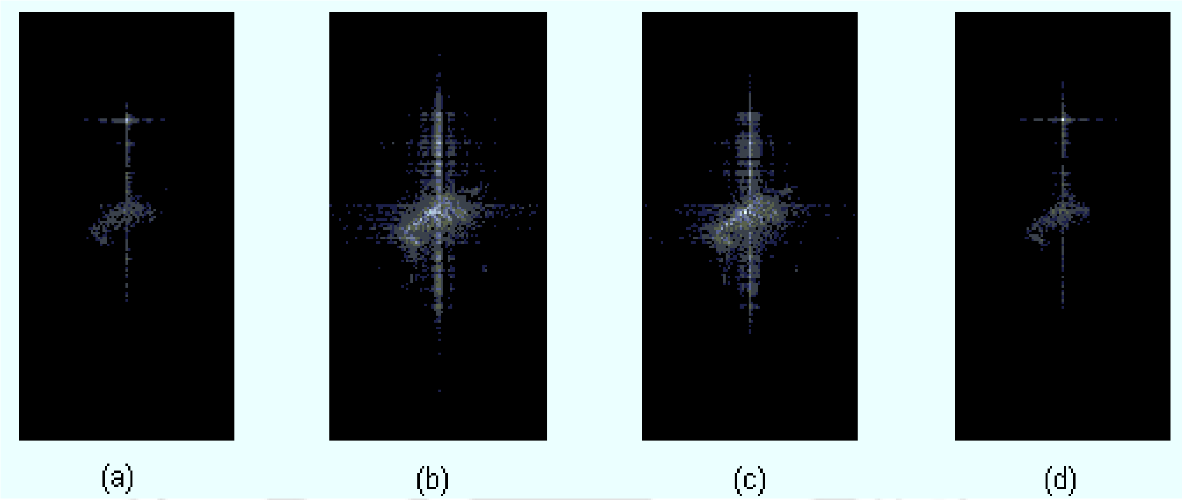

Figure 5.6: (a) HH image, (b) HV image, (c) VH image, and (d) VV image.

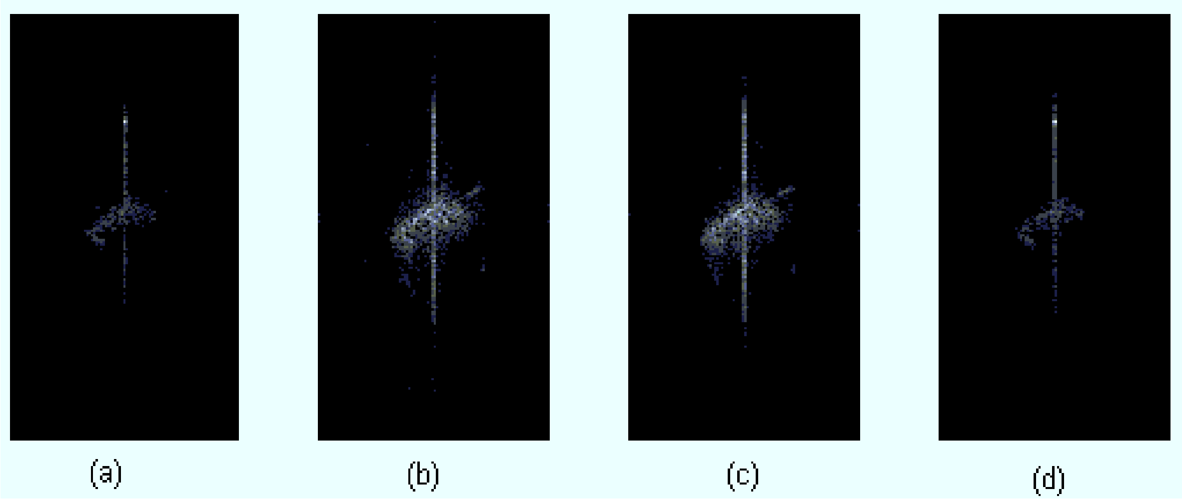

Figure 5.7: (a) $HH1$ image, (b) $HV1$ image, (c) $VH1$ image, and (d) $VV1$ image.

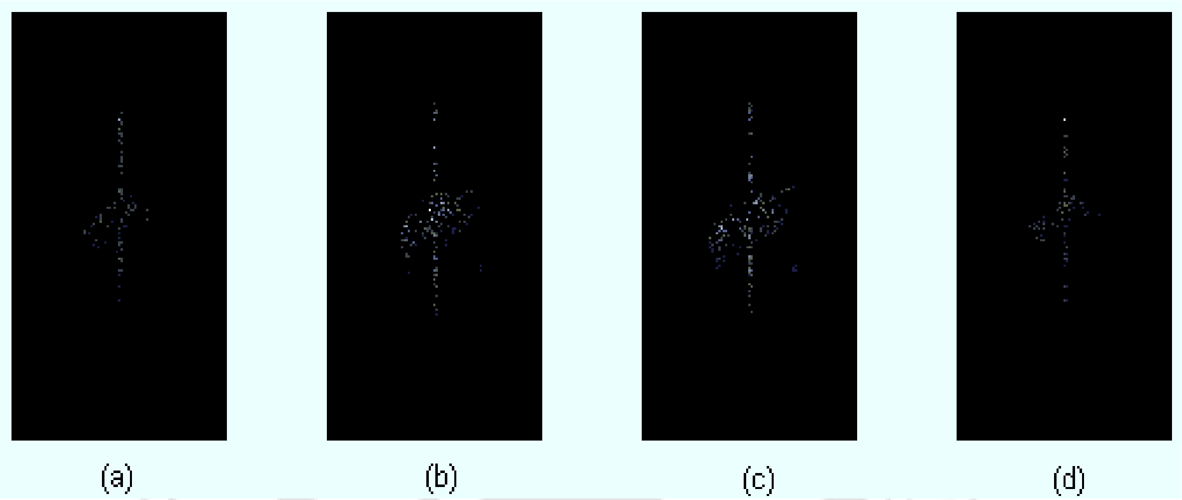

Figure 5.8: (a) $HH2$ image, (b) $HV2$ image, (c) $VH2$ image, and (d) $VV2$ image.

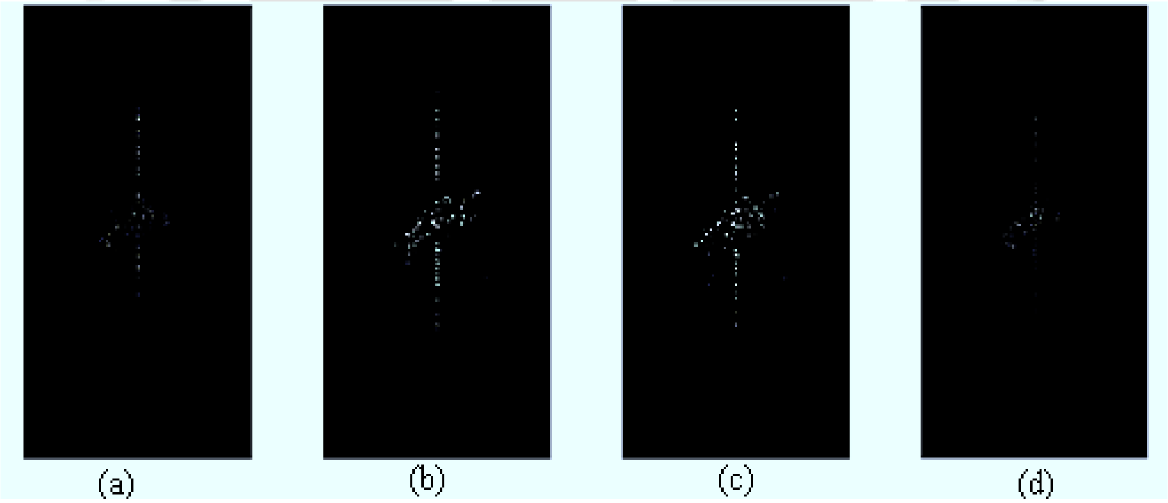

Figure 5.9: (a) $HH3$ image, (b) $HV3$ image, (c) $VH3$ image, and (d) $VV3$ image.

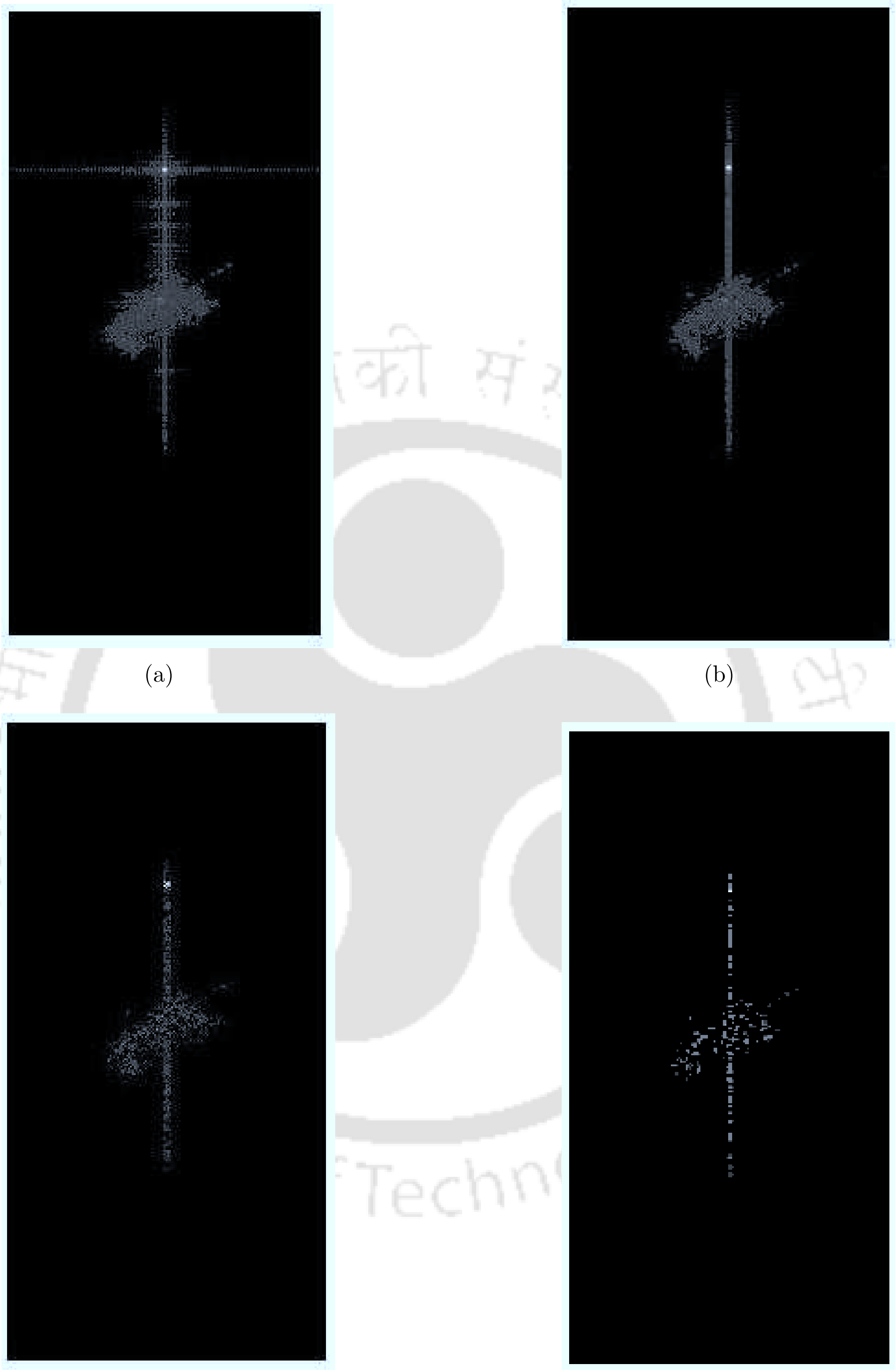

(a) (b)

(c) (d)

Figure 5.10: Combined image: (a) max(HH, HV, VH and VV), (b) max($HH1$, $HV1$, $VH1$ and $VV1$), (c) max($HH2$, $HV2$, $VH2$ and $VV2$) and (d) max($HH3$, $HV3$, $VH3$ and $VV3$).

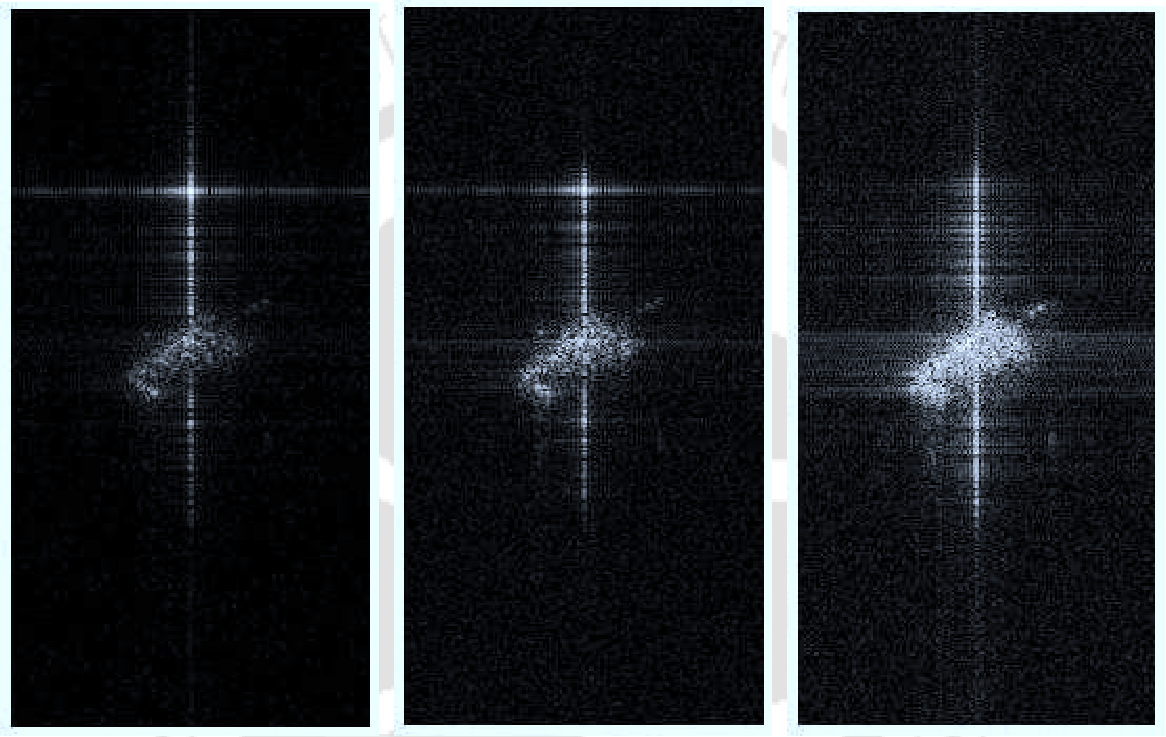

(a) (b) (c)

Figure 5.11: Target generators reconstructed after Pauli decomposition of PolSAR images. (a) Pauli1 (b) Pauli2, and (c) Pauli3.

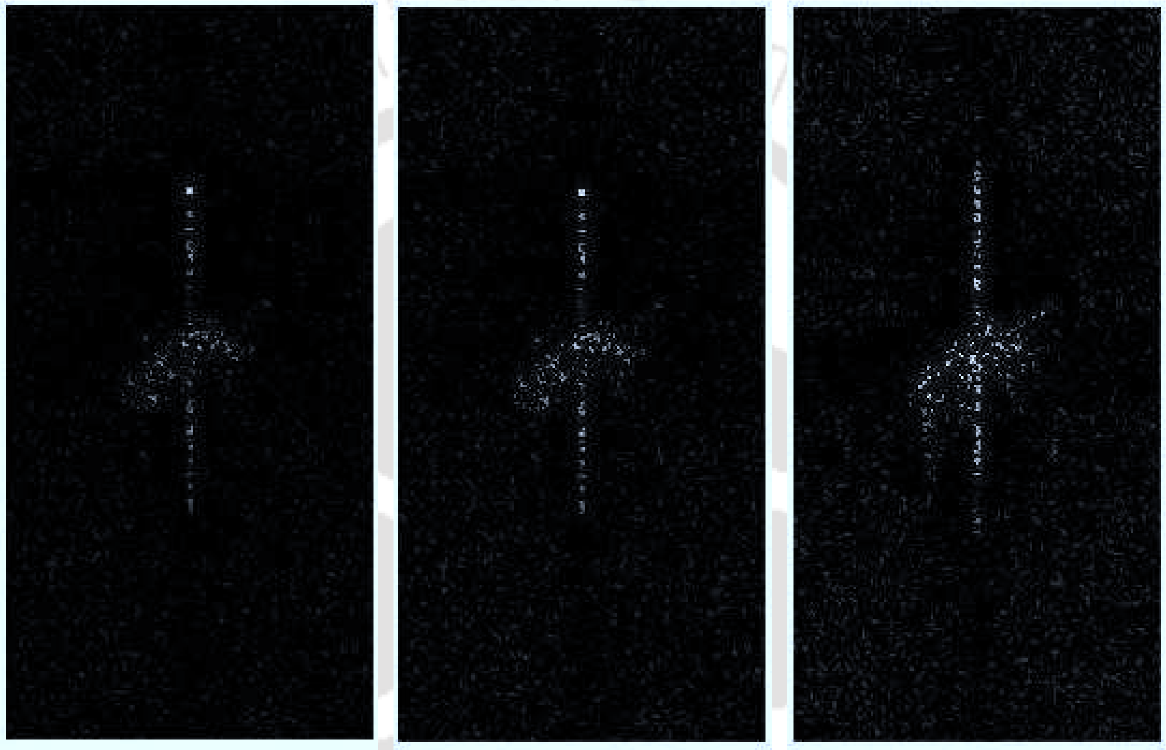

(a) (b) (c)

Figure 5.12: Target generators reconstructed after Pauli decomposition of apodized PolSAR images. (a) Pauli1 (b) Pauli2, and (c) Pauli3.

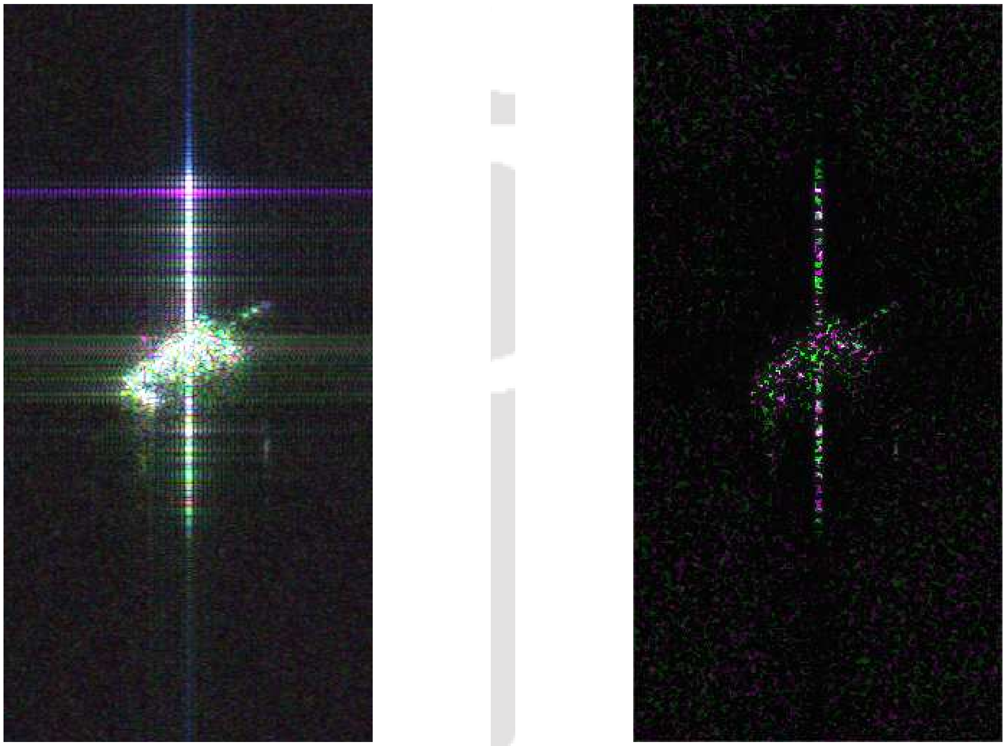

(a) (b)

Figure 5.13: Colour coded image of Pauli decomposition of (a) PolSAR images and (b) apodized PolSAR images: blue, Pauli1; red, Pauli2; green, Pauli3.

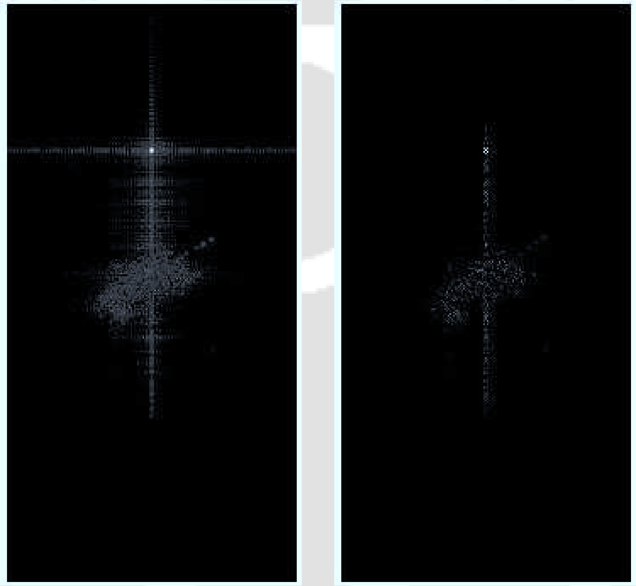
(a) (b)

Figure 5.14: (a) PCA decomposition of PolSAR images and (b) PCA decomposition of apodized PolSAR images.

6

Conclusion

Contents

The work presented in this thesis mainly involves extraction of information from polarimetric SAR (PolSAR) images. The entire thesis work has been divided into three major parts.

In the first part, the thesis deals with landcover mapping and crop classification using PolSAR images. More precisely, the thesis deals with unsupervised classification of different land features. In this, we have proposed and developed three new unsupervised algorithms for landcover classification. One of the most famous and efficient unsupervised classification techniques reported in literature is Wishart-entropy(H)/anisotropy(A)/alpha(α) scheme. However, when this entropy based classification scheme was applied to Flevoland data to evaluate its crop classification capability; it is observed that this scheme fails in correctly classifying all types of crops. This inspired us to develop new efficient algorithms for accurate landcover classification. A new unsupervised landcover classification scheme based on Gini-index was proposed. In this technique, a Gini-index has been introduced to replace polarimetric entropy parameter to overcome the drawbacks in later's evaluation. This new scheme is computationally more efficient and has higher discrimination capability in comparison to entropy based classification scheme. However, it too fails in correctly classifying all types of crops. So, a need was felt to develop an algorithm that could correctly discriminate all types of crops. The cause behind the better performance of Gini-index based classification scheme was realized and that led us to look for more entropy like parameters that can replace entropy in Wishart-$H/A/\alpha$ classification scheme. Entropy in the classic entropy based classification scheme is Shannon entropy. There exist different versions of Shannon entropy. A comparative study of different entropies based classification schemes was carried out on the basis of their discriminating abilities. The best performing classification scheme among all entropy based classification schemes, that correctly classifies all types of crops with better classification accuracy was reported. In parallel to this algorithm, a new fully automated landcover classification algorithm has also been developed to improve the efficiency of Wishart-$H/A/\alpha$. In this approach, the boundaries in entropy/alpha plane were decided based on the nature of a particular dataset. This facilitates the Wishart based classifier to converge correctly with fewer numbers of iterations; this saves a lot of computational time. All crops were observed to be correctly segmented with good classification accuracy by following this approach.

In the second part, the thesis deals with the recently introduced hybrid-Pol architecture. Presently, it is in the focus of radar community for its simple architecture and a number of advantages that it has over other dual-Pol modes. Even though hybrid-Pol is the optimum architecture among dual-Pol modes, it occupies half of the polarization information of full polarimetric SAR like any other dual-Pol mode. Hence, it was felt necessary to investigate the potential of this new hybrid-Pol architecture. To realize the potential of this new architecture, it was compared with the full polarimetric SAR system based on information content. The comparison has been carried out based on two different approaches. In these approaches, we have shown that information content in hybrid-Pol system is less but comparable with that of a quad-Pol system. It was also observed that the information content in hybrid-Pol is enough to extract a meaningful insight about the ground truth. Presently, the methods in literature suggested the common practice of converting dual-Pol data to pseudo quad-Pol data and then extracting the information by using the algorithms, which have been developed for quad-Pol data. This gave us the motivation to develop techniques to extract information from hybrid-Pol images directly. We have proposed three new approaches for the analysis of the hybrid-Pol data. The analysis of hybrid-Pol data was started with the Stokes vector for hybrid-Pol. From the Stokes vector, many secondary parameters were derived, which can be used for characterizing the hybrid-Pol data. One such parameter is the relative phase; using which an unsupervised landcover classification technique was proposed. We have shown that the basic scattering mechanisms can be discriminated by using this single parameter. This illustrates the rich potential of hybrid-Pol system. In the second approach, a hybrid-Pol version of the entropy/alpha decomposition method was developed for landcover classification. We have also obtained hybrid-Pol version of the fully automated landcover classification technique introduced by us. Both the techniques were found to be not effective in earth types discrimination, with the later technique performing slightly better. In the third approach, principal component analysis (PCA) of hybrid-Pol data was carried out, which was represented in terms of Stokes vector. Each element of Stokes vector was considered as a sample point in the PCA based algorithm. The principal components were then obtained on the application of PCA to hybrid-Pol data. An analogy between the principal components and the major scattering mechanisms has been established. Based on this analogy, an unsupervised landcover classification technique using hybrid-Pol data was proposed. Here, it was observed that all land features are correctly discriminated.

In the last part of the work, the thesis deals with polarimetric SAR image enhancement through sidelobe suppression techniques. There are different types of sidelobe suppression techniques reported in literature for SAR image enhancement. The thesis is concerned with sidelobe suppression in PolSAR images using non linear apodization (NLA) techniques. There are different types of NLA techniques, namely dual apodization (DA), complex dual apodization (CDA) and spatially variant apodization (SVA). We have developed a 2-D version of CDA algorithm by extending it. The algorithm has been named as extended 2-D CDA (E2CDA). We have also proposed a new NLA technique based on local gradient analysis and referred to it as LGNLA. In this technique, we have made use of the fact that mainlobe of the sinc wave is twice as wide as the sidelobe. It was shown that using this algorithm, the sidelobes were totally suppressed, and mainlobe width was reduced beyond the limits of super-resolution [64, 81]. The NLA algorithms originally developed for SAR imagery were extended to PolSAR images. 2-D version of SVA, E2CDA and LGNLA algorithms were used for removing the sidelobe noise from all the four polarization images of PolSAR and then the four images were combined into one image by taking maximum of each image at each spatial location. However, by this process some information about the target contained in the rest of the three images was lost. Hence, different decomposition techniques such as Pauli and PCA were used as a fusion technique to extract information from all the four polarization images and provide a suitable presentation for these images. A comparison of information provided by the PolSAR images, and its apodized version was carried out. It was shown that better information can be extracted through the target decomposition techniques if sidelobe noise is removed from the PolSAR images.

6.1 Thesis contributions

In this thesis, we have proposed new, efficient and effective algorithms for information extraction from polarimetric SAR images. The overall thesis contributions are summarized as follows.

- A new landcover classification technique based on Gini-index has been proposed. Using this new algorithm, enhanced crop classification accuracy has been reported. The Gini-index based classification scheme is computationally more efficient than entropy based classification scheme.

- We have explored different version of Shannon entropy such as Tsallis entropy and R*é*nyi entropy. New landcover classification schemes based on these entropies using PolSAR images have been developed. A comparative study of Tsallis and R*é*nyi entropy based classification schemes has been carried out on the basis of their discriminating abilities. The optimum one that correctly classifies different types of crops has been reported.

- A fully automatic and efficient algorithm to classify landcover from PolSAR images has been proposed. It is observed that the crop classification accuracy of Wishart-$H/A/\alpha$ scheme can be further enhanced by setting entropy and alpha boundaries as per the nature of dataset. By this approach, the Wishart based classifier converges with fewer numbers of iterations. This reduces the computational cost significantly; since each iteration of Wishart based classifiers requires a finite amount of time as the number pixels in a SAR image for remote sensing is of the order of 10^6.

- The potential of recently introduced hybrid-Pol configuration has been analysed by comparing it with the quad-Pol configuration based on the scattering information content.

- Three new approaches have been proposed for the analysis of hybrid-Pol data to extract information from hybrid-Pol SAR images.

- A new NLA technique has been proposed that completely removes the sidelobes and enhances the image resolution beyond the limits of super-resolution.

- The NLA techniques have been extended to PolSAR images. An extended CDA algorithm has been developed to be implemented on 2-D signal to suppress the sidelobes. It has been validated that better information can be extracted from apodized PolSAR images than non-apodized ones.

6.2 Scope for future work

- We have proposed three new unsupervised classification techniques for landcover mapping and crop classification. The performance of these techniques may be evaluated for other remote sensing applications, such as ice type discrimination and forest classification.

- The comparison of recently proposed hybrid-Pol data with full polarimetric SAR shows the rich potential of hybrid-Pol configuration. That motivates us to develop three algorithms to extract information from hybrid-Pol images. However, further analysis of hybrid-Pol data is still required to extract more information from its images.

- The potential of hybrid-Pol architecture was investigated for the few of remote sensing applications. Estimation of soil moisture from bare surfaces and estimation and correction of Faraday rotation is reported in [42]. We have proposed new approaches for landcover classification using hybrid-Pol data. The usefulness of hybrid-Pol architecture is yet to be exploited in various other remote sensing applications.

- The 2-D version of the newly proposed local gradient based NLA algorithm may be developed as a further work. In this thesis, we have developed the 1-D version of the algorithm and implementing it on an image by applying the 1-D algorithm sequentially to row-wise and column-wise and, then combining it suitably. Rather, a new 2-D version of this algorithm may be developed by extending the original concept of this algorithm to 2-D case.

- A new geometric approach based on the notion of the differential geometry of covariance matrices may be developed to extract information from polarimetric SAR data. The polarimetric covariance matrices are Hermitian positive definite matrices. It has been established in literature that positive definite matrices do not form an Euclidean space. Therefore, it becomes necessary to analyze the polarimetric SAR data by using non Euclidean geometry such as differential geometry. Also the Stokes vector which is located on a Poincare sphere is a manifold, so the analysis starting from Stokes vector should also be based on differential geometrical concept.
- There are different dual-Pol modes based on transmitting and receiving configuration. A new dual-Pol system that transmits elliptical polarization and receives the backscattered wave by dual orthogonal polarized channel may be conceptualized. Theoretical studies may be carried out to analyse this new architecture.

References

[1] J. B. Campbell, *Introduction to Remote Sensing*. The Guilford PRESS, 1994.

[2] K. Carver, C. Elachi, and F. Ulaby, “Microwave remote sensing from space,” *Proceedings of the IEEE*, vol. 73, no. 6, pp. 970–996, Jun. 1985.

[3] C. Elachi, T. Bicknell, R. Jordan, and W. Chialin, “Spaceborne synthetic aperture imaging radars: Applications, techniques, and technology,” *Proceedings of the IEEE*, vol. 70, no. 10, pp. 1174–1209, Oct. 1982.

[4] D. Evans, “Application of imaging radar data in earth science investigation,” *Electronics and Communication Engineering Journal*, vol. 11, no. 5, pp. 227–234, Oct. 1999.

[5] C. Elachi and J. J. van Zyl, *Introduction to the Physics and Techniques of Remote Sensing*. Wiley Interscience, 2006.

[6] C. A. Wiley, “Pulsed doppler radar methods and apparatus,” United States Patent 3 196 436, Jul., 1965.

[7] J. J. van Zyl, “Unsupervised classification of scattering behavior using radar polarimetry data,” *IEEE Transactions on Geoscience and Remote Sensing*, vol. 27, no. 1, pp. 36–45, Jan. 1989.

[8] D. Giuli, “Polarization diversity in radars,” *Proceedings of the IEEE*, vol. 74, no. 2, pp. 245–269, Feb. 1986.

[9] M. E. Nord, T. L. Ainsworth, J.-S. Lee, and N. J. S. Stacy, “Comparison of compact polarimetric synthetic aperture radar modes,” *IEEE Transaction on Geoscience and Remote Sensing*, vol. 47, no. 1, pp. 174–188, Jan. 2009.

[10] T. Ainsworth, J. Kelly, and J.-S. Lee, “Classification comparisons between dual-pol, compact polarimetric and quad-pol SAR imagery,” *ISPRS Journal of Photogrammetry and Remote Sensing*, vol. 64, no. 5, pp. 464–471, 2009.

[11] P. Beckmann, “Optimum polarization for polarization discrimination,” *Proceedings of the IEEE*, vol. 56, no. 10, pp. 1755–1756, Oct. 1968.

[12] R. K. Raney, “Hybrid-polarity SAR architecture,” *IEEE Transaction on Geoscience and Remote Sensing*, vol. 45, no. 11, pp. 3397–3404, Nov. 2007.

[13] T. Misra, S. S. Rana, R. N. Tyagi, and K. Thyagarajan, “RISAT: first planned SAR mission of ISRO,” *Society of Photo-Optical Instrumentation Engineers (SPIE) Conference Series*, vol. 6407, Nov. 2006.

[14] F. Ulaby, D. Held, M. Donson, K. McDonald, and T. Senior, "Relating polaization phase difference of SAR signals to scene properties," *IEEE Transactions on Geoscience and Remote Sensing*, vol. GE-25, no. 1, pp. 83–92, Jan. 1987.

[15] H. Mott, *Antennas for radar and communication: A polarimetric Approach.* John Wiley and Sons, 1992.

[16] J.-S. Lee and E. Pottier, *Polarimetric Radar Imaging: From Basics to Applications.* CRC Press, 2009.

[17] R. Touzi, S. Goze, T. L. Toan, A. Lopes, and E. Mougin, "Polarimetric discriminators for SAR images," *IEEE Transactions on Geoscience and Remote Sensing*, vol. 30, no. 5, pp. 973–980, Sep. 1992.

[18] A. Guissard, "Mueller and Kennaugh matrices in radar polarimetry," *IEEE Transactions on Geoscience and Remote Sensing*, vol. 32, no. 3, pp. 590–597, May 1994.

[19] S. R. Cloude and E. Pottier, "A review of target decomposition theorems in radar polarimetry," *IEEE Transactions on Geoscience and Remote Sensing*, vol. 34, no. 2, pp. 498–518, Mar. 1996.

[20] J. R. Huynen, "Phenomenological theory of radar targets," Ph.D. dissertation, Technical University, Delft, The Netherlands, 1970.

[21] D. Evans, T. Farr, J. V. Zyl, and H. Zebker, "Radar polarimetry: analysis tools and applications," *IEEE Transactions on Geoscience and Remote Sensing*, vol. 26, no. 6, pp. 774–789, Nov. 1992.

[22] J. J. van Zyl, H. Zebker, and C. Elachi, "Imaging radar polarization signature: theory and observation," *Radio Science*, vol. 22, pp. 529–543, 1987.

[23] S. Chandrasekhar, *Radiative Transfer.* New York: Dover, 1960.

[24] R. Touzi, W. M. Boerner, J. S. Lee, and E. Lueneburg, "A review of polarimetry in the context of synthetic aperture radar," *Canadian Journal of remote Sensing*, vol. 30, no. 3, pp. 380–407, 2004.

[25] W. Holm and R. Barnes, "On radar polarization mixed state decomposition theorems," *in Proceedings 1988 USA National Radar Conference*, Apr. 1988.

[26] S. R. Cloude, "Group theory and polarization algebra," *OPTIK*, vol. 75, no. 1, pp. 26–36, 1986.

[27] ——, "Target decomposition theorems in radar scattering," *ELECTRONICS LETTERS*, vol. 21, no. 1, pp. 22–24, Jan. 1985.

[28] J. J. van Zyl, "Application of Cloudes target decomposition theorem to polarimetric imaging radar data," *Radar Polarimetry*, vol. SPIE- 1748, pp. 184–212, Jul. 1992.

[29] A. Freeman and S. L. Durden, "A three-component scattering model for polarimetric SAR data," *IEEE Transactions on Geoscience and Remote Sensing*, vol. 36, no. 3, pp. 963–973, May 1998.

[30] Y. Yamaguchi, T. Moriyama, M. Ishido, and H. Yamada, “Four-component scattering model for polarimetric SAR image decomposition,” *IEEE Transactions on Geoscience and Remote Sensing*, vol. 43, no. 8, pp. 1699–1706, Aug. 2005.

[31] A. Freeman, “Fitting a two-component scattering model to polarimetric SAR data from forests,” *IEEE Transactions on Geoscience and Remote Sensing*, vol. 45, no. 8, pp. 2583–2592, Aug. 2007.

[32] V. Alberga, D. Borghys, G. Satalino, D. K. Staykova, A. Borghgraef, F. Lapierre, and C. Perneel, “Comparison of algorithms for the classification of polarimetric SAR data,” *Proceedings of SPIE - Image and Signal Processing for Remote Sensing XV*, vol. 7477, no. 74771V, Sep. 2009.

[33] E. Pottier and J.-S. Lee, “Unsupervised classification scheme of PolSAR images based on the complex Wishart distribution and the ‘H/A/Alpha’ polarimetric decomposition theorem,” in *EUSAR 2000; 3rd European Conference on Synthetic Aperture Radar*, Munich, Germany, May 2000, pp. 265–268.

[34] J.-S. Lee, M. R. Grunes, T. L. Ainsworth, L.-J. Du, D. L. Schuler, and S. R. Cloude, “Unsupervised classification using polarimetric decomposition and the complex Wishart classifier,” *IEEE Transactions on Geoscience and Remote Sensing*, vol. 37, no. 5, pp. 2249–2258, Sep. 1999.

[35] C. Xiuwana, H. Hepingb, R. Tateishic, and C.-H. Ahn, “A method on land cover classification by combining unsupervised algorithm and training data,” *International Journal of Remote Sensing*, vol. 14, no. 4, pp. 15–20, 1999.

[36] S. R. Cloude and E. Pottier, “An entropy based classification scheme for land applications of polarimetric SAR,” *IEEE Transactions on Geoscience and Remote Sensing*, vol. 35, no. 1, pp. 68–78, Jan. 1997.

[37] J.-S. Lee, M. R. Grunes, E. Pottier, and L. Ferro-Famil, “Unsupervised terrain classification preserving polarimetric scattering characteristics,” *IEEE Transactions on Geoscience and Remote Sensing*, vol. 42, no. 4, pp. 722–731, Apr. 2004.

[38] J.-C. Souyris, P. Imbo, R. Fjortoft, S. Mingot, and J.-S. Lee, “Compact polarimetry based on symmetry properties of geophysical media: The $pi/4$ mode,” *IEEE Transaction on Geoscience and Remote Sensing*, vol. 43, no. 3, pp. 634–646, Mar. 2005.

[39] R. K. Raney, “Dual-polarized SAR and Stokes parameters,” *IEEE Geoscience and Remote Sensing Letters*, vol. 3, no. 3, pp. 317–319, Jul. 2006.

[40] F. Charbonneau, B. Brisco, and H. McNairn, “Compact polarimetry: Multi-thematic evaluation,” in *in POLInSAR 2009, Frascati, Italy*, 2009.

[41] L. Chen, F. Cao, and W. Hong, “Unsupervised classification for compact polarimetric SAR data using $m-\delta$ decomposition, SPAN and the Wishart classifier,” in *APSAR 2009*, Oct. 2009, pp. 36–45.

[42] M.-L. Truong-Lo, A. Freeman, P. C. Dubois-Fernandez, and E. Pottier, “Estimation of soil moisture and faraday rotation from bare surfaces using compact polarimetry,” *IEEE Transactions on Geoscience and Remote Sensing*, vol. 47, no. 11, pp. 3608–3615, Nov. 2009.

[43] J. Su and H. Ma, “A new speckle reduction algorithm for SAR images,” *Synthetic Aperture Radar, 2007. APSAR 2007. 1st Asian and Pacific Conference on*, pp. 331–337, Nov. 2007.

[44] J. Schroeder and T. Bose, “Speckle reduction in SAR imagery by Lp normed filtering,” *Signals, Systems and Computers, 2001. Conference Record of the Thirty-Fifth Asilomar Conference on*, vol. 1, pp. 365–370, Aug. 2001.

[45] C. Shen, Y. Peng, L. Pi, and Z. Li, “Variational-based speckle noise removal of SAR imagery,” *Geoscience and Remote Sensing Symposium*, vol. 1, pp. 532–535, Jul. 2007.

[46] J.-M. Park, W.J.Song, and W.A.Pearlman, “Speckle filtering of SAR images based on adaptive windowing,” *Vision, Image and Signal Processing, IEE Proceedings*, vol. 146, no. 4, pp. 191–197, Aug. 1999.

[47] J. W. Goodman, “Some fundamental properties of speckle,” *Journal of optics Society Amer*, vol. 66, no. 11, pp. 1145–1149, Nov. 1976.

[48] C. Lopez-Martinez and X. Fabregas, “Polarimetric SAR speckle noise model,” *IEEE Transactions on Geoscience and Remote Sensing*, vol. 41, no. 10, pp. 2232–2242, Oct. 2003.

[49] L. M. Novak and M. C. Burl, “Optimal speckle reduction in polarimetric SAR imagery,” *IEEE Transactions on Aerospace and Electronic Systems*, vol. 26, no. 2, pp. 293–305, Mar. 1990.

[50] J.-S. Lee, M. Grunes, and S. Mango, “Speckle reduction in multipolarization, multifrequency SAR imagery,” *IEEE Transactions on Geoscience and Remote Sensing*, vol. 29, no. 4, pp. 535–544, Jul. 1991.

[51] J.-S. Lee, M. Grunes, and G. de Grandi, “Polarimetric SAR speckle filtering and its implication for classification,” *IEEE Transaction on Geoscience and Remote Sensing*, vol. 37, no. 5, pp. 2363–2373, Sep. 1999.

[52] V. J. Schwarz, “Mathematical-statistical description of the iterative beam removing technique (method CLEAN),” *Astron. Astrophys.*, vol. 65, pp. 345–356, 1978.

[53] A. Segalovitz and B. D. Frieden, “A CLEAN-type deconvolution algorithm,” *Astron. Astrophys.*, vol. 70, pp. 335–343, 1978.

[54] J. Tsao and B. Steinberg, “Reduction of sidelobe and speckle artifacts in microwave imaging: the CLEAN technique,” *IEEE Transactions on Antennas and Propagation*, vol. 36, no. 4, pp. 543–556, Apr. 1988.

[55] Y. Sun and P. Lin, “An improved method of ISAR image processing,” in *in Proceedings of the 35th Midwest Symposium on Circuits and System*, vol. 2, no. 4, Washington, DC, USA, Aug. 1992, pp. 983–986.

[56] M. Martorella, A. Cacciamano, E. Giusti, F. Berizzi, B. Haywood, and B. Bates, “CLEAN technique for polarimetric ISAR,” *International Journal of Navigation and Observation*, 2008.

[57] S. DeGraaf, “Sidelobe reduction via adaptive FIR filtering in SAR imagery,” *IEEE Transactions on Image Processing*, vol. 3, no. 3, pp. 292–301, May 1994.

[58] H. C. Stankwitz, R. J. Dallaire, and J. R. Fineup, “Nonlinear apodization for sidelobe control in SAR imagery,” *IEEE Transaction on Aerospace and Electronics Systems*, vol. 31, no. 4567, pp. 267–279, Jan 1995.

[59] G. Thomas and N. Gadhok, "Sidelobe apodization in Fourier imaging," *Conference Record of the Thirty-Fifth Asilomar Conference on Signals, Systems and Computers, 2001*, vol. 2, pp. 1369–1373, 2001.

[60] B. Sarkar, R. K. Panigrahi, and A. K. Mishra, "Sidelobe suppression in Wigner distribution using non-linear apodization," *IEEE Indicon*, pp. 81–84, Dec. 2009.

[61] F. Harris, "On the use of windows for harmonic analysis with the discrete Fourier transform," *IEEE Proceedings*, vol. 66, no. 1, pp. 51–83, Jan. 1978.

[62] B. H. Smith, "Generalization of spatially variant apodization to noninteger Nyquist sampling rates," *IEEE Transaction on Aerospace and Electronics Systems*, vol. 9, no. 6, pp. 1088–1093, Jun. 2000.

[63] X. Xu and R. M. Narayanan, "Enhanced resolution in SAR/ISAR imaging using iterative sidelobe apodization," *IEEE Transaction on Aerospace and Electronics Systems*, vol. 14, no. 4, pp. 537–546, Apr. 2005.

[64] H. C. Stankwitz and M. R. Kosek, "Super-resolution for SAR/ISAR RCS measurement using spatially variant apodization (super-SVA)," in *in Proc.AMTA Symp.*, Nov. 1995, pp. 251–256.

[65] C. Castillo-Rubio, S. Llorente-Romano, and C. Burgos-Garcia, "Spatially variant apodization for squinted synthetic aperture radar images," *IEEE Transactions on Image Processing*, vol. 16, no. 8, pp. 2023–2027, Aug. 2007.

[66] D. Andre, "Sidelobe rotation and apodization," in *2006 IEEE Conference on Radar*, Apr. 2006, p. 5 pp.

[67] G. Thomas, B. Flores, and J. Sok-Son, "SAR sidelobe apodization using the Kaiser window," in *International Conference on Image Processing,*, vol. 1, 2000, pp. 709 –712.

[68] P. Patel, H. S. Srivastava, and R. R. Navalgund, "Use of synthetic aperture radar polarimetry to characterize wetland targets of Keoladeo national park, Bharatpur, India," *CURRENT SCIENCE*, vol. 97, no. 4, pp. 529–537, Aug. 2009.

[69] Q. Burrell, "The Bradford distribution and the Gini index," *SCIENTOMETRICS*, vol. 21, no. 2, pp. 181–194, Apr. 1991.

[70] R. O. Duda, P. E. Hart, and D. G. Stork, *Pattern Classification.* John Wiley and Sons, 2001.

[71] Y. Wu, K. Ji, W. Yu, , and Y. Su, "Region-based classification of polarimetric SAR images using Wishart MRF," *IEEE Geoscience and Remote Sensing Letters*, vol. 5, no. 4, pp. 668–672, Oct. 2008.

[72] A. Rényi, "On measures of information and entropy," *Proceedings of the 4th Berkeley Symposium on Mathematics, Statistics and Probability 1960.*, pp. 547–561, 1961.

[73] P. Bromiley, N. Thacker, and E. Bouhova-Thacker, "Shannon entropy, Renyi entropy, and information," *Tina Memo No. 2004-004, Statistics and segmentation series*, 2001.

[74] C. G. Chakrabarti and K. De, "Boltzmann-Gibbs entropy: axiomatic characterization and application," *International Journal of Mathematics and Mathematical Sciences*, vol. 23, no. 4, pp. 243–251, 2000.

[75] C. Tsallis, “Possible generalization of Boltzmann-Gibbs statistics,” *Journal of Statistical Physics*, vol. 52, pp. 479–487, 1988.

[76] M. P. de Albuquerque, I. A. Esquef, A. R. G. Mello, and M. P. de Albuquerque, “Image thresholding using Tsallis entropy,” *Pattern Recognition Letters*, vol. 25, no. 9, pp. 1059–1065, 2004.

[77] S. R. Cloude, “The dual polarisation entropy/alpha decomposition: A PALSAR case study,” in *PolinSAR Workshop 2007, Frascatti, Italy*, 2007.

[78] I. T. Jollief, *Principal Component Analysis.* Springer, New York, 2002.

[79] A. K. Mishra, “Validation of PCA and LDA for SAR ATR,” *TENCON 2008 - 2008 IEEE Region 10 Conference*, pp. 1–6, Nov. 2008.

[80] A. K. Mishra and B. Mulgrew, “Multipolar SAR ATR: Experiments with the GTRI dataset,” May 2008, pp. 1–5.

[81] F. M. Dickey, L. A. Romero, and A. W. Doerry, “Superresolution and synthetic aperture radar,” *S. N. Laboratories, Ed. Albuquerque, New Mexico: Sandia National Laboratories*, 2001.

List of Publications

Refereed Journals

1. R. K. Panigrahi and A. K. Mishra, "Gini-Index Based Land-cover Classification Using Polarimetric Synthetic Aperture Radar", *International Journal of Remote Sensing* (Accepted).

Manuscripts Under review

1. R. K. Panigrahi and A. K. Mishra, "Comparison of Hybrid-Pol with Quad-Pol Scheme Based on Polarimetric Information Content", *Progress in Electromagnetics Research Symposium.*

Manuscripts Under Preparation:

1. R. K. Panigrahi and A. K. Mishra, "Analysis of different entropy based landcover classification", to be submitted to *IEEE Transaction on Geoscience and Remote Sensing.*
2. R. K. Panigrahi and A. K. Mishra, "Fully automated landcover classification using Wishart-H/A/α", to be submitted to *Remote Sensing of Environment.*
3. R. K. Panigrahi and A. K. Mishra, "PCA analysis of hybrid-pol data", to be submitted to *Remote Sensing letters.*

Conference Publications

1. R. K. Panigrahi and A. K. Mishra, "Comparison of hybrid-polarization with Quad-polarization schemes based on airborne SAR images", *A Workshop on Advanced Antenna Technology, 2010 IEEE Indian Antenna Week* , Puri, India, pp. 1–4, May 31 2010-June 4 2010.
2. R. K. Panigrahi and A. K. Mishra, "Multipolar SAR image enhancement using non-linear apodization,", *IRS Germany*, 2009.

3. R. K. Panigrahi and A. K. Mishra, “A Novel Algorithm for Apodization and Super-Resolution in Fourier Imaging”, *Devices and Communications (ICDeCom), 2011 International Conference on*, vol., no., pp.1-5, 24-25 Feb. 2011.

4. R. K. Panigrahi and A. K. Mishra, “Spaceborne synthetic aperture radar image enhancement using non linear apodization,”, *IRSI Bangalore*, 2009.

A

Original Publication

Contents

A.1 Gini-index based landcover classification using polarimetric synthetic aperture radar

This appendix is a reproduction of the journal paper which has been accepted for publication in International Journal of Remote Sensing (Taylor and Francis group). The title of the journal is “Gini-Index Based Land-cover Classification Using Polarimetric Synthetic Aperture Radar”. The colour images in this appendix are given in gray scale. The corresponding colour images are provided in Chapter 3.